

---

# Electronic Correlation Calculations of small Molecules with Quantum Monte Carlo Methods

Diploma Thesis

by Alexander Badinski

Fritz-Haber-Institut  
der Max-Planck-Gesellschaft

Supervisor

Prof. Dr. Udo Scherz

Prof. Dr. Matthias Scheffler

Technischen Universität Berlin

Berlin, February 2004

---

## Acknowledgment

I would like to express my gratitude to several people who have contributed for this work to become realized. Thank you Prof. Matthias Scheffler for suggesting to me the topic for this thesis, for providing me such an inspiring environment and also in supporting my participation at the workshop in Lyon (Sep. 2002) as an excellent introduction. Thank you Peter Kratzer and Martin Fuchs for our many hours of fruitful discussions. I would like to thank Claudia Filippi and Cyrus Umrigar for providing me all required QMC codes and for discussing specific questions.

I would like to thank all members of the FHI (and most of all my neighbor Jörg Behlers) for our conversations. For her endurance, I gratefully thank Shirley Caduhada in giving answers to my endless questions concerning English Grammar. And last but not least, I would like to thank my family for their indispensable support, especially toward the end of that work.

# Contents

<b>1</b>	<b>Introduction and Motivation</b>	<b>7</b>
<b>2</b>	<b>Many-Particle Problem</b>	<b>13</b>
2.1	The Schrödinger Equation . . . . .	13
2.2	Born-Oppenheimer Approximation . . . . .	14
2.3	Hartree-Fock . . . . .	15
2.4	Configuration Interaction . . . . .	17
2.5	Electron Correlation . . . . .	17
<b>3</b>	<b>Theory of QMC</b>	<b>21</b>
3.1	Monte Carlo Integration . . . . .	21
3.1.1	Statistical Foundations . . . . .	21
3.1.2	Importance Sampling . . . . .	22
3.1.3	Metropolis Algorithm . . . . .	23
3.2	Variational Monte Carlo . . . . .	25
3.2.1	Total Energy . . . . .	26
3.2.2	The Trial Wavefunction $\Psi_T$ . . . . .	26
3.2.3	The Electron-Electron Cusp Condition . . . . .	29
3.2.4	Wave Function Optimization . . . . .	29
3.2.5	The VMC Algorithm with Importance Sampling . . . . .	31
3.3	Diffusion Monte Carlo . . . . .	34
3.3.1	Ground State Projection . . . . .	34
3.3.2	Short Time Approximation . . . . .	35
3.3.3	Importance Sampling in DMC . . . . .	38
3.3.4	Total Energy in DMC . . . . .	39
3.3.5	The Fixed Node Approximation in DMC . . . . .	40
3.3.6	DMC Algorithm with Importance Sampling . . . . .	41

3.4	Pseudopotentials in QMC . . . . .	44
3.4.1	The Construction of Pseudopotentials . . . . .	45
3.4.2	Pseudopotentials in VMC . . . . .	47
3.4.3	Pseudopotentials in DMC - The Pseudopotential Localization Approximation . . . . .	49
3.4.4	Interdependence of the Fixed-Node and Pseudopotential Localization Approximation . . . . .	51
3.5	Correlated Sampling . . . . .	51
3.5.1	Correlated Sampling in VMC . . . . .	51
3.5.2	Correlated Sampling in DMC . . . . .	53
3.5.3	Re-Centered versus Orbitals Re-Optimized Correlated Sampling . . . . .	54
<b>4</b>	<b>Results</b>	<b>55</b>
4.1	Binding Energies . . . . .	55
4.1.1	Terminology - Binding Energy . . . . .	56
4.1.2	Technicalities . . . . .	56
4.1.3	Results and Discussion . . . . .	58
4.1.4	Comparison with other Quantum Chemical Methods and DMC References . . . . .	61
4.2	Equilibrium Geometries . . . . .	66
4.2.1	Terminology . . . . .	66
4.2.2	Technicalities . . . . .	68
4.2.3	Results and Discussion . . . . .	69
4.2.4	Comparison with other Reference Methods . . . . .	70
4.3	Vibrational Frequencies . . . . .	72
4.3.1	Terminology . . . . .	72
4.3.2	Technicalities - Treatment of Di- and Tri-Atomic Molecules . . . . .	73
4.3.3	Discussion . . . . .	73
4.3.4	Comparison with other Reference Methods . . . . .	75
4.4	Hydrogen Bonding and QMC . . . . .	76
4.4.1	Hydrogen Bonding . . . . .	76
4.4.2	Energy Barriers in the Proton Transfer . . . . .	78
4.4.3	Technicalities . . . . .	79
4.4.4	Results and Discussion . . . . .	80
4.4.5	Comparison with other Quantum Chemical Methods . . . . .	82

<b>5</b>	<b>Methodological Investigations</b>	<b>85</b>
5.1	Jastrow Factor . . . . .	85
5.2	The Basis Set . . . . .	88
5.2.1	Selection and Construction of the HF Basis Set . . . . .	89
5.2.2	Results & Discussion . . . . .	90
5.3	Pseudopotential . . . . .	92
5.3.1	Results & Discussion . . . . .	93
5.3.2	Comparison with other QMC Calculations . . . . .	95
5.4	MCSCF . . . . .	98
5.4.1	MCSCF Trial Wavefunctions . . . . .	98
5.4.2	Results & Discussion . . . . .	99
5.4.3	Comparison with other QMC MCSCF References . . . . .	103
5.5	Time Steps . . . . .	105
5.5.1	Results & Discussion for Different Time Steps . . . . .	106
5.6	Time Evolution in DMC . . . . .	108
5.7	Different Quadrature Rules . . . . .	110
5.8	Correlated Sampling . . . . .	111
5.8.1	The Potential Energy Curve and the Diffusion Time . . . . .	111
5.8.2	Orbital Re-Optimized versus Re-Centered Correlated Sampling . . . . .	113
<b>6</b>	<b>Summary and Outlook</b>	<b>117</b>
<b>A</b>		<b>121</b>
A.1	Harmonic Approximation of the BOS . . . . .	121
A.2	Internal and Mass-weighted Coordinates for H <sub>2</sub> O . . . . .	122
A.3	Definitions in Statistics . . . . .	122
A.4	Construction of our HF Basis sets . . . . .	124
A.5	Technical Instructions for a MCSCF Calculation with QMC . . . . .	125
A.6	Unit Conversion . . . . .	126
<b>B</b>	<b>Tables</b>	<b>127</b>



# Chapter 1

## Introduction and Motivation

This thesis investigates the capability of the Variational Monte Carlo (VMC) and Diffusion Monte Carlo (DMC) methods in calculating electronic structures for a set of small molecules. Thereby, we examine some of their physical properties with a particular focus on many-particle correlation effects in quantum mechanics.

### The Many-Particle Problem (Chapter 2)

For many-particle problems, it is generally impossible to find exact solutions due to their high dimensionality. For illustration, let us consider a malonaldehyde molecule ( $\text{C}_3\text{O}_2\text{H}_4$ ) with 28 valence electrons. An exact solution would require the knowledge of the electron probability distribution given by the wavefunction,  $\Psi$ , which depends on  $3 \times 28$  spatial electron coordinates. Supposing that 10 grid points in each dimension are enough for an adequate numerical representation of  $\Psi$ , one still needs  $10^{3 \times 28}$  spatial grid points to fully describe  $\Psi$ . Yet, this number is one million times larger than the amount of all atoms in our universe<sup>1</sup>. Such complexity reflects the difficulty in numerical handling and thus in finding exact solutions to the many-particle problem.

The complexity illustrated in that example is a result of many-particle effects in quantum mechanics (i.e. Fermi and Coulomb correlation). However, these effects are important for a quantitative prediction of all material properties. Such importance calls for accurate and efficient methods when calculating electronic structures by solving the many-electron Schrödinger equation. To do so, different methods have been developed such as Hartree-Fock (HF), Configuration Interaction (CI), Coupled Cluster (CC) or Density Functional Theory (DFT). Each method has its own advantages and disadvantages. HF, by definition, includes the exchange energy exactly but completely omits correlations beyond the Pauli principle. CI and CC methods [POPPE 1987] can be very accurate and allow for systematic improvement. Nevertheless, they are nu-

---

<sup>1</sup>This estimate assumes that all matter is hydrogen, which is true for more than 99%, and a mass of the universe of  $5.98 \cdot 10^{50} \text{kg}$  [HOLLEMAN 1995].

merically very costly and are currently not suitable for systems with more than 20 first row atoms [TSUZUKI 2001]. DFT is in principle an exact method to describe many-electron systems and is much less numerically demanding as compared to the CC and CI post-HF methods. Yet, in practice it requires approximations for the exchange-correlation functional such as BLYP [LEE 1988]. Also, it is very difficult within DFT to judge its accuracy or to systematically improve when necessary. Although DFT with approximative density functionals has proven to be very successful in describing electronic structure properties, like elastic properties, vibrational frequencies and molecular geometries [PERDEW 2003], it often overestimates binding energies<sup>2</sup>. Hence, these accuracy and efficiency problems within the listed methods indicate a further need for an accurate yet efficient many-body approach as found in Quantum Monte Carlo.

### Variational and Diffusion Monte Carlo (Chapter 3)

Quantum Monte Carlo (QMC) methods allow for solutions to the many-electron Schrödinger equation with a statistical approach. The simplest form of these methods, Variational Monte Carlo (VMC), is based on evaluating a high-dimensional integral,  $\langle \Psi | \hat{H} | \Psi \rangle$ , with the Monte Carlo Integration (MCI) technique. For problems involving more than a few dimensions, the convergence of the integral using MCI is much faster than for conventional integration techniques. This stems from the important fact that the statistical error in the estimated integral,  $\langle \Psi | \hat{H} | \Psi \rangle$ , decreases as square root of the number of points sampled, irrespective of the dimensionality of the problem.

The second and more advanced QMC method used in this thesis is Diffusion Monte Carlo (DMC). It solves the time-dependent many-electron Schrödinger equation by mapping it to the classical diffusion and rate equations and by transforming the time into imaginary units. The evolution of an initial arbitrary wavefunction,  $\Psi$ , is then simulated through a diffusion and rate process. The DMC method finally projects out the unknown  $N$ -electron ground state,  $\Psi_0$ , and thereby yields in principle the true ground state energy.

QMC methods, in particular DMC, have already proven to be very useful in a number of applications. A landmark achievement for DMC applications was the calculation of the exchange-correlation energy of the uniform electron gas [CEPERLEY 1980]. This exchange-correlation energy then allowed to find an accurate expression of the correlation functional,  $\varepsilon_{xc}^{\text{hom}}(n)$ , in the local-density approximation (LDA), used in DFT [PERDEW 1981]. “Without these early DMC results, DFT might have never grown into the leviathan we know today.” [FOULKES 2001]

---

<sup>2</sup>When looking at a standard (G2) test set of 148 molecules, the mean absolute deviation of the binding energy for B3LYP is 0.14 eV, for BLYP 0.32 eV or for PBE 0.73 eV. For comparison, HF yields 6.43 eV and CC in the complete basis set limit yields 0.06 eV [PERDEW 2003, FELLER 1998].



A further successful DMC application was demonstrated for carbon  $C_{20}$  clusters. As found by Raghavachari<sup>3</sup> et al. in 1993, DFT LDA predicted the  $C_{20}$  cage structure to be about 4 eV lower in energy than the ring, while the BLYP functional essentially predicted the opposite. However, Grossman<sup>4</sup> et al. disproved in 1995 both predictions with DMC calculations and showed that the graphitic bowl was the lowest energy isomer. This was confirmed by Murphy<sup>5</sup> et al. in 1998 using a high-level perturbation theory approach. Another critical study of DFT LDA and GGA results investigated the dissociative adsorption of  $H_2$  on the Si(001) surface and found a significant underestimation of the reaction energies and barriers when compared to DMC results [FILIPPI 2002 ].

Despite these rather young successful applications in electronic structure calculations, there are several reasons why QMC methods are still not widely used. The first and paramount reason is the large numerical effort that is necessary for statistical significant predictions. Secondly, efficient QMC methods still show open methodological questions, which need to be better understood such as the use of pseudopotentials or dealing with anti-symmetric wavefunctions. A last major drawback for a wider application of QMC methods appears to be the scarcity of experience. Only a very limited amount of critical studies have been published to demonstrate the accuracy and reliability of QMC results [FOULKES 2001]. Other methods, like DFT with an exponentially increasing number of several thousand annual publications [KOCH 2001], have gotten much more attention in the last years. It will be rather speculative if QMC methods ever become as widely used as other methods today. However, QMC methods are likely to become a supplement for the others, since they have already taken a place in setting benchmarks in electronic structure calculations and in helping to understand shortcomings of other methods.

The QMC methods have a common link with the well established classical Monte Carlo methods: the use of randomly sampled numbers. Monte Carlo methods comprise a whole range of statistical techniques [NEWMAN 1999] and have already been successfully applied to a variety of problems, involving stochastic behavior ranging from science (e.g. kinetic Monte Carlo), engineering (e.g. treatment of real-world industrial problems) to economics (e.g. modeling financial markets)[DUBI 1999].

## Physics of Molecular Bonds - Results (Chapter 4)

The focus of this thesis is to investigate the accuracy and capability of the VMC and DMC methods in the CHAMP<sup>6</sup> implementation when describing various physical prop-

---

<sup>3</sup>K. Raghavachari, D. Strout, G. Odom, G. Scuseria, J. Pople, B. Johnson, P. Gill, Chem. Phys. Lett. Vol. 214 357 (1993)

<sup>4</sup>J. Grossman, L. Mitas and K. Raghavachari, Phys. Rev. Lett, Vol. 75 3870 (1995)

<sup>5</sup>R. Murphy, R. Friesner, Chem. Phys. Lett. Vol. 288 403 (1998)

<sup>6</sup>Cornell-Holland Ab-initio Materials Package by Claudia Filippi and Cyrus Umrigar, [www.lorentz.leidenuniv.nl/~filippi/champ.html](http://www.lorentz.leidenuniv.nl/~filippi/champ.html)

erties of small molecules. In particular, we investigate binding energies, equilibrium geometries and vibrational frequencies. As of this writing, binding energies calculated with QMC methods have been investigated only in few studies. To date, the largest systematic study, 55 molecules by Grossman [GROSSMAN 2002], found an average absolute deviation of 0.1 eV (2.9 kcal/mol) in the molecular binding energy compared to experimental data. This study used fixed-node DMC with a single determinant trial wavefunction and pseudopotentials. Another QMC study by Filippi and Umrigar [FILIPPI 1996] investigated total energies for seven first-row homo-nuclear diatomic molecules. For these molecules, the average absolute deviation is 0.73 eV (17 kcal/mol) from the exact, non-relativistic energy. Thereby, an all-electron DMC calculation with a trial wavefunction of 17 determinants was chosen. Further studies about total and binding energies with QMC have been undertaken on specific molecules, some of which will be mentioned later on.

Inter-atomic forces (i.e. equilibrium geometries and molecular vibrational frequencies) have been less studied with QMC. The reason for that is the difficulty for QMC methods when calculating small energy differences (in the order of several  $\mu\text{eV}$ ) between points on the potential energy surface. And these differences require a very high statistical accuracy. To my knowledge, there are only two papers that calculate vibrational frequencies with DMC. Ref. [SCHAUTZ 1998] presents vibrational frequencies for  $\text{Zn}_2$  and  $\text{Cd}_2$  that are obtained with pure DMC (a different method than the one used in this work). They are determined with a statistical error bar of 5-10% and reproduce the experimental value within that error. Yet, for a third molecule,  $\text{Hg}_2$ , the best estimate for the vibrational frequency underestimates the experimental value by 15%. The second recently published Ref. [LU 2003] predicts already better results. For  $\text{N}_2$ , the calculated vibrational frequency is in agreement with experimental data with a statistical error of 1.6%. In this reference, a DMC method was used that is based on floating spherical Gaussians (different than our DMC method).

In this thesis, we are interested in investigating these inter-atomic forces with a recently developed correlated sampling method [FILIPPI 2000]. For both, VMC and DMC, this method essentially samples differences in the total energy, i.e. between a reference geometry and an adjacent geometry. With this method, the equilibrium geometries as well as fundamental vibrational frequencies will be calculated for the diatomic molecules  $\text{H}_2$ ,  $\text{O}_2$ ,  $\text{N}_2$  and  $\text{CO}$  and the tri-atomic molecule  $\text{H}_2\text{O}$ .

These molecular ground-state properties are mostly determined by covalent bonds that have typical binding energies of several eV. A different type of bond are hydrogen-bonds which are one order of magnitude weaker than covalent bonds. In this thesis, we will use the VMC and DMC method to examine two model systems for H-bonds: diammonia and malonaldehyde. In particular, we will investigate the H-bond strength and the proton transfer barrier for these two molecules. Both, H-bonding and the proton transfer are important in the understanding of biochemical systems and in determining the functionality of proteins [JEFFREY 1994]. Because of such importance,

much attention has been paid to these particular bonds by experimentalists as well as theoreticians [SCHEINER 1997].

So far, standard DFT approaches with approximated exchange-correlation functionals, like BLYP and B3LYP [BARONE 1996, TSUZUKI 2001] or PBE and PBE-LDA functionals [ISMER 2002], yield energy barriers for the proton transfer that are too low. In our model systems, they are more than 0.04 eV (or several tens of percent) lower compared to very accurate CC or CI calculations. Whereas H-bonding strengths are well described by DFT PBE within about 0.04 eV for our two systems [ISMER 2002], which is also true for a larger set of molecules [TUMA et al. 1999].

In particular for di-ammonia, several equilibrium geometries have been suggested based on different quantum chemical methods and basis sets [TSUZUKI 2001]. These suggestions are energetically within 0.04 eV (1kcal/mol) and thus close to each other. Here, we will investigate two different structures for di-ammonia which are previously obtained by two DFT methods [ISMER 2002]. In this study, we compare our calculations with elaborate CC calculations where available.

## Methodological Investigations of our QMC Calculations (Chapter 5)

The DMC method in principle provides exact solutions to the many-electron problem. However, in practice several approximations are typically used to increase the efficiency of VMC and DMC. Three approximations are important: (1) the fixed-node approximation (2) the use of pseudopotentials and (3) the approximation of short time steps in the time evolution in DMC.

(1) The fixed node-approximation is a fundamental approximation specific to DMC. It allows for a convenient approach to impose anti-symmetry conditions on the many-particle wavefunction when treating fermion systems in DMC. It keeps the nodal surface from an initially chosen trial wavefunction (such as given by a HF calculation) as boundary condition in the calculated DMC ground state wavefunction. The fixed-node approximation always introduces a positive error in the total energy. A typical value of that error is estimated to be about 5% of the correlation energy when starting with a HF trial wavefunction [FOULKES 2001].

(2) All-electron QMC calculations have been applied to first row molecules<sup>7</sup> in few studies. One example was the earlier cited Ref. [FILIPPI 1996] with an average absolute deviation of 0.73 eV from the exact, non-relativistic total energy. Another Ref. [MANTE 2001] shows total energies for 20 first row molecules for (single Slater determinant) DMC calculations. For N<sub>2</sub> and F<sub>2</sub>, which are also calculated in the previous study, the results are not significantly different. These studies reflect the difficulty for accurate all-electron calculations with DMC already for first row molecules. Furthermore, the computational cost increases severely with the nuclear charge,  $Z$ . For DMC,

---

<sup>7</sup>In physics, the first row elements are Li till Ne (while in chemistry, they are identified as second row elements).

estimates range from  $Z^{5.5}$  to  $Z^{6.5}$  [LESTER 1994] and all-electron calculations quickly become intractable in reaching a fixed accuracy in the energy. Introduced to QMC by [BACHELET 1989]), pseudopotentials drastically increase the efficiency of QMC algorithms. An estimate of the scaling in DMC is given by  $N^3$ , where  $N$  is the number of valence electrons [MITAS 1991]. Generally, the pseudopotential approximation can be controlled for VMC calculations. Not so for DMC, there the non-locality of the pseudopotential poses larger difficulties due to the introduced localization. An estimate of that error is difficult due to its unknown sign.

(3) The short time approximation allows to use an efficient expression for the Greens function when solving the Schrödinger equation in DMC. A state of the art implementation of this approximation will be used in our calculations [UMRIGAR et al. 1993]. But other than for the two previous approximations, the influence of this short time approximation can be controlled and eliminated for DMC calculations.

As a consequence of these approximations, the VMC and DMC methods investigated in this thesis yield results that rely on various factors. These are the used representation of the trial wavefunction (i.e. the chosen correlation factor that improves the constructed trial wavefunction, the basis sets of the determinantal part of the trial wavefunction, or the chosen number of determinants of the determinantal part), and the type of pseudopotentials chosen.

Some studies have investigated and discussed such influences upon the QMC results like Refs.[GROSSMAN 2002, MITAS 1991, FILIPPI 1996]. However, there is still a need for further assessment of the accuracy and reliability when using these approximations. The last chapter of this thesis is devoted to examine these dependencies. We discuss our findings through the various results obtained upon the use of different correlation factors, basis sets, pseudopotentials, number of determinants and time steps. Thereby, we discuss the influence on our QMC results.

# Chapter 2

## Many-Particle Problem

This chapter provides theoretical foundations about dealing with the many-particle problem in quantum mechanics. First, we discuss the Born-Oppenheimer approximation which separates the electron and nuclear motion. This separation is important to make later QMC calculations more efficient. Then two conventional methods Hartree Fock and Configuration Interaction are briefly reviewed. Both methods yield solutions to the many-particle problem and are starting points for later QMC calculations. This chapter ends with a qualitative introduction of electron correlation.

### 2.1 The Schrödinger Equation

The many-particle time independent Schrödinger equation for  $N$  electrons at positions<sup>1</sup>  $\mathbf{r} = (\mathbf{r}_1, \dots, \mathbf{r}_N)$  and  $M$  nuclei at positions  $\mathbf{R} = (\mathbf{R}_1, \dots, \mathbf{R}_M)$  is given by the many-particle Hamiltonian  $\hat{H}$ ,

$$\hat{H}(\mathbf{r}, \mathbf{R})\Psi_\kappa(\mathbf{r}, \mathbf{R}) = E_\kappa\Psi_\kappa(\mathbf{r}, \mathbf{R}). \quad (2.1)$$

The many-particle wavefunction,  $\Psi_\kappa$ , describes the probability distribution of the  $N+M$  particles and  $\kappa$  indicates the eigenvectors and values. The many-particle Hamiltonian consists of five terms,

$$\hat{H}(\mathbf{r}, \mathbf{R}) = \hat{T}^e(\mathbf{r}) + \hat{T}^{\text{Ion}}(\mathbf{R}) + \hat{V}^e(\mathbf{r}) + \hat{V}^{e-\text{Ion}}(\mathbf{r}, \mathbf{R}) + \hat{V}^{\text{Ion}}(\mathbf{R}), \quad (2.2)$$

which are explicitly given by

---

<sup>1</sup>This notation will be strictly used throughout this thesis, where vectors with subscripts refer to single particles and vectors without subscripts refer to a set of particles.

$$\begin{aligned}\hat{T}^e &= \frac{1}{2} \sum_{i=1}^N (-\nabla_{\mathbf{r}_i}^2), & \hat{T}^{\text{Ion}} &= \frac{1}{2} \sum_{\alpha=1}^M (-M_\alpha \nabla_{\mathbf{R}_\alpha}^2), & \hat{V}^e &= \frac{1}{2} \sum_{i,i',i \neq i'}^{N,N'} \frac{1}{|\mathbf{r}_i - \mathbf{r}_{i'}|}, \\ \hat{V}^{e-\text{Ion}} &= \sum_{i=1, \alpha=1}^{N,M} \frac{-Z_\alpha}{|\mathbf{R}_\alpha - \mathbf{r}_i|} & \text{and} & & \hat{V}^{\text{Ion}} &= \frac{1}{2} \sum_{\alpha, \beta, \alpha \neq \beta}^{M,M'} \frac{Z_\alpha Z_\beta}{|\mathbf{R}_\alpha - \mathbf{R}_\beta|}.\end{aligned}\quad (2.3)$$

$\hat{T}^e$  is the kinetic and  $\hat{V}^e$  the potential electronic energy,  $\hat{T}^{\text{Ion}}$  is the kinetic and  $\hat{V}^e$  the potential nuclear energy and  $\hat{V}^{e-\text{Ion}}$  is the electron-nuclear potential.<sup>2</sup>  $Z_\alpha$  is the nuclear charge and  $M_\alpha$  is the nuclear mass with  $\alpha = 1, \dots, M$ .<sup>3</sup> QMC methods in principle would be already capable to solve eq.(2.1) via a statistical approach. Yet, the fundamental Born-Oppenheimer approximation further allows to separate the electron and nuclear motion and thereby to separate the Schrödinger equation accordingly.

## 2.2 Born-Oppenheimer Approximation

The Born-Oppenheimer approximation is based on the large difference between the electron and the nuclear mass. To see that it separates the treatment of electrons and nuclei, we first define the Hamiltonian  $\hat{H}^e(\mathbf{r}, \mathbf{R})$  for a set of fixed nuclear parameters  $\mathbf{R}$ ,

$$\hat{H}^e(\mathbf{r}, \mathbf{R}) \phi_\nu(\mathbf{r}, \mathbf{R}) = E_\nu^e(\mathbf{R}) \phi_\nu(\mathbf{r}, \mathbf{R}) \quad (2.4)$$

$$\text{with } \hat{H}^e(\mathbf{r}, \mathbf{R}) = \hat{T}^e(\mathbf{r}) + \hat{V}^e(\mathbf{r}) + \hat{V}^{e-\text{Ion}}(\mathbf{r}, \mathbf{R}) + \hat{V}^{\text{Ion}}(\mathbf{R}). \quad (2.5)$$

Here,  $\phi_\nu$  is the wavefunction of the electrons in the limit  $m/M_\alpha \rightarrow 0$ .  $\nu \in \mathbb{N}$  labels the different electronic eigenfunctions and values. Now, the many-particle wavefunction,  $\Psi_\kappa$ , can be expanded in the basis of these eigenfunctions  $\phi_\nu$ ,

$$\Psi_\kappa(\mathbf{r}, \mathbf{R}) = \sum_{\nu} \chi_{\nu\kappa}(\mathbf{R}) \phi_\nu(\mathbf{r}, \mathbf{R}), \quad (2.6)$$

with expansion coefficients  $\chi_{\nu\kappa}$ , where  $\mathbf{R}$  are fixed nuclear parameters. Now, we apply the many-particle Hamiltonian (2.1) to  $\Psi_\kappa$ , multiply with  $\phi_\mu^*$  from the left and integrate over all electron coordinates. Thereby, the many-particle Hamiltonian reduces to the **nuclear Schrödinger equation**,

$$\hat{H}^{\text{Ion}} \chi_{\mu\kappa} = (E_\mu^e(\mathbf{R}) + \hat{T}^{\text{Ion}}(\mathbf{R})) \chi_{\mu\kappa} - \quad (2.7)$$

$$\sum_{\nu} \sum_{\alpha=1}^M \left[ \frac{\hbar^2}{2M_\alpha} \langle \phi_\mu | \nabla_{\mathbf{R}_\alpha} | \phi_\nu \rangle \nabla_{\mathbf{R}_\alpha} + \langle \phi_\mu | \frac{\hbar^2 \nabla_{\mathbf{R}_\alpha}^2}{2M_\alpha} | \phi_\nu \rangle \right] \chi_{\nu\kappa} = E_{\mu\kappa} \chi_{\mu\kappa}. \quad (2.8)$$

<sup>2</sup>Throughout the entire work, atomic units will be used with  $\hbar = m = c = e = 4\pi\epsilon_0 = 1$ , unless otherwise noted.

<sup>3</sup>In this and subsequent equations, Greek and Latin indices will be used for nuclei and electrons, respectively.

The nuclear wavefunctions,  $\chi_{\mu\kappa}$ , are dependent on  $E_\mu^e$  (indicated by  $\mu$ ) and on  $\kappa$ , which labels the nuclear eigenfunctions and -values. The last two terms describe the electron-phonon coupling that interlinks the electron wavefunctions with nuclear motion. The first of the last two terms would give rise to the electronic transition induced by the nuclear motion. The second term would give a contribution to the electronic kinetic energy again caused by the nuclear motion. Both terms are set to zero within the Born-Oppenheimer approximation. To argue for leaving out the first term, we use the fact that all later systems are calculated at zero temperature. Thereby, the system is limited to the electronic ground state  $\phi_{\mu=0}$  and no electronic transition will be neglected when leaving out that term. For leaving out the second kinetic energy term, the general argument is the large difference in the electron and nuclear mass such that  $\frac{m}{M_\alpha} < 10^{-3}$ . When now approximating that second term as  $\frac{m}{M_\alpha} \langle \phi_0 | \frac{\hbar^2}{2m} \nabla_{\mathbf{r}_k}^2 | \phi_0 \rangle$  (where  $\nabla_{\mathbf{R}_\alpha}$  is replaced by  $\nabla_{\mathbf{r}_k}$ ), we see that this term is about three orders of magnitude smaller than the one by the electronic kinetic energy. Hence, the second term can be neglected. Another argument for disregarding this term is found in referring to the nuclear motion at zero temperature. In this limit, only small nuclear vibrations are allowed due to the zero point motion. Consequently, the coupling between the nuclei and electrons is small and the Born-Oppenheimer approximation acts as a good approximation [SCHERZ 1999]. This approximation now reduces the nuclear Schrödinger equation to<sup>4</sup>

$$(\hat{T}^{\text{Ion}} + E_0^{\text{BOS}}(\mathbf{R}))\chi_{0\kappa}(\mathbf{R}) = E_0^{\text{tot}}\chi_{0\kappa}(\mathbf{R}), \quad (2.9)$$

where we introduce the (ground state) **Born-Oppenheimer surface** (BOS),  $E_0^{\text{BOS}} := E_0^e$ . It describes the effective potential which governs the dynamics of the nuclei. Within the Born-Oppenheimer approximation, eq.(2.4) is now justified to be the **electronic Schrödinger equation**, parameterized by a set of fixed nuclear geometries,  $\mathbf{R}$ . And  $E_0^{\text{tot}}$  in eq.(2.9) is now the total ground state energy consisting of the electronic energy from eq.(2.4) and the kinetic contributions from the nuclei.

## 2.3 Hartree-Fock

Now, we want an approximate solution of the many-electron wavefunction. The most simple representation is a single Slater determinant. It goes beyond the treatment of effectively independent electrons in accounting for the Pauli principle (i.e. an anti-symmetry of the wavefunction). The Slater determinant can be written as

$$\Psi^{\text{SD}}_{k_1, \dots, k_N}(\mathbf{r}_1, \dots, \mathbf{r}_N) = \frac{1}{\sqrt{N!}} \sum_{\eta \in \mathcal{P}} \text{sign}(\eta) \psi_{k_{\eta(1)}}(\mathbf{r}_1) \psi_{k_{\eta(2)}}(\mathbf{r}_2) \cdots \psi_{k_{\eta(N)}}(\mathbf{r}_N), \quad (2.10)$$

<sup>4</sup>In this and subsequent equations, the nucleus-nucleus potential energy is included in  $E_0^{\text{BOS}}$ , as defined in eq.(2.4).

with the electron orbitals  $\psi_{k\sigma} = \phi_k \otimes \chi_\sigma$ , where  $\phi_k$  is the spatial and  $\chi_\sigma$  the spin part of the orbital, and  $k$  is the spatial and  $\sigma$  the spin quantum numbers.  $\eta$  is one out of all possible permutations  $\mathcal{P}$  of  $(1, \dots, N)$ . The Hartree Fock (HF) total energy  $E_0^{\text{HF}}$  is now given by the expectation value of  $\hat{H}^e$  with respect to a Slater Determinant,

$$E_0^{\text{HF}}[\{\phi_k\}] = \langle \Psi^{\text{SD}} | \hat{H}^e | \Psi^{\text{SD}} \rangle \quad \text{with} \quad \langle \Psi^{\text{SD}} | \Psi^{\text{SD}} \rangle = 1. \quad (2.11)$$

In order to derive the **Hartree Fock (HF) equations** from eq.(2.11), one has to take the functional derivative with respect to the  $\phi_k$  [SCHERZ 1999], and obtains<sup>5</sup>

$$\left[ -\frac{1}{2}\nabla^2 + \hat{v}_{\text{ext}}(\mathbf{r}) + \hat{v}_{\text{loc}}^{\text{H}}(\mathbf{r}) + \hat{v}_{\text{nloc}}^{\text{X}} \right] \phi_k(\mathbf{r}) = \varepsilon_k \phi_k(\mathbf{r}). \quad (2.12)$$

$\hat{v}_{\text{ext}}$  is the external potential,  $\hat{v}_{\text{loc}}^{\text{H}}$  is the local Coulomb or Hartree potential, and  $\hat{v}_{\text{nloc}}^{\text{X}}$  the non-local exchange or Fock operator. The latter two operators are explicitly given by

$$\hat{v}_{\text{loc}}^{\text{H}}(\mathbf{r}) := \sum_{j=1}^N \int_{\mathbb{R}^3} \frac{|\phi_j(\mathbf{r}')|^2}{|\mathbf{r} - \mathbf{r}'|} d^3\mathbf{r}' \quad (2.13)$$

$$\text{and} \quad (\hat{v}_{\text{nloc}}^{\text{X}} \phi_k)(\mathbf{r}) = \int \hat{v}_{\text{nloc}}^{\text{X}}(\mathbf{r}, \mathbf{r}') \phi_k(\mathbf{r}') d^3\mathbf{r}' \quad (2.14)$$

$$\text{with} \quad \hat{v}_{\text{nloc}}^{\text{X}}(\mathbf{r}, \mathbf{r}') := - \sum_{j=1}^N \delta_{\sigma\sigma_j} \frac{\phi_j^*(\mathbf{r}')}{|\mathbf{r} - \mathbf{r}'|} \phi_j(\mathbf{r}). \quad (2.15)$$

The eigenvalues,  $\varepsilon_k$ , and orbitals,  $\phi_k$ , are determined via a self-consistent solution of eq.(2.12) to (2.15). Then, the ground state energy can be written as

$$E_{\text{HF}} = \sum_k^N \varepsilon_k - (E^{\text{H}} + E^{\text{X}}), \quad \text{where} \quad (2.16)$$

$$E^{\text{H}} = \frac{1}{2} \sum_i^N \int_{\mathbb{R}^3} \hat{v}_{\text{loc}}^{\text{H}}(\mathbf{r}) |\phi_i(\mathbf{r})|^2 d^3\mathbf{r} \quad \text{and} \quad E^{\text{X}} = - \frac{1}{2} \sum_i^N \int_{\mathbb{R}^3} (\hat{v}_{\text{nloc}}^{\text{X}} \phi_i^*)(\mathbf{r}) \phi_i^*(\mathbf{r}) d^3\mathbf{r} \quad (2.17)$$

are the Hartree and exchange energy, respectively. There are three approaches to include the spin state when solving the HF eq.(2.12). The **Restricted HF (RHF)** assigns two electrons with different spins to the same orbital, thus limiting this approach to an electronic system with a closed shell. This is different from **Restricted**

---

<sup>5</sup>It should be said that the spatial orbitals,  $\phi_k$ , in the following eq.(2.12) are in general different from the ones before and result from a unitary transformation required to uncouple the orbitals,  $\phi_k$  [SCHERZ 1999].



**Open-shell HF (ROHF)**, that allows placement of unpaired, additional electrons in outer orbitals. **Unrestricted HF (UHF)** has different orbitals for both spins allowing for more variational freedom, but the UHF wavefunction thereby loses its character of being a spin eigenstate.

## 2.4 Configuration Interaction

The many-electron wavefunction can now further be improved by including more determinants. This is done in the Configuration Interaction (CI) method which replaces  $\Psi^{\text{SD}}$  in eq.(2.11) by  $\Psi^{\text{CI}}$ , where  $\Psi^{\text{CI}}$  is based on such an expansion of possible  $N$ -electron determinants. The coefficients for all determinants are again determined variationally so as to minimize the total energy. Thereby, the determinants may be constructed from  $M$  molecular orbitals (MO) previously obtained from a HF calculation, where  $M$  enumerates the included ground- and excited states. For a given set of  $M$  MOs, a full CI wavefunction then requires

$$\frac{(2M)!}{N!(2M - N)!} \quad (2.18)$$

determinants to describe an  $N$ -electron system [JENSEN 2002]. And  $\Psi^{\text{CI}}$  only corresponds to the true many-electron wavefunction if  $M \rightarrow \infty$  which is beyond numerical handling. But when considering the example of an  $\text{N}_2$  molecule (even when using a pseudopotential to reduce the number of electrons to  $N = 10$ ), a full CI description still requires 30 million determinants when limiting the number of MOs to the first 10 excited MOs (or 850 million determinants, when considering the first 15 excited MOs). From that requirement, it is obvious that the CI method becomes numerically intractable when thoroughly studying molecules for an increasing numbers of electrons (and MOs). For an elaborate CI study, Ref. [TSUZUKI 2001] gives a current limit of 20 first row atoms.

## 2.5 Electron Correlation

We will see in the later discussion that the electron correlation has a substantial contribution when determining molecular properties, like binding energies. There are two reasons that account for electron correlations. Electrons as fermion particles must obey the anti-symmetry requirement of the wavefunction (Pauli principle). The associated correlation is called Fermi correlation. Electrons as charged particles are subject to the Coulomb interaction. And this interaction gives rise to the Coulomb correlation between electrons.

### Fermi Correlation

The anti-symmetry requirement of the wavefunction for fermions (Pauli principle) prevents like spin electrons from being found at the same position in space. Within the HF theory, such an anti-symmetric wavefunction is approximated by a single Slater determinant. And the correlation described by this Slater determinant between like spin electrons gives rise to the electronic exchange energy in eq.(2.17). This correlation caused by a Slater determinant is often referred to as Fermi correlation. The Fermi correlation neglects any interaction between electrons with opposite spin (e.g. the exchange energy vanishes for electrons with opposite spin). Hence, electrons with opposite spin are treated as effectively independent particles in HF.

### Coulomb Correlation - Dynamic and Static Correlation

The treatment of electrons (with opposite spins) as independent particle in HF is approximated by the interaction between one electron and an average field generated by the remaining independent electrons (discussed in Ref. [KOCH 2001]). This field is static and neglects the influence of the motion of one electron on the motion of the other electrons and vice versa. This treatment results in an electron pair density that is too large for small distances and too small for large distances. Consequently, the electron-electron repulsion and thus the Hartree energy in eq.(2.17) gives an additional positive contribution so that  $E_{\text{HF}}$  overestimates the exact total energy. Therefore, a correct “dynamic” electron description (such as approximated with a later DMC ground state or full CI wavefunction) lowers the total energy. This correlation is also referred to as **dynamic correlation**.

The **static correlation** is an expression commonly used in quantum chemistry. It is defined as the missing contribution of the total non-relativistic energy that is not described by Fermi and dynamic correlation. One possible way of understanding the static correlation is when a single HF Slater determinant fails to properly describe a physical system. In these cases, adding (one or two) determinants helps to reduce that shortfall. An emblematic illustration of such cases can be already found by  $\text{H}_2$  when using RHF (discussed in Ref.[HAKEN 2000]). In this example, adding a second determinant avoids the simultaneous placement of two electrons at the same nucleus. This results for a substantial lowering of the total energy. Due to this interpretation, the static correlation is also called left-right correlation [KUTZELNIGG 1992].

Following the standard practice in quantum chemistry, we define **correlation energy**,  $E_{\text{corr}}$ , as the difference between the Hartree-Fock energy,  $E_{\text{HF}}$ , in eq.(2.16) and a more accurate total energy (such as given by CI or QMC calculations)<sup>6</sup>

$$E_{\text{corr}} = E_{\text{CI or QMC}} - E_{\text{HF}}. \quad (2.19)$$

---

<sup>6</sup>This definition is taken from Ref. [NIST 2003] and goes back to E. Wigner, F. Seitz, Phys. Rev. 43, 804 (1933).

$E_{\text{corr}}$  has its maximum (exact) value when  $E_{\text{CI or QMC}}$  approaches the true non-relativistic total energy. Other definitions for  $E_{\text{corr}}$  exist, mostly used by physicists, which include the HF exchange energy.<sup>7</sup>

---

<sup>7</sup>For clarity, I like to mention that the treatment of the exchange interaction is generally different between HF and the Kohn-Sham Density Functional Theory (KS-DFT). In KS-DFT, the one-particle orbitals are derived from a multiplicative local potential (KS-potential including a local exchange potential). In the HF theory, however, the exchange is represented by a non-local Fock operator. Therefore, the DFT and HF one-particle orbitals are different in general. Correspondingly, the total energy (and its components like the exchange and correlation energy) in DFT and post-HF or QMC methods differs. According to Ref. [GRABO 1999], it holds for example the following inequality

$$E_{\text{tot}}^{\text{HF}}[\{\phi_i\}_{i=1,\dots,N}] \leq E_{\text{tot}}^{\text{DFT-X}}[n].$$

In this inequality,  $E_{\text{tot}}^{\text{HF}}$  is the HF total energy from eq.(2.16) which depends on the single-particle orbitals.  $E_{\text{tot}}^{\text{DFT-X}}[n]$  depends on the density  $n$  and is the total energy in DFT that only includes exchange functionals, see also Ref. [KOCH 2001]. However, in this thesis we will use the exchange energy always according to the HF theory.



# Chapter 3

## Theory of QMC

The last section introduced the many-particle problem in quantum mechanics and two standard quantum chemical approaches HF and CI that yield (approximate) solutions to it. Alternative approaches are the two Monte Carlo methods, VMC and DMC, which will be presented in this section. Both methods require the evaluation of multi-dimensional integrals when solving the Schrödinger eq.(2.9). Since these integrals are high dimensional as illustrated in the introduction of this thesis, standard quadrature rules become inappropriate. An alternative to these standard quadrature rules is Monte Carlo Integration (MCI), that will be introduced at the beginning of this chapter. MCI then provides the key concept for both VMC and DMC methods. Both latter methods will then be introduced followed by a discussion of the use of pseudopotentials. This chapter ends by presenting the correlated sampling VMC and DMC method.

### 3.1 Monte Carlo Integration

The Monte Carlo Integration (MCI) method is based on a statistical approach to evaluate high dimensional and/or non-analytic integrals. We will begin with relevant statistical foundations that give rise to the concept of MCI, followed by its implementation as it is used in this thesis.

#### 3.1.1 Statistical Foundations

The basic principle used by MCI is the simple **mean value theorem**. When applying that theorem in one dimension, an integral

$$I = \int_p^q f(x)dx \tag{3.1}$$

can be approximated as

$$I \approx (q - p) \cdot \bar{f} \quad \text{with} \quad \bar{f} = \frac{1}{M} \sum_{i=1}^M f(x_i), \quad (3.2)$$

where  $x_i$  are appropriate **sampling points** covering the integration domain  $[p, q]$ . It is apparent that the approximation is exact in the limit of large  $M$ . The important point, that distinguishes MCI from conventional numerical integration methods, is the random selection of these sampling points. This selection allows the application of the central limit theorem (A.11) when calculating the mean value  $\bar{f}$  in eq.(3.2). It guarantees a Gaussian distribution of the mean with **standard deviation**

$$\sigma_{\bar{f}} = \sqrt{\frac{\frac{1}{M-1} \sum_{i=1}^M [f(x_i) - \bar{f}]^2}{M}}. \quad (3.3)$$

It is important to notice the decrease of  $\sigma_{\bar{f}}$  with  $\frac{1}{\sqrt{M}}$  independently of the dimension of the integral. When comparing with the conventional trapezoidal integration rules with uniform grid points, the standard deviations decrease with  $\frac{1}{\sqrt[d]{M^2}}$  [PRESS 2002]. Hence, for dimensions  $d$  larger than four, MCI is already more efficient<sup>1</sup>.

### 3.1.2 Importance Sampling

The efficiency of MCI extensively improves when choosing **importance sampled** points. The idea is to select sampling points that yield large values of  $f$  and thus larger contributions to the integral  $I$ . Points with small values in  $f$  are neglected.

Let us consider the one-dimensional integral over  $f$  again. First, one considers another function  $g$  that reasonably approximates  $f$  (i.e.  $g \approx f$ ). Now, one chooses sampling points according to the following probability distribution function,

$$\rho(x) := \frac{g(x)}{\int_p^q g(x) dx}, \quad (3.4)$$

which is constructed from  $g$ . The integral  $I$  in eq.(3.1) can then be re-written,

$$I = \int_p^q \frac{f(x)}{\rho(x)} \rho(x) dx = \int_p^q \hat{f}(x) \rho(x) dx, \quad (3.5)$$

when introducing  $\hat{f} := \frac{f}{\rho}$ . The last integral expression for  $I$  can be interpreted as expectation value or weighted average of  $\hat{f}$  with respect to a distribution function,  $\rho$ .

---

<sup>1</sup>In addition to the more efficient convergence of  $\sigma_{\bar{f}}$ , the example in the introduction also illustrated the impossibility to manage the amount of uniform grid points in 84 dimensions.

That modified integral can be calculated in analogy to expression (3.2) as the average value of  $\hat{f}$ ,

$$I \approx \frac{1}{M} \sum_{i=1}^M \hat{f}(y_i), \quad (3.6)$$

with the important difference, that the sampling points  $\{y_i\}_{i=1,\dots,M}$  have to be taken from the probability distribution  $\rho$ .

Importance sampling has an important advantage compared to a uniform selection of sampling points. The modified integrand  $\hat{f}$  is approximately independent of  $y$  and its fluctuation is largely reduced. In turn when approximating the integral with the mean value of  $\hat{f}$ , the standard deviation of the mean of  $\hat{f}$  is much smaller than for a (uniform) randomly sampled integrand  $f$ . This importance sampling technique therefore reduces the amount of required sampling points and thereby the numerical effort.

Several methods now exist to find sampling points according to a given distribution function,  $\rho$  [LESTER 1994]. One of those is the powerful Metropolis method used in this thesis.

### 3.1.3 Metropolis Algorithm

The Metropolis algorithm [METROPOLIS 1953] generates importance sampled points according to any given distribution function,  $\rho$ . The idea of that algorithm is

1. to take a randomly chosen point,  $\mathbf{r}$ , in the integration domain (configuration space),
2. to perform a random walk (trial move) from  $\mathbf{r}$  to  $\mathbf{r}'$  in the configuration space with  $\mathbf{r}' = \mathbf{r} + \boldsymbol{\chi}$ , where  $\boldsymbol{\chi}$  is a normally distributed random vector with a mean value of zero,
3. and to accept or reject that move according to a given acceptance rule (to be derived later on).
4. If the move is accepted, the given starting point,  $\mathbf{r}$ , becomes replaced with  $\mathbf{r}'$  and the whole process starts again with step 1 from  $\mathbf{r}'$ . If the move is rejected, that random trial move will be repeated starting again from  $\mathbf{r}$ .

This generation process yields sampling points according to the given distribution  $\rho$ . Figure 3.1 illustrates a set of 1000 sampling points generated for the electron density for the  $\text{N}_2$  molecule. Note that these sampling points,  $\mathbf{r}$ , are commonly called **walkers** in allusion to their generation process.

The acceptance rule is a central part in the Metropolis algorithm. To derive an expression for it, let us consider two points,  $\mathbf{r}$  and  $\mathbf{r}'$ , in the configuration space. Following

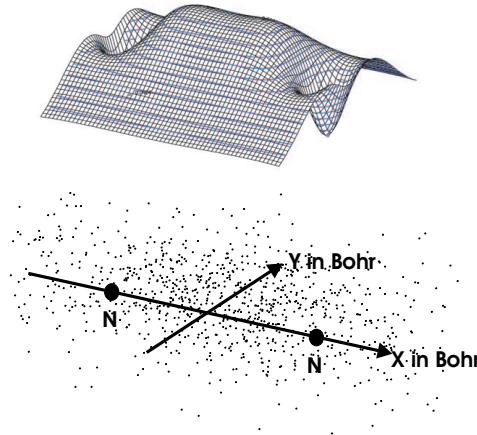


Figure 3.1: The upper plot shows the electron density for an  $N_2$  molecule obtained with a HF calculation. The lower plot shows 1000 walkers generated with the Metropolis algorithm and distributed in the configuration space of  $N_2$ . Since  $N_2$  has 10 valence electrons, its configuration space is  $3 \times 10$  dimensional and each of the walkers has  $3 \times 10$  dimensions. In order to plot these walkers as shown above, all walkers are projected to the x- and y- plane of the first electron.

Ref. [FOULKES 2001], one refers to a **steady equilibrium** if the probability of walkers moving from an infinitesimal volume  $d\mathbf{r}$  to  $d\mathbf{r}'$  is the same as for the reverse case from  $d\mathbf{r}'$  to  $d\mathbf{r}$  for one move.<sup>2</sup> Let us begin by describing a move of a walker from position  $\mathbf{r}$  (not a volume  $d\mathbf{r}$ ) into the volume  $d\mathbf{r}'$ . The total probability of that move can be written as,

$$G(\mathbf{r} \rightarrow \mathbf{r}') \cdot P(\mathbf{r} \rightarrow \mathbf{r}') \cdot d\mathbf{r}', \quad (3.7)$$

where  $G(\mathbf{r} \rightarrow \mathbf{r}')$  is the probability of the walker for moving from  $\mathbf{r}$  to  $\mathbf{r}'$  and is the Green function to be explicitly discussed in Section 3.3.  $P(\mathbf{r} \rightarrow \mathbf{r}')$  is the probability of accepting that move and represents the unknown acceptance rule we like to derive. Based on expression (3.7), the average number of walkers moving now from volume  $d\mathbf{r}$  to  $d\mathbf{r}'$  is given by multiplying that expression by  $\rho d\mathbf{r}$ ,

$$\rho(\mathbf{r})d\mathbf{r} \cdot G(\mathbf{r} \rightarrow \mathbf{r}') \cdot P(\mathbf{r} \rightarrow \mathbf{r}') \cdot d\mathbf{r}'. \quad (3.8)$$

$\rho$  is the walker density at  $\mathbf{r}$ . Now, in fulfillment of the previously described steady equilibrium, the following equality,

$$G(\mathbf{r} \rightarrow \mathbf{r}')P(\mathbf{r} \rightarrow \mathbf{r}')\rho(\mathbf{r}) = G(\mathbf{r}' \rightarrow \mathbf{r})P(\mathbf{r}' \rightarrow \mathbf{r})\rho(\mathbf{r}'), \quad (3.9)$$

---

<sup>2</sup>Attaining a steady equilibrium requires a sufficient large number of walkers. This is assumed here.



must hold for all  $\mathbf{r}$  and  $\mathbf{r}'$ . In order to satisfy that equation (i.e. the steady equilibrium), different choices for  $P(\mathbf{r} \rightarrow \mathbf{r}')$  exist. A typical choice is

$$P(\mathbf{r} \rightarrow \mathbf{r}') = \min \left\{ 1, \frac{G(\mathbf{r}' \rightarrow \mathbf{r})\rho(\mathbf{r}')}{G(\mathbf{r} \rightarrow \mathbf{r}')\rho(\mathbf{r})} \right\}. \quad (3.10)$$

With this choices, eq.(3.9) can be easily shown to hold [LESTER 1994].  $P(\mathbf{r} \rightarrow \mathbf{r}')$  is now the derived acceptance rule used in step 3. As stated above, the explicit form of  $G$  will be introduced and discussed in Section 3.3.<sup>3</sup>

This **Metropolis algorithm** can further be improved when modifying the proposition rule of a move,  $\mathbf{r} \rightarrow \mathbf{r}'$ , in step 2 by an “intelligent” proposal. That avoids a high rejection rate for otherwise “blind” suggestions. In particular, the proposition of a sampling point should favor points corresponding to an increase in the density,  $\rho$ , and disfavor points for decreasing,  $\rho$ . We will derive that improved proposition rule in a more general context for DMC in Section 3.3.3 but anticipate the result,

$$\mathbf{r}' = \mathbf{r} + \delta\tau \cdot \mathbf{v}(\mathbf{r}) + \chi. \quad (3.11)$$

Here,  $\mathbf{v}$  is the drift velocity given by  $\mathbf{v} := \rho^{-1}\nabla\rho$  (further discussed in Section 3.3.3) and  $\delta\tau$  is a constant time step. When choosing this improved proposition rule, the modified algorithm then becomes the **Metropolis algorithm with importance sampling** [LESTER 2001].

## 3.2 Variational Monte Carlo

The introduced HF and CI methods in Chapter 2 rely on wavefunctions that are constructed from single or multiple determinants. The Variational Monte Carlo (VMC) method presented in this section generalizes now this wavefunction ansatz that is purely based on determinants. The wavefunction used in VMC (later on called trial wavefunction  $\Psi_T$ ) is constructed from these determinants but additionally includes a multiplicative correlation factor. This factor aims at improving the dynamic correlation description of  $\Psi_T$ . However, this generalized representation of  $\Psi_T$  also leads to a complex and high-dimensional integral when evaluating the expectation value of the Hamilton operator,  $\langle \Psi_T | \hat{H} | \Psi_T \rangle$ , or of any other operator. To evaluate this integral, the introduced Monte Carlo Integration serves as a convenient and essential method. After the evaluation of that integral, the energy expectation value obtained for  $\Psi_T$  can further be improved by optimizing the free parameters of  $\Psi_T$  with an appropriate optimization algorithm. Thereby, the Ritz variation principle in quantum mechanics guarantees that the obtained minimum in the total energy is an upper bond of the true ground state energy.

The following section presents all relevant parts of a VMC calculation and concludes with a summary of the VMC algorithm used in this thesis.

---

<sup>3</sup>In this derivation, the explicit time dependence of the Greens function has been omitted.

### 3.2.1 Total Energy

The VMC total energy,  $E_{\text{VMC}}$ , is obtained by evaluating the expectation value of  $\hat{H}^e$  with respect to a trial wavefunction,  $\Psi_T$ . For a chosen expression for  $\Psi_T$ , the expectation value,  $E_{\text{VMC}}$ , can be expressed in integral form,

$$E_{\text{VMC}} = \frac{\int \Psi_T(\mathbf{r})(\hat{H}^e \Psi_T)(\mathbf{r}) d\mathbf{r}}{\int \Psi_T(\mathbf{r}) \Psi_T(\mathbf{r}) d\mathbf{r}} = \frac{\int |\Psi_T(\mathbf{r})|^2 \frac{(\hat{H}^e \Psi_T)(\mathbf{r})}{\Psi_T(\mathbf{r})} d\mathbf{r}}{\int |\Psi_T(\mathbf{r})|^2 d\mathbf{r}} = \frac{\int |\Psi_T(\mathbf{r})|^2 E_L(\mathbf{r}) d\mathbf{r}}{\int |\Psi_T(\mathbf{r})|^2 d\mathbf{r}}, \quad (3.12)$$

where the local energy,

$$E_L(\mathbf{r}) = \frac{(\hat{H}^e \Psi_T)(\mathbf{r})}{\Psi_T(\mathbf{r})}, \quad (3.13)$$

is introduced. Applying the importance sampled MCI from Section 3.1.2, the integral expression for  $E_{\text{VMC}}$  can now be approximated as sum,

$$E_{\text{VMC}} \approx \frac{1}{M} \sum_{i=1}^M E_L(\mathbf{r}^{(i)}), \quad (3.14)$$

where the MCI technique automatically integrates the local energy with respect to the weights,  $\frac{|\Psi_T|^2}{\int |\Psi_T|^2 d\mathbf{r}}$ . In the last sum,  $\mathbf{r}^{(i)}$  represents the  $i^{\text{th}}$  walker. Now, the next arising question is how to construct an appropriate trial wavefunction.

### 3.2.2 The Trial Wavefunction $\Psi_T$

The trial wavefunction,  $\Psi_T$ , should be as similar as possible to the true wavefunction to guarantee that  $E_{\text{VMC}}$  is close to the true ground state energy. But also, it is required that  $\Psi_T$  is more compact than a full-CI wavefunction with millions of determinants (Section 2.4). The idea in constructing  $\Psi_T$  with only a few parameters is to use the most important determinant(s) to properly describe static correlation. Then, an additional multiplicative factor, the **Jastrow factor**, tries to account for a description of the remaining dynamic correlation. Therefore, the trial wavefunction is commonly defined as the product between a sum of determinants and a Jastrow factor,

$$\Psi_T = \left( \sum_{n=1}^m d_n D_n \right) \cdot \mathcal{J}(\{r_{i\alpha}, r_{j\alpha}, r_{ij}\}). \quad (3.15)$$

$D_n$  represent the determinants and  $d_n$  are their respective coefficients with  $n = 1, \dots, m$ . In the case of  $m = 1$ , the sum reduces to the single HF Slater determinant. The second factor in eq.(3.15) is the Jastrow factor,  $\mathcal{J}$ . It depends on the electron-nucleus distance,  $r_{i\alpha}$ , and the electron-electron distance,  $r_{ij}$ , (the Latin indices count all  $N$  electrons and the Greek indices all  $M$  nuclei). The curly bracket in the argument of  $\mathcal{J}$  refers to the set of all possible indices for  $i, j$  and  $\alpha$ .

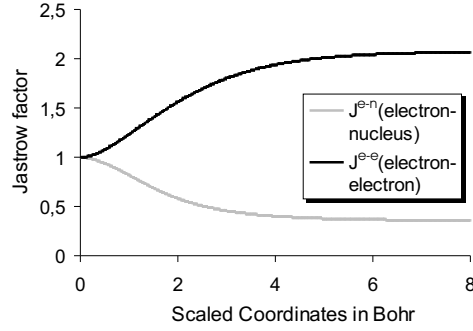


Figure 3.2: This figure shows the Jastrow factors  $\mathcal{J}^{e-e}$  and  $\mathcal{J}^{e-n}$  of the  $\mathcal{J}(550)$ -factor for an  $N_2$  molecule. The upper thicker line represents the Jastrow factor  $\mathcal{J}^{e-e}$  for the electron-electron correlation. The thin lower line represents the Jastrow factor  $\mathcal{J}^{e-n}$  for the electron-nucleus correlation. To avoid confusion, the reader should note that two different abscissa are used in that plot, i.e. for the e-e and the e-n distances.

There are several ways for choosing the Jastrow factor, stemming from both, mathematical simplicity and physical motivation. As we will discuss below, both criteria are well satisfied for the Jastrow factor utilized in this thesis,

$$\mathcal{J}(\{r_{i\alpha}, r_{j\alpha}, r_{ij}\}) = \mathcal{J}^{e-n} \cdot \mathcal{J}^{e-e} \cdot \mathcal{J}^{e-e-n} \quad (3.16)$$

$$= \overbrace{\prod_{i=1}^N \prod_{\alpha=1}^M e^{A_{i\alpha}}} \overbrace{\prod_{i,j=1}^N e^{B_{ij}}} \overbrace{\prod_{i,j=1}^N \prod_{\alpha} e^{C_{ij\alpha}}} \quad (3.17)$$

$$\text{with} \quad A_{i\alpha} = \sum_{n=2}^{n_A} a_{n\alpha} r_{i\alpha}^n, \quad (3.18)$$

$$B_{ij} = \frac{b_0 r_{ij}}{1 + b_1 r_{ij}} + \sum_{n=2}^{n_B} b_n r_{ij}^n \quad (3.19)$$

$$\text{and} \quad C_{ij\alpha} = P(c_{i\alpha}, r_{i\alpha}, r_{j\alpha}, r_{ij}). \quad (3.20)$$

The three Jastrow factors in eq.(3.16) describe the electron-nuclear (e-n), the electron-electron (e-e) and the electron-electron-nuclear (e-e-n) correlation. The polynomial parts of  $A_{i\alpha}$  and  $B_{ij}$  have orders  $n_A$  and  $n_B$  with  $(n_A - 1)$  and  $n_B$  free parameters  $a_{n\alpha}$  and  $b_n$ , respectively. (Later on, polynomials will be identified by their orders.) The last  $\mathcal{J}^{e-e-n}$ -factor in eq.(3.16) describes so called three-body correlations and is given by the polynomial  $P$  with coefficients  $c_{i\alpha}$ . Its quite complex construction is based on polynomials simultaneously consisting of (e-e) and (e-n) coordinates and is

omitted here (it can be found in Ref. [FILIPPI 1996]). Nevertheless, it is important to know that some  $c_{i\alpha}$  coefficients (parameters) are dependent on each other, e.g. for maintaining the anti-symmetry in the electron coordinates. Also, some  $c_{i\alpha}$  parameters replicate the two-body correlation from  $\mathcal{J}^{e-n}$  and  $\mathcal{J}^{e-e}$ . In turn, these parameters need to be ruled out when exclusively considering three body correlations. Table 3.1 shows the number of independent three body parameters,  $c_{i\alpha}$ , that belong to the respective order  $n_C$  of the polynomial  $P$ .

For the notation of later Jastrow factors, we will use the following convention. A Jastrow factor for example with five orders in all three polynomials,  $A_{i\alpha}$ ,  $B_{ij}$  and  $C_{ij\alpha}$ , will be denoted as  $\mathcal{J}(555)$  and has  $4 + 5 + 15 = 24$  independent parameters. Attention must be paid to the fact that hetero-nuclear molecules have one set of  $a_{i\alpha}$  and  $c_{n\alpha}$  for each species of atoms.

Orders $n_C$ in $P$	1	2	3	4	5	6
$c_{i\alpha}$	0	0	2	7	15	27

Table 3.1: This table shows the number of independent three body parameters  $c_{i\alpha}$  of  $\mathcal{J}^{e-e-n}$  which belong to the respective order  $n_C$  in  $P$ .

In order to prevent domination of polynomials by their highest-order term at large inter-particle distances, the Jastrow factor is written in terms of scaled coordinates,  $\tilde{r}_{i\alpha}$  and  $\tilde{r}_{ij}$ ,

$$\tilde{r}_{i\alpha} := \frac{1}{\kappa}(1 - e^{-\kappa r_{i\alpha}}) \quad (3.21)$$

$$\text{and } \tilde{r}_{ij} := \frac{1}{\kappa}(1 - e^{-\kappa r_{ij}}). \quad (3.22)$$

In this way, the interval  $[0, \infty[$  with  $r \in [0, \infty[$  is mapped onto the interval  $[0, \kappa^{-1}[$ . Therefore, the value of  $\mathcal{J}$  remains finite even for large distances  $r$ , where  $\kappa$  is a variational parameter that can be optimized similarly to the other parameters in the Jastrow factor.

The Jastrow factor defined in eq.(3.16) to (3.22) and used in this thesis fulfills important features (advantages). (1) It allows to construct a rather compact trial wavefunction with only a few parameters. (2) It provides the correct analytic behavior when two electrons or one electron and one nucleus approach each other (further discussed in the next subsection). (3) Consequently, it gives an appropriate description of dynamic correlations as introduced in Section 2.5. This is illustrated in Figure 3.2. There, the behavior of the two Jastrow factor components  $\mathcal{J}^{e-e}$  and  $\mathcal{J}^{e-n}$  of the  $\mathcal{J}(550)$ -factor is shown for the  $N_2$ -molecule. The upper thicker line represents  $\mathcal{J}^{e-e}$  and shows the reduced probability density of two electrons when they approach each other. This is equivalent to an increased repulsion and a larger average distance between two electrons. The thin lower line represents  $\mathcal{J}^{e-n}$  and "corrects" the effect caused by  $\mathcal{J}^{e-e}$  for

larger e-n distances. The remaining characteristics after multiplying these two components is a lowering in the electron density around each electron. And their effects cancel (the product of  $\mathcal{J}^{e-n}$  and  $\mathcal{J}^{e-e}$  becomes one) for larger distances. This is in accordance with the given picture of dynamic correlation in Section 2.5.

### 3.2.3 The Electron-Electron Cusp Condition

When using the previous expression of the Jastrow factor, one can already incorporate the exact characteristics of the true wavefunction in the limit of small distances between two electrons. This is favorable since  $\Psi_T$  in eq.(3.15) is generally not an exact representation of the true ground state. And the resulting local energy in eq.(3.13) may diverge as  $r_{ij} \rightarrow 0$ . The requirement on  $\Psi_T$  to keep the local energy finite in the limit for two approaching electrons is called the **electron-electron cusp condition**. This condition guarantees that the arising singularities in the Coulomb potential and in the kinetic energy do cancel appropriately. Its derivation can be found in Ref. [FOULKES 2001, FILIPPI 1996] and is stated for our Jastrow factor as follows,

$$b_0^{\uparrow\uparrow} = \frac{1}{2} \quad \text{and} \quad b_0^{\downarrow\uparrow} = \frac{1}{4}. \quad (3.23)$$

Here,  $b_0^{\uparrow\uparrow}$  applies for two electrons with like spin and  $b_0^{\downarrow\uparrow}$  applies for two electrons with anti-parallel spin. Both are coefficients in the  $B_{ij}$  polynomial of the  $\mathcal{J}^{e-e}$ -factor in eq.(3.19).

### 3.2.4 Wave Function Optimization

In the last sections, we have shown how to calculate the VMC total energy for a chosen trial wavefunction,  $\Psi_T$ . The optimization of  $\Psi_T$  is now the last step in a VMC calculation to obtain the optimized VMC total energy. Two different approaches exist, the variance and total energy minimization [LESTER 1994]. In the case where  $\Psi_T$  is the true wavefunction, both methods are equivalent due to the variation principle. If  $\Psi_T$  differs from the true wavefunction, it can be shown that energy minimization yields lower energies compared to variance minimization [Foulkes, private communication]. However, the variance minimization is found to be statistically more efficient in practice due to the positive definiteness of the variance, where zero is the minimum value [FOULKES 2001]. In this thesis, we use a combination of both methods that will be presented in the following.

#### Variance Minimization

According to Ref. [LESTER 1994], Variance minimization uses the inequality

$$E_{\text{VMC}}[\Psi_T] - \sigma[\Psi_T] \leq E_0 \leq E_{\text{VMC}}[\Psi_T] \leq E_{\text{VMC}}[\Psi_T] + \sigma[\Psi_T] \quad (3.24)$$

with the variance,  $\sigma^2$ , of the total energy given by

$$\sigma^2 = \frac{\int |\Psi_T|^2 (E_L - E_{\text{VMC}})^2 d\mathbf{r}}{\int |\Psi_T|^2 d\mathbf{r}} \approx \frac{1}{M} \sum_{i=1}^M (E_L(\mathbf{r}_i) - E_{\text{VMC}})^2. \quad (3.25)$$

In the last step, Monte Carlo Integration (MCI) has been applied and  $E_{\text{VMC}}$  is the previously defined VMC total energy from eq.(3.12). Both upper equations show that the variance vanishes if and only if the trial wave function is the true ground state of the Hamiltonian. In other words, if  $\Psi_T$  matches the exact ground state, the local energy becomes a constant and equals  $E_{\text{VMC}}$  such that the variance vanishes, and vice versa, if the variance is zero,  $\Psi_T$  must be exact.

When minimizing  $\sigma^2$  with respect to an initial set of variational parameters,  $\alpha^{(0)}$ , of the trial wavefunction, it is important to compare very small differences in  $\sigma^2$  in order to determine the optimal set of parameters,  $\alpha^*$ . This is achieved with an application of a correlated sampling approach. Thereby, the same set of walkers are used when proposing a new set of parameters,  $\alpha^{(1)}$ , and when evaluating the variance with these new parameters. This approach guarantees a greatly reduced statistical fluctuation when evaluating small quantitative changes in  $\sigma^2$ .<sup>4</sup>

This correlated sampling technique is introduced in the following. First, eq.(3.25) is written for the optimized set of parameters,  $\alpha^{(1)}$ ,

$$\sigma^2[\alpha^{(1)}] = \frac{\int \Psi_T^2[\alpha^{(1)}] (E_L[\alpha^{(1)}] - E_{\text{VMC}}[\alpha^{(1)}])^2 d\mathbf{r}}{\int \Psi_T^2[\alpha^{(1)}] d\mathbf{r}}. \quad (3.26)$$

When introducing the weight,

$$\omega[\alpha^{(0)}, \alpha^{(1)}] := \frac{\Psi_T^2[\alpha^{(1)}]}{\Psi_T^2[\alpha^{(0)}]}, \quad (3.27)$$

eq.(3.26) can be re-written as

$$\begin{aligned} \sigma^2[\alpha^{(1)}] &= \frac{\int \Psi^2[\alpha^{(0)}] (E_L[\alpha^{(1)}] - E_{\text{VMC}}[\alpha^{(1)}])^2 \omega[\alpha^{(0)}, \alpha^{(1)}] d\mathbf{r}}{\int \Psi^2[\alpha^{(0)}] \omega[\alpha^{(0)}, \alpha^{(1)}] d\mathbf{r}} \\ &\approx \frac{\sum_{i=1}^M (E_L - E_{\text{VMC}})^2 \omega[\alpha^{(0)}, \alpha^{(1)}]}{\sum_{i=1}^M \omega[\alpha^{(0)}, \alpha^{(1)}]}. \end{aligned} \quad (3.28)$$

---

<sup>4</sup>The numerical optimization of the variational parameters,  $\alpha$ , is performed by a combination of three standard numeric optimization techniques, i.e. Levenberg-Marquardt, Simulated Annealing and Metropolis Sampling. A discussion of these techniques is omitted here but can be found in Ref.s [UMRIGAR et al. 1988, PRESS 2002].

In the last step, MCI is used again. The important result now is that the two values  $\sigma^2[\alpha^{(0)}]$  in eq.(3.25) and  $\sigma^2[\alpha^{(1)}]$  in eq.(3.28) are sampled with walkers generated from the same distribution,  $\Psi[\alpha^{(0)}]$ .

However, the quantity  $\sigma^2$  is a good estimate only, if  $E_{\text{VMC}}$  is accurately determined in eq.(3.28). As this is generally not the case for a small number of walkers, it has been suggested to replace  $E_{\text{VMC}}$  with an appropriately chosen and fixed reference value,  $E_{\text{ref}}$  [LESTER 1994]. But it is generally difficult to know what the best value for  $E_{\text{ref}}$  is, since it is the true energy,  $E_{\text{VMC}}^{\infty}[\alpha^*]$ , for  $\Psi_{\text{T}}^{\text{VMC}}[\alpha^*]$  with optimized parameters,  $\alpha^*$ , and infinitely many sampling points. We will show that the variance minimization additionally includes a total energy minimization when  $E_{\text{ref}} < E_{\text{VMC}}^{\infty}[\alpha^*]$ .

### Interdependence of Variance and Energy Minimization

Following Ref. [LESTER 1994], this interdependence between variance and energy minimization can be seen as follows. When setting  $E_{\text{ref}} := E_{\text{VMC}}^{\infty}[\alpha^*] + \delta E$  for a small value  $\delta E$ , the variance in eq.(3.25) becomes

$$\begin{aligned}\sigma_{\delta E}^2[\alpha] &:= \frac{1}{M} \sum_{i=1}^M (E_{\text{L}}[\alpha] - E_{\text{VMC}}^{\infty}[\alpha^*] - \delta E)^2 \\ &= \sigma^2[\alpha] + \delta E^2 + 2\delta E \cdot (E_{\text{VMC}}^{\infty}[\alpha^*] - E_{\text{VMC}}[\alpha]).\end{aligned}\quad (3.29)$$

The first term in the last equation is the variance,  $\sigma^2$ , that we like to minimize with respect to a set of parameters  $\alpha$ . The second term is a constant which does not influence the minimization. The third term, however, is a linear function of  $E_{\text{VMC}}$  and can be made small by choosing  $\delta E$  as small as possible (i.e. setting  $E_{\text{ref}}$  close to  $E_{\text{VMC}}^{\infty}$ ). As an alternative, this third term can also be used to minimize  $E_{\text{VMC}}[\alpha]$  when choosing  $\delta E$  negative. For such a choice, the third term will always be positive (to show this, we also used the fact that  $E_{\text{VMC}}^{\infty}[\alpha^*] < E_{\text{VMC}}[\alpha]$ ). In turn, minimizing that (positive) difference between  $E_{\text{VMC}}^{\infty}[\alpha^*]$  and  $E_{\text{VMC}}[\alpha]$  is equivalent to minimizing  $E_{\text{VMC}}[\alpha]$ .

To conclude, when choosing  $E_{\text{ref}}$  sufficiently lower than  $E_{\text{VMC}}^{\infty}$  (in our calculations about 1-10 mHa), expression(3.29) is optimized using both, variance and energy minimization. In the following, we will schematically illustrate the operational optimization procedure within a complete VMC calculation.

#### 3.2.5 The VMC Algorithm with Importance Sampling

The required steps within a complete VMC calculation as used in this work are illustrated in the flowchart in Figure 3.3 and are summarized as follows.

1. A HF or CI calculation is performed with the program package GAMESS [SCHMIDT 1993] to obtain the HF or CI molecular orbitals. Thereby, pseudopotentials are used which are described in Section 3.4.

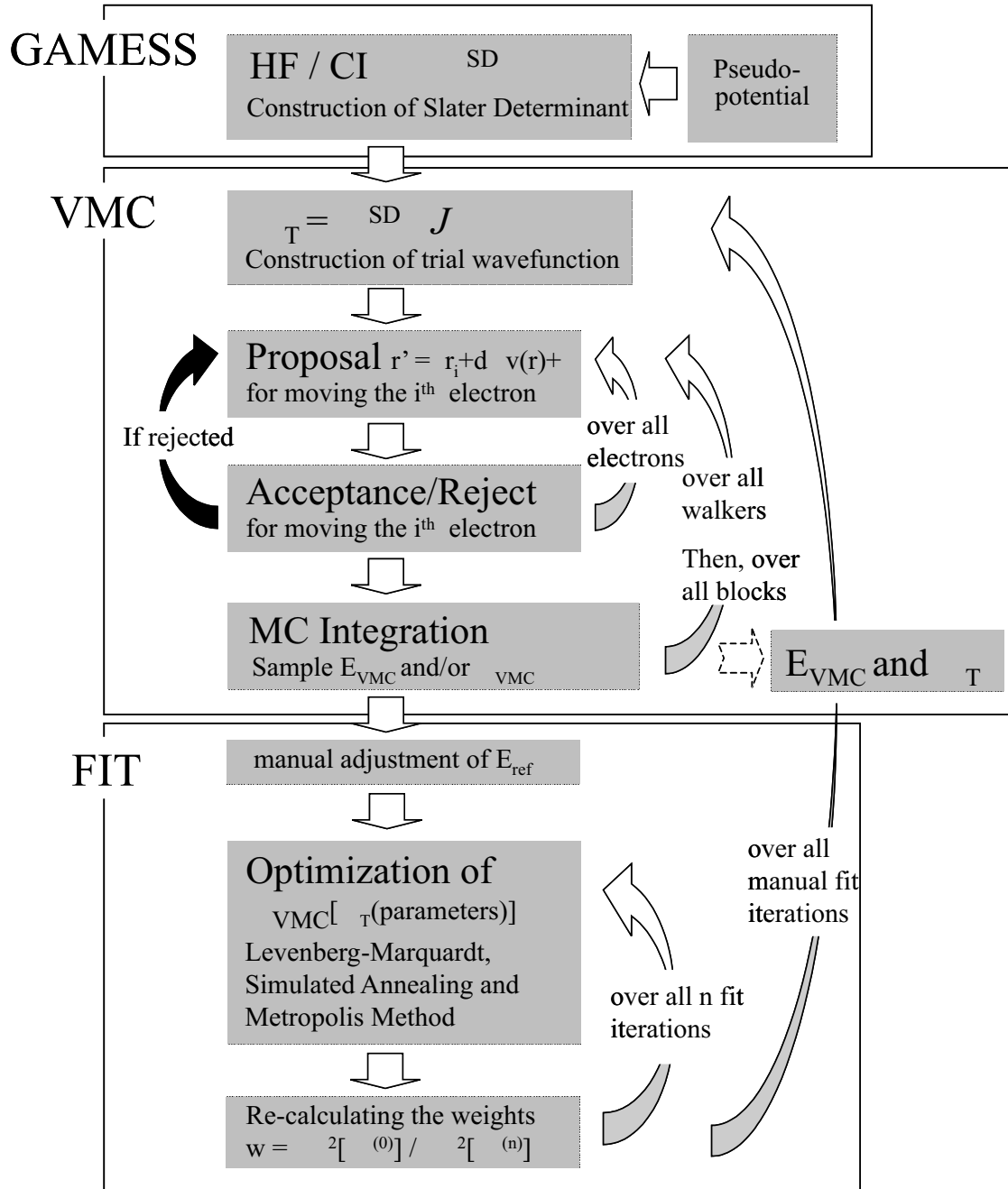


Figure 3.3: This flow-chart illustrates the steps followed when performing a VMC calculation. In total, three different programs are used where each one is framed with a box. All single steps and variables are elaborated in Section 3.2.5.



2. The trial wavefunction is constructed (see Section 3.2.2) by guessing the unknown parameters in the Jastrow factor,  $\alpha^{(0)}$  (usually, by setting all parameters zero).
3. The importance sampled Metropolis algorithm is applied in the following (see also Section 3.1.3). First, one triple of electron coordinates,  $\mathbf{r}_i$ , of a single walker,  $\mathbf{r} = (\mathbf{r}_1, \dots, \mathbf{r}_N)$ , is individually advanced by  $\mathbf{r}'_i = \mathbf{r}_i + \delta\tau \cdot \mathbf{v}_i + \chi_i$ , see also eq.(3.54). Note, only one triple of electron coordinates (rather than the entire walker) is moved to guarantee a small rejection rate.
4. Then, the Metropolis acceptance rule is applied. If that move is accepted, a next electron,  $\mathbf{r}_{i+1}$ , will be moved within the walker,  $\mathbf{r}$ , re-starting from step 3. If the move is rejected, step 3 will be repeated for electron,  $\mathbf{r}_i$ .
5. After the generation of one walker  $\mathbf{r}'$ , the local energy  $E_L(\mathbf{r}')$  will be evaluated.
6. The VMC total energy,  $E_{\text{VMC}}$ , is evaluated based on the average of all previous local energies (at the beginning of only one local energy) according to eq.(3.14). The fluctuation of these local energies gives the variance,  $\sigma^2$ , and is calculated according to eq.(3.28). Now, steps 3 to 6 are repeated until the standard deviation of the mean of  $E_{\text{VMC}}$  defined in eq.(A.10) in the appendix is below a certain value (usually 1 mHa). It is important to notice that subsequently generated walkers are partly correlated since their positions are determined based on their respective predecessors. To guarantee statistically independent local energies when calculating  $E_{\text{VMC}}$  and  $\sigma^2$  (which is required when applying the Central Limit Theorem) a number  $t_{\text{corr}}$  of subsequent walkers are blocked.  $t_{\text{corr}}$  in eq.(A.14) is determined such that the walkers become statistically independent. For a definition of  $t_{\text{corr}}$ , see the auto-correlation function in eq.(A.15). In all later calculations,  $t_{\text{corr}}$  is always less than 10.<sup>5</sup> Also, the first block is omitted when calculating  $E_{\text{VMC}}$  and  $\sigma^2$  since the initial set of walkers might be improperly chosen.
7. After a successful VMC calculation from step 1 to 6 for the initial trial wavefunction,  $\Psi_T$ , its initial parameters are now optimized based on minimizing  $\sigma^2$  (see Section 3.2.4). First,  $E_{\text{ref}}$  needs to be manually adjusted in eq.(3.28) to be lower than the previous  $E_{\text{VMC}}$  value (we choose a value of 1-10mH). When using the first 4000 walkers generated under step 3 for the initial set of parameters,  $\alpha^{(0)}$ , a first set of optimized parameters,  $\alpha^{(1)}$ , will be generated.
8. This optimization procedure will be automatically repeated (iterated) several times (we use 20 iterations) and yields the optimized parameters,  $\alpha^{(20)}$ , for the initially set of walkers.

---

<sup>5</sup> $t_{\text{corr}}$  is defined as the number of time steps  $\delta\tau$  (see Appendix A.14). Since the time is given in units of  $\text{Ha}^{-1}$ , 10 time steps correspond to a time of  $\tau = t_{\text{corr}} \cdot \delta\tau = 1\text{Ha}^{-1}$  for  $t_{\text{corr}} = 10$  and a time step  $\delta\tau = 0.1\text{Ha}^{-1}$ .

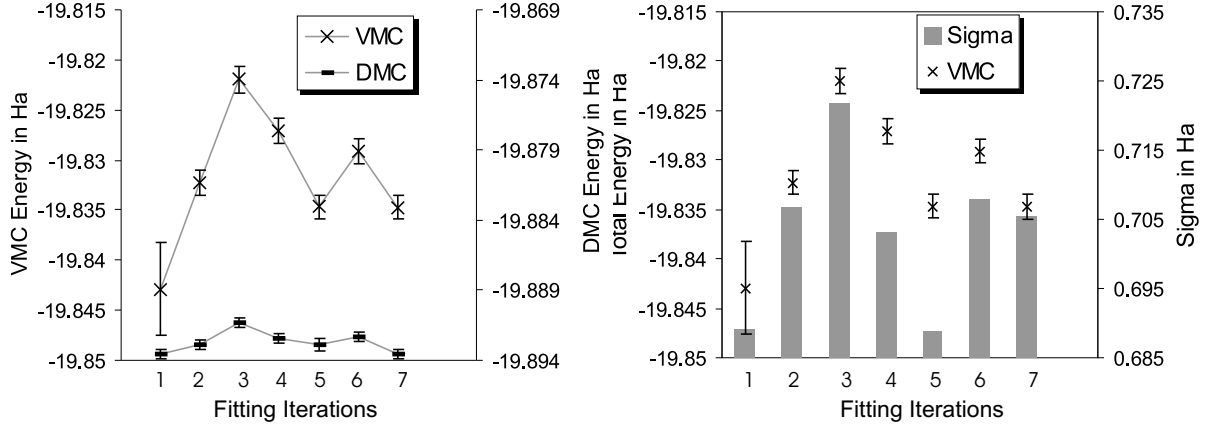


Figure 3.4: The diagram on the left hand side shows the VMC and DMC total energy after each VMC-FIT iteration cycle. The diagram on the right hand side shows the VMC variance for each cycle. For these calculation, the cc-pCVQZ basis and the  $\mathcal{J}(550)$  Jastrow factor is used, where all other specifications are chosen as in Section 4.1. (The DMC total energies are included in the left diagram and will be matter of discussion in Section 3.3.)

9. To check that  $\sigma^2$  has achieved a global minimum for all points in the configuration space, we then generate a new set of walkers from the optimized  $|\Psi_T[\alpha^{(20)}]|^2$  distribution by re-doing step 1 to 6 again. This re-calculation of walkers, followed by another consecutive variance optimization, is performed until the VMC total energy is converged. Figure 3.4 in Appendix A5 presents the results for such an iteration process.

### 3.3 Diffusion Monte Carlo

In this section, we describe the second Monte Carlo method used in this thesis: Diffusion Monte Carlo (DMC). The idea of DMC is to solve the electron Schrödinger equation by mapping it to the classical diffusion and rate equation. Then, these new equations describe the unknown  $N$ -electron ground state,  $\Psi_0$ , when evolving an initial wave function,  $\Psi$ , for a sufficiently long time. Since that evolution projects out the ground state of  $\Psi$ , this method is also referred to as ground state projection technique.

#### 3.3.1 Ground State Projection

To illustrate this projection technique, we start from the time dependent electron Schrödinger equation,

$$i\frac{\partial|\Psi\rangle}{\partial t} = (\hat{T}^e + \hat{V}^e)|\Psi\rangle, \quad (3.30)$$

where  $\hat{T}^e$  and  $\hat{V}^e$  are defined in eq.(2.2) with  $\hat{H}^e = \hat{T}^e + \hat{V}^e$ . Now, we transform  $t$  into imaginary time,  $t \rightarrow it =: \tau$  and introduce a constant offset,  $E_{\text{Ref}}$ ,

$$-\frac{d}{d\tau}|\Psi(\tau)\rangle = (\hat{T}^e + \hat{V}^e - E_{\text{Ref}})|\Psi(\tau)\rangle. \quad (3.31)$$

The need for  $E_{\text{Ref}}$  will be justified shortly. This equation can formally be solved by integration,

$$|\Psi(\tau)\rangle = e^{-(\hat{T}^e + \hat{V}^e - E_{\text{Ref}})\tau} |\Psi(\tau = 0)\rangle. \quad (3.32)$$

Then, the wavefunction  $|\Psi\rangle$  can be expanded in energy eigenvectors,  $|\phi_i\rangle$ ,

$$|\Psi\rangle = \sum_{i=0}^{\infty} c_i |\phi_i\rangle, \quad (3.33)$$

with  $\hat{H}^e |\phi_i\rangle = E_i |\phi_i\rangle$  and coefficients  $c_i$ . Inserting that expansion into eq.(3.32) yields

$$\begin{aligned} |\Psi(\tau)\rangle &= e^{-(\hat{T}^e + \hat{V}^e - E_{\text{Ref}})\tau} \left| \sum_{i=0}^{\infty} c_i \phi_i \right\rangle \\ &= e^{-(E_0 - E_{\text{Ref}})\tau} |c_0 \phi_0\rangle + e^{-(E_1 - E_{\text{Ref}})\tau} |c_1 \phi_1\rangle + \dots \end{aligned} \quad (3.34)$$

When adjusting  $E_{\text{Ref}}$  to be the true ground-state energy,  $E_0$ , the asymptotic solution for large  $\tau$  (large in atomic units) of eq.(3.34) becomes a steady-state solution of the ground state,

$$\lim_{\tau \rightarrow \infty} |\Psi(\tau)\rangle = c_0 |\phi_0\rangle. \quad (3.35)$$

This projection can be understood when remembering that all  $-(E_i - E_{\text{Ref}})$  terms are negative for all excited states with  $i \geq 1$  and zero for the ground state with  $i = 0$ . Consequently, for increasing  $\tau$  all factors in eq.(3.34) decay except the one with  $E_0 = E_{\text{Ref}}$ . For that reason, the imaginary-time evolution operator,  $e^{-(\hat{T}^e + \hat{V}^e - E_{\text{Ref}})\tau}$ , is called **ground state projection operator**<sup>6</sup> and is the basic concept of DMC.

### 3.3.2 Short Time Approximation

The ground state projection for an initially chosen wavefunction can be calculated when writing eq.(3.32) in space representation,

$$\Psi(\mathbf{r}, \tau) = \int \langle \mathbf{r} | e^{-(\hat{T}^e + \hat{V}^e - E_{\text{Ref}})\tau} | \mathbf{r}' \rangle \Psi(\mathbf{r}', 0) d\mathbf{r}' \quad (3.36)$$

$$= \int G(\mathbf{r}, \mathbf{r}', \tau) \Psi(\mathbf{r}', 0) d\mathbf{r}', \quad (3.37)$$

---

<sup>6</sup>The coefficient  $c_0$  in eq.(3.35) is unimportant as it vanishes when normalizing  $|\phi_0\rangle$ .

with  $\langle \mathbf{r} | \Psi \rangle = \Psi(\mathbf{r}, \tau)$  and the Green's function,

$$G(\mathbf{r}, \mathbf{r}', \tau) := \langle \mathbf{r} | e^{-(\hat{T}^e + \hat{V}^e + E_{\text{Ref}})\tau} | \mathbf{r}' \rangle. \quad (3.38)$$

The Green's function can be understood as the probability amplitude of a particle when moving from position  $\mathbf{r}'$  to position  $\mathbf{r}$  in imaginary time. Unfortunately, no analytic solution exists that allows to calculate  $G$  explicitly. However,  $G$  can be evaluated approximately when factorizing the time propagator,  $e^{-(\hat{T}^e + \hat{V}^e - E_{\text{Ref}})\tau}$ , into a separate kinetic and potential energy part,

$$e^{-(\hat{T}^e + \hat{V}^e - E_{\text{Ref}})\tau} = e^{-\frac{1}{2}(\hat{V}^e - E_{\text{Ref}})\tau} e^{-\hat{T}^e \tau} e^{-\frac{1}{2}(\hat{V}^e - E_{\text{Ref}})\tau} + O[\tau^3], \quad (3.39)$$

known as the Trotter approximation [FOULKES 2001]. It is exact only for  $\tau \rightarrow 0$ . When further re-writing  $\tau = n\delta\tau$  with  $n \in \mathbb{N}$ , eq.(3.37) becomes

$$\begin{aligned} \Psi(\mathbf{r}, \tau) &= \int \langle \mathbf{r} | e^{-(\hat{T}^e + \hat{V}^e - E_{\text{Ref}})n\delta\tau} | \mathbf{r}' \rangle \Psi(\mathbf{r}', 0) d\mathbf{r}' \\ &\approx \int \langle \mathbf{r} | (e^{-\frac{1}{2}(\hat{V}^e - E_{\text{Ref}})\delta\tau} e^{-\hat{T}^e \delta\tau} e^{-\frac{1}{2}(\hat{V}^e - E_{\text{Ref}})\delta\tau})^n | \mathbf{r}' \rangle \Psi(\mathbf{r}', 0) d\mathbf{r}' \\ &= \int \langle \mathbf{r} | \dots \left( e^{-(\hat{V}^e - E_{\text{Ref}})\delta\tau} e^{-\hat{T}^e \delta\tau} \right)^{\delta\tau} \left( e^{-(\hat{V}^e - E_{\text{Ref}})\delta\tau} e^{-\hat{T}^e \delta\tau} \right)^{\delta\tau} e^{-\frac{1}{2}(\hat{V}^e - E_{\text{Ref}})\delta\tau} | \mathbf{r}' \rangle \Psi(\mathbf{r}', 0) d\mathbf{r}'. \end{aligned} \quad (3.40)$$

In the last equation, the character of an **iterative projection process** becomes evident: after an initial operation on  $\Psi(\tau = 0)$ , the same kinetic and potential energy operator is  $n$  times iteratively applied acting to the right in the upper equation. Now, in order to find a representation of those iterative operators, we first define two Green's functions,

$$G_{\text{diff}}(\mathbf{r}, \mathbf{r}', \tau) := \langle \mathbf{r} | e^{\hat{T}^e \delta\tau} | \mathbf{r}' \rangle \quad \text{and} \quad G_{\text{rate}}(\mathbf{r}, \mathbf{r}', \tau) := \langle \mathbf{r} | e^{(\hat{V}^e - E_{\text{Ref}})\delta\tau} | \mathbf{r}' \rangle, \quad (3.41)$$

which are spatial representations of the two iterative operators in eq.(3.40). As a matter of fact,  $G_{\text{diff}}$  and  $G_{\text{rate}}$  are at the same time solutions to the classical diffusion and rate equation,

$$-\frac{dG_{\text{diff}}}{d\tau} = \hat{T}G_{\text{diff}} = -\nabla^2 G_{\text{diff}} \quad (3.42)$$

$$\text{and} \quad -\frac{dG_{\text{rate}}}{d\tau} = (\hat{V} - E_{\text{Ref}})G_{\text{rate}}, \quad (3.43)$$

with respective solutions

$$G_{\text{diff}}(\mathbf{r}, \mathbf{r}', \delta\tau) = \frac{1}{(2\pi\delta\tau)^{3N/2}} e^{-\frac{[\mathbf{r} - \mathbf{r}']^2}{2\delta\tau}} \quad (3.44)$$

$$\text{and} \quad G_{\text{rate}}(\mathbf{r}, \mathbf{r}', \delta\tau) = e^{-\delta\tau[\frac{1}{2}V^e(\mathbf{r}) + \frac{1}{2}V^e(\mathbf{r}') - E_{\text{Ref}}]}, \quad (3.45)$$

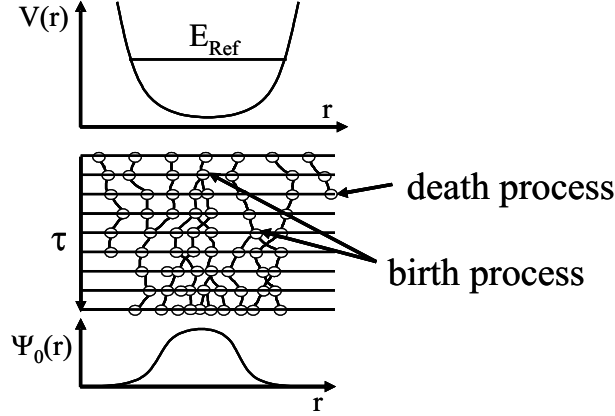


Figure 3.5: This scheme illustrates the iterative branching (birth/death) and diffusion processes as described by the two Green's functions  $G_{\text{rate}}$  and  $G_{\text{diff}}$ . If the potential energy is larger than  $E_{\text{Ref}}$ , random walks are terminated. If the potential energy is less than  $E_{\text{Ref}}$ , multiple copies of the walker may be generated.

following Ref. [FOULKES 2001, LESTER 1994]. With this analogy, the iteration procedure in eq.(3.40) has a simple stochastic interpretation.  $\Psi$  plays the role of the density of diffusing particles if one restricts the previous discussion to problems with positive wavefunctions, i.e. to bosonic systems in their groundstate<sup>7</sup>. The two Green's functions then represent a combined diffusion and rate process acting on those "particles". In particular, when describing  $\Psi$  with a set of "particles", the diffusion process characterized by  $G_{\text{diff}}$  diffuses them according to a Gaussian distribution with the variance  $2\delta\tau$  and zero mean. The subsequent rate process increases or decreases the number of "particles" determined by  $G_{\text{rate}}$ . In particular, for each "particle",  $n$  multiple copies can be created according to the integer part of

$$n = \text{int}[e^{-d\tau[\frac{1}{2}V^e(\mathbf{r}) + \frac{1}{2}V^e(\mathbf{r}') - E_{\text{Ref}}]} + u]. \quad (3.46)$$

In this expression, the first term is the branching probability given in eq.(3.45). The second term,  $u$ , is a uniformly distributed random number in  $[0,1]$ . Since "particles" are created or annihilated, this process is also called branching or birth/death process.

A schematic illustration of these iteration processes is shown in Figure 3.5. In conclusion, when performing these iterative stochastic processes within eq.(3.40), the obtained particle distribution iteratively converges to a discrete representation of the true ground state.

<sup>7</sup>This limitation will be resolved when introducing the fixed node approximation in Section 3.3.5.

### 3.3.3 Importance Sampling in DMC

The above scheme is very inefficient when solving the Schrödinger eq.(3.31). This can be seen as follows. The Coulomb potential,  $V^e(r)$ , increases when two electrons approach each other. Since  $V^e(r)$  influences the branching process described by expression (3.46), changes in  $V^e(r)$  also lead to fluctuations in the number of walkers (particles). However, this fluctuation problem can be largely controlled with the following importance sampling technique.

The idea of this importance sampling technique in DMC is to use a trial (or guiding) wavefunction,  $\Psi_T$ , to help “guiding” random walks towards regions where  $\Psi_T$  is large [KALOS 1974]. This technique is implemented when multiplying the Schrödinger eq.(3.31) with  $\Psi_T$ . When further introducing a new distribution,

$$f(\mathbf{r}, \tau) := \Psi(\mathbf{r}, \tau)\Psi_T(\mathbf{r}, \tau), \quad (3.47)$$

the arising equation

$$\frac{df(\mathbf{r}, \tau)}{d\tau} = \frac{1}{2}\nabla^2 f(\mathbf{r}, \tau) - \nabla[\mathbf{v}(\mathbf{r}, \tau)f(\mathbf{r}, \tau)] - [E_L(\mathbf{r}, \tau) - E_{\text{Ref}}]f(\mathbf{r}, \tau). \quad (3.48)$$

is known as **importance sampled Schrödinger equation**. In that equation, we have introduced the local energy,  $E_L$ , from eq.(3.13) and the drift velocity,

$$\mathbf{v}(\mathbf{r}, \tau) := \frac{\nabla\Psi_T(\mathbf{r}, \tau)}{\Psi_T(\mathbf{r}, \tau)}. \quad (3.49)$$

The importance sampled Schrödinger eq.(3.48) is a modification of eq.(3.31) and has a similar formal solution,

$$f(\mathbf{r}, \tau) = \exp^{-(\hat{T} - \nabla\mathbf{v} + E_L(\mathbf{r}) - E_{\text{Ref}})\tau} f(\mathbf{r}, \tau = 0), \quad (3.50)$$

in accordance to eq.(3.32). Sampling eq.(3.50) for  $f$  has two advantages compared to the previous density  $\Psi$ : (1)  $\hat{V}^e$  becomes replaced by  $E_L$ . Unlike  $\hat{V}^e$ ,  $E_L$  can be controlled by the quality of the trial wavefunction. As a consequence, the fluctuation in the number of walkers (in the population) can be largely reduced. (2) The gradient of the velocity,  $\mathbf{v}$ , accounts for an additional stochastic processes, the drift of a walker, which further improves the sampling process as explained in the following.

When writing eq.(3.50) in integral form and applying the short time approximation again (both steps are in analogy to eq.(3.40)), a third Green’s function arises,

$$G_{\text{drift}}(\mathbf{r}, \mathbf{r}', \delta\tau) := \langle \mathbf{r} | e^{\delta\tau \cdot \nabla \mathbf{v}} | \mathbf{r}' \rangle, \quad (3.51)$$

in addition to those in eq.(3.41). When using the product rule,  $\nabla \cdot \mathbf{v} = \mathbf{v} \cdot \nabla + (\mathbf{v} \cdot \nabla)$ , and considering the fact that  $\mathbf{v}$  is constant (which is true as  $\delta\tau \rightarrow 0$ ), we can substitute

$\nabla \mathbf{v}$  by  $\mathbf{v} \nabla$  in eq.(3.51). When further using the Taylor expansion for a scalar function,  $f$ ,

$$e^{(\delta\tau \cdot \mathbf{v}) \nabla} f(\mathbf{r}) = f[\mathbf{r} + (\delta\tau \cdot \mathbf{v})] \quad (3.52)$$

[NOLTING 1996],  $G_{\text{drift}}$  can be understood as a displacement of  $\mathbf{r}$  by  $\delta\tau \cdot \mathbf{v}$  which can be expressed in the following delta function,

$$G_{\text{drift}} = \langle \mathbf{r} | \mathbf{r}' + \delta\tau \cdot \mathbf{v} \rangle = \delta[\mathbf{r} - (\mathbf{r}' + \delta\tau \cdot \mathbf{v})]. \quad (3.53)$$

Now, the application of this Green's function when describing the additional drift process in eq.(3.48) is equivalent to a **revised proposition rule** in the Metropolis algorithm in Section 3.1.3,

$$\mathbf{r}' = \mathbf{r} + \delta\tau \cdot \mathbf{v}(\mathbf{r}) + \chi. \quad (3.54)$$

In this expression, the walker,  $\mathbf{r}$ , is drifted by the distance  $\delta\tau \cdot \mathbf{v}$  and  $\chi$  is again the normally distributed random vector with variance  $2\delta\tau$  and zero mean. When recalling the definition of the drift velocity,  $\mathbf{v}$ , in eq.(3.49), it can be immediately seen that  $\mathbf{v}$  drifts walkers into regions of large  $\Psi_T$ . In particular, the velocity becomes large when walkers approach a nodal surface, i.e. when  $\Psi_T$  becomes small (recall that  $\mathbf{v}$  is singular for  $\Psi_T = 0$ ). And the velocity is small if walkers approach a maximum in  $\Psi_T$ . To conclude, the solution of the importance sampled Schrödinger eq.(3.50) is now obtained by an iteration of three statistical processes: diffusion, branching (modified by the local energy) and drifting.

### 3.3.4 Total Energy in DMC

In the last sections, we have discussed the finding of the exact ground state for the time-dependent Schrödinger equation. In this section, we will show that the DMC algorithm in principle yields the true ground state energy. Different approaches exist to obtain the total energy in DMC [UMRIGAR et al. 1993]. In this work, we will use the method of a **mixed estimator** which calculates the total energy as an average of local energies similarly as in VMC.

To verify that, let us consider the mixed estimator,  $\langle \Psi_0 | \hat{H}^e | \Psi_T \rangle$ , as the expectation value of  $\hat{H}^e$  using the exact wavefunction,  $\Psi_0$  (on the left), and the trial wavefunction,  $\Psi_T$  (on the right). Via the hermiticity,  $\hat{H}^e$  can also be applied to the left on  $\Psi_0$ , which yields

$$\frac{\langle \Psi_0 | \hat{H}^e | \Psi_T \rangle}{\langle \Psi_0 | \Psi_T \rangle} = \frac{\langle \Psi_0 | E_0 | \Psi_T \rangle}{\langle \Psi_0 | \Psi_T \rangle} = E_0 \frac{\langle \Psi_0 | \Psi_T \rangle}{\langle \Psi_0 | \Psi_T \rangle} = E_0. \quad (3.55)$$

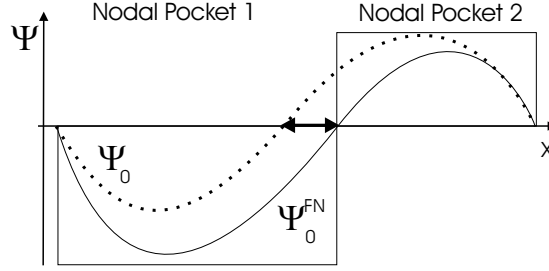


Figure 3.6: This schematic illustration shows the difference between the fixed-node DMC ground state wavefunction,  $\Psi_0^{FN}$ , and the exact wavefunction,  $\Psi_0$ . The black arrow indicates the displacement between the fixed nodal surface (which is 0-dimensional in this illustration) and the true nodal surface.

In this expression, the mixed estimator is normalized. Furthermore, that mixed estimator can also be written in integral form,

$$\frac{\int \Psi_0(\mathbf{r}) \hat{H}^e \Psi_T(\mathbf{r}) d\mathbf{r}}{\int \Psi_0(\mathbf{r}) \Psi_T(\mathbf{r}) d\mathbf{r}} = \frac{\int \Psi_0(\mathbf{r}) \frac{\Psi_T(\mathbf{r})}{\Psi_T(\mathbf{r})} \hat{H}^e \Psi_T(\mathbf{r}) d\mathbf{r}}{\int \Psi_0(\mathbf{r}) \Psi_T(\mathbf{r}) d\mathbf{r}} = \frac{\int f_\infty(\mathbf{r}) E_L(\mathbf{r}) d\mathbf{r}}{\int f_\infty(\mathbf{r}) d\mathbf{r}}. \quad (3.56)$$

In the last step, we inserted the local energy from eq.(3.13) and the converged probability distribution  $f_\infty = \Psi_0 \Psi_T$  from eq.(3.47). Using importance sampled MCI in eq.(3.56), the equality of the last two equations yields

$$E_0 = E_{\text{DMC}} \quad \text{with} \quad E_{\text{DMC}} := \frac{1}{M} \sum_{i=1}^M E_L(\mathbf{r}_i). \quad (3.57)$$

The last expression is the obtained estimate of the DMC total energy.  $E_{\text{DMC}}$  then is the exact ground state energy if the distribution  $f_\infty$  is converged to  $\Psi_0 \Psi_T$ , where  $\Psi_0$  is the true ground state and  $\Psi_T$  the chosen trial wavefunction.

### 3.3.5 The Fixed Node Approximation in DMC

So far we have assumed that the wavefunction,  $\Psi$ , is positive everywhere. When dealing with fermion systems, however, the requirement of anti-symmetry also calls for negative values of  $\Psi$ . But unfortunately, probabilistic methods such as DMC can handle only positive probability distributions. There have been attempts to impose sign variables to individual walkers [Anderson 1975], but so far, their applications (except for very simple ones like  $\text{H}_3^+$ ) have not been successful due to large signal-to-noise ratio [FOULKES 2001]. An alternative method, which is now the common way to deal with this sign problem and implemented in our code, is the fixed-node approximation. In this approximation, an initially calculated trial wavefunction,  $\Psi_T$ ,



for  $N$  electrons divides the configuration space into pockets that are separated by  $(3N - 1)$ -dimensional nodal surfaces on which  $\Psi_T$  is zero. All walkers in one pocket are now assigned the same sign, and the fixed-node DMC algorithm projects out the fixed-node ground state,  $\Psi_0^{\text{FN}}$ . Thereby, the nodal surface of  $\Psi_T$  is kept as boundary condition. For illustration, see Figure 3.6.

The implementation of the fixed-node approximation is a slight modification of the normal DMC algorithm: a walker will be deleted if it crosses a nodal surface. But the used importance sampling DMC algorithm drifts the walkers already away from the nodal surfaces as explained in Section 3.3.3. Hence, the number of walkers crossing the nodal surface is already reduced.

It can be shown that the fixed-node DMC energy,  $E_0^{\text{FN}}$ , is variational,

$$E_0^{\text{FN}} = \langle \Psi_0^{\text{FN}} | H^e | \Psi_0^{\text{FN}} \rangle \geq E_0, \quad (3.58)$$

and is an upper bound to the exact ground state energy [LESTER 1994]. In Ref. [FOULKES 2001], the fixed node error of the total energy is estimated to be not larger than 5% of the correlation energy. This estimation assumes a decent trial wavefunction with a Slater determinant obtained by a HF calculation.

The fixed-node error can systematically be reduced when improving the nodal surface. This can be done for example when using more than one determinant in  $\Psi_T$ . But since the fixed-node error is always positive, it partly cancels when calculating energy differences.

### 3.3.6 DMC Algorithm with Importance Sampling

The required steps within a complete DMC calculation are illustrated in Figure 3.7 and are summarized in the following.

1. The optimized trial wavefunction,  $\Psi_T$ , from a previous VMC calculation is chosen as initial wavefunction in DMC. For the molecules studied here, we will use a population of  $P = 50$  (the number of simultaneous walkers) which is the zeroth generation of diffusion steps.<sup>8</sup>
2. In step 2 to 4, the next generation of walkers will be generated using the importance sampled Metropolis algorithm (see Section 3.1.3): in particular, a triple of electron coordinates,  $\mathbf{r}_i$ , of a single walker,  $\mathbf{r} = (\mathbf{r}_1, \dots, \mathbf{r}_N)$ , is advanced by  $\mathbf{r}'_i = \mathbf{r}_i + \chi_i + \delta\tau \cdot \mathbf{v}(\mathbf{r})$ . The time step,  $\delta\tau$ , is chosen as to minimize the time step error discussed in eq.(3.39). At the same time, the auto-correlation time (see also step 8) increases for smaller time steps and thereby the numerical effort. Consequently, a compromise has to be made when setting the time step (details are discussed in Section 5.5).

---

<sup>8</sup>The population needs to be larger than one walker, since their number will fluctuate in later branching processes.

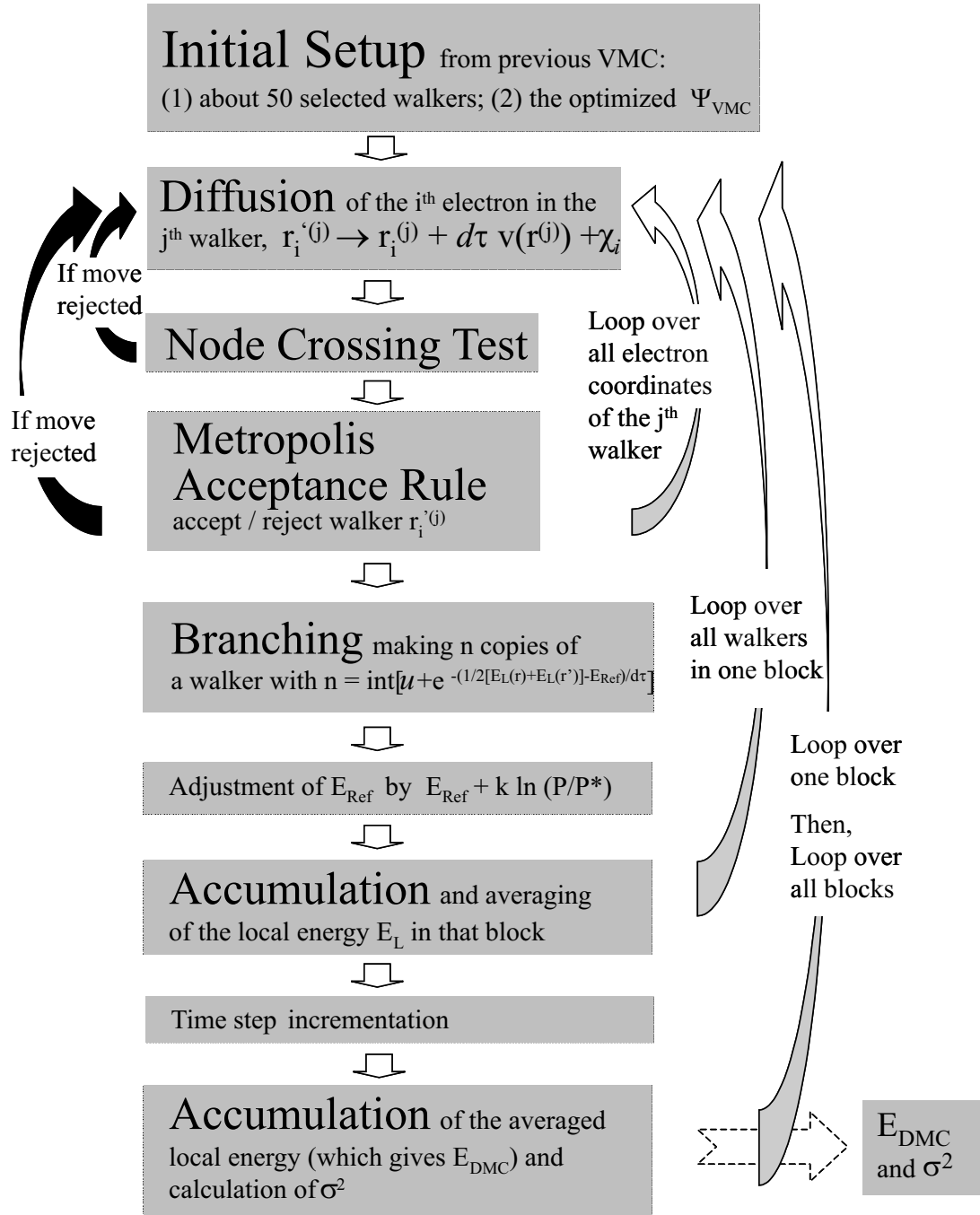


Figure 3.7: This flow-chart illustrates the steps followed when performing a DMC calculation. All single steps and variables are elaborated in Section 3.3.6.

3. To account for the fixed-node approximation, our algorithm checks now whether the proposed walker (with the new triple of electron coordinates) has crossed a nodal surface. In this case, the proposed move will be rejected and the algorithm resumes at step 2 again.
4. If the walker does not cross a nodal surface, it is then accepted with probability  $P(\mathbf{r} \rightarrow \mathbf{r}')$  given in eq.(3.10). In case of rejection, the algorithm resumes step 2 again, likewise. Normally, an acceptance ratio is obtained which is larger than 90%. In case of acceptance, steps 2 to 4 are iterated for the next electron,  $\mathbf{r}_{i+1}$ , in that walker,  $\mathbf{r}$ .
5. After a successful diffusion and drift of one walker in steps 2 to 4, the walker either branches into  $n$  copies or is eliminated according to the integer expression,

$$n = \text{int}[\exp^{-\delta\tau(\frac{1}{2}E_L(\mathbf{r}) + \frac{1}{2}E_L(\mathbf{r}') - E_{\text{Ref}})} + u]. \quad (3.59)$$

The first term in the above expression is the branching probability according to eq.(3.45), where  $\hat{V}^e(r)$  is replaced by  $E_L$  (discussed in Section 3.3.3). The second term,  $u$ , is a uniformly distributed random number in  $[0,1]$ . Similarly as in Figure 3.5, the upper expression describes a branching process that eliminates a walker if the local energy,  $E_L$ , is larger than  $E_{\text{Ref}}$  and generates copies if the local energy is less than  $E_{\text{Ref}}$ .

6. Steps 2 to 5 are iterated for all walkers in one generation.
7. The number of walkers in one generation fluctuates and might have changed from its initial value due to the branching process. However, when adjusting the trial energy,  $E_{\text{Ref}}$ , in eq.(3.45), the population,  $P$  (the number of walkers in one generation), can be kept at a desired level. This is done by adjusting  $E_{\text{Ref}}$  according to

$$E_{\text{Ref}} = E_{\text{guess}} + \kappa \ln\left(\frac{P}{P^*}\right), \quad (3.60)$$

where  $P$  is the current and  $P^*$  the initial (desired) population.  $E_{\text{guess}}$  is the best guess of the ground state energy. Initially, it needs to be adjusted manually (e.g.  $E_{\text{guess}}(\tau = 0) = E^{\text{VMC}}$ ). Later on, it is replaced by  $E_{\text{DMC}}$ .  $\kappa$  is a feedback parameter and is adjusted such as to stabilize the population around the initial  $P^*$ .

8. The DMC total energy,  $E_{\text{DMC}}$ , is obtained as average value of the local energy, see eq.(3.57).
9. In order to guarantee statistically independent local energies when calculating  $E_{\text{DMC}}$ , a certain number of diffusion steps are blocked before calculating  $E_{\text{DMC}}$ . Likewise as in the VMC algorithm (i.e. step 6, not repeated here), step 2 to 7 are iterated for a certain fixed number of generations which are grouped in one

block. The block length is determined by the correlation time,  $t_{\text{corr}}$  [see eq.(A.14 in Appendix A)], and is usually less than 5. The correlation time in DMC is also discussed in Section 5.5.

10. The cycle 2 to 9 will be redone for as many blocks as are required to project out all excited states (for our molecules, we use between 2000 and 8000 blocks).

## 3.4 Pseudopotentials in QMC

In this section, pseudopotentials in VMC and DMC will be discussed, since their application introduces approximations that might influence our results. After a short introduction, the construction of our used pseudopotentials is presented, followed by their application in VMC and subsequently in DMC.

As already stated in the introduction of this thesis, all-electron QMC calculations have been applied to first row molecules in few studies. But already for first row molecules, these studies reflect the difficulty in the all-electron treatment by DMC calculations. In addition, we already stated the numerical effort which severely increases with the nuclear charge. Two main problems occur when dealing with core electrons in larger atoms. (1) There is an increase of the fluctuations in the local energy,  $E_L$ , since the potential and kinetic energies are large in the core region. Because of a rapidly changing wavefunction in the core region, it is very difficult to design such a trial wavefunction that can decrease these fluctuations in  $E_L$ . (2) Due to an increased variation in the wave function near a nucleus of large  $Z$ , the time steps need to be small enough to reduce the rejection rate of the walkers. However, small time steps drastically reduce the efficiency of DMC since the correlation time increases. The two stated main problems are overcome with the pseudopotential approximation.

The pseudopotential approximation in QMC considers the core orbitals of atoms and molecules as frozen. Then, the effects by those fixed orbitals are replaced by an angular momentum dependent potential. A justification for that approximation is that the core remains practically inert and has a negligible impact on the valence properties, like chemical bonds. As an additional step, the valence orbitals are then replaced by pseudo-orbitals. The pseudopotential is constructed such as to approximate the core-valence interaction. Since we will use pseudopotentials obtained from a HF calculation, it should be said that core-valence Coulomb interaction is not incorporated in our pseudopotentials.

While pseudopotentials account for further approximations (first introduced to QMC by [BACHELET 1989]), they drastically increase the efficiency of QMC algorithms. An estimate of the scaling in DMC is given by  $N^3$ , where  $N$  is the number of valence electrons [MITAS 1991]. The large improvement in the exponent from 5.5-6.5 to 3 can be understood by the removal of the core orbitals and thereby the two main problems indicated in the first paragraph.

### 3.4.1 The Construction of Pseudopotentials

The pseudopotentials used in our calculations are constructed from an all-electron HF calculation of the free atom in spherical approximation. With the following ansatz for the one-particle orbitals,  $\phi_{nlm} = \rho_{nl} Y_{lm}$  (where  $\rho_{nl}$  is the radial part and  $Y_{lm}$  are the spherical harmonics), the HF equation from Section 2.3 can be separated in a radial HF equation,

$$\left[ -\frac{1}{2} \nabla_r^2 + \frac{l(l+1)}{2r^2} - \frac{Z}{r} + \hat{v}_{\text{loc}}^{\text{H}}(r) + \hat{v}^{\text{X}}(r)_{\text{nloc}l} \right] \rho_{nl}(r) = \varepsilon_{nl} \rho_{nl}(r). \quad (3.61)$$

$n$  is the principal quantum number,  $l$  the angular momentum and  $m$  the magnetic quantum number.  $r$  is the radius of the position of the  $i^{\text{th}}$  electron,  $\mathbf{r}_i$  (the index  $i$  is omitted for the radius) and  $Z$  is the nuclear charge.  $\hat{v}_{\text{loc}}^{\text{H}}$  is the local Coulomb potential (Hartree potential) and  $\hat{v}_{\text{nloc}l}^{\text{X}}$  the non-local Fock operator (exchange operator) which depends on  $l$ . Notice that both operators,  $\hat{v}_{\text{loc}}^{\text{H}}$  and  $\hat{v}_{\text{nloc}l}^{\text{X}}$ , only describe the radial part of the Coulomb potential and Fock operator given in eq.(2.13) and (2.14), respectively.<sup>9</sup>

After solving eq.(3.61) self-consistently for all electrons with numerical HF [JENSEN 2002], the core electrons are then eliminated and pseudo-orbitals,  $\phi_{nlm}^{\text{psp}} = \rho_{nl}^{\text{psp}} Y_{lm}$ , are constructed. This construction is done by choosing a cutoff radius,  $r_0$ , and eliminating all nodes for  $r \leq r_0$ . For the pseudo-orbitals, it is required that they should reproduce the behavior of the all-electron orbitals outside the cutoff radius for  $r \geq r_0$ . Also, the continuity of the trial wavefunction at the cutoff radius,  $r_0$ , and the normalization need to be satisfied.

Following Ref. [LESTER 1994], the pseudo-HF equation then becomes

$$\left[ -\frac{1}{2} \nabla_r^2 + \frac{l(l+1)}{2r^2} - \frac{Z_{\text{eff}}}{r} + \hat{v}_{\text{loc}}^{\text{H val}}(r) + \hat{v}_{\text{nloc}l}^{\text{X val}} + \hat{v}_{\text{loc}l}^{\text{psp}}(r) \right] \rho_{nl}^{\text{psp}}(r) = \varepsilon_{nl} \rho_{nl}^{\text{psp}}(r). \quad (3.62)$$

Here,  $\hat{v}_{\text{loc}l}^{\text{psp}}$  is the pseudopotential operator accounting for the core-valence interaction. And  $\hat{v}_{\text{loc}}^{\text{H val}}$  and  $\hat{v}_{\text{nloc}l}^{\text{X val}}$  are the Coulomb and Fock operators acting on the pseudo-orbitals.  $Z_{\text{eff}}$  is the effective charge and  $\varepsilon_{nl}$  are the all-electron eigenvalues for the valence orbitals from eq.(3.61). The pseudopotential can be obtained by inverting the pseudo-HF eq.(3.62),

$$\hat{v}_{\text{loc}l}^{\text{psp}}(r) = \varepsilon_{nl} + \frac{Z_{\text{eff}}}{r} - \frac{l(l+1)}{2r^2} + \frac{\frac{1}{2} \nabla_r^2 \rho_{nl}^{\text{psp}}(r)}{\rho_{nl}^{\text{psp}}(r)} - \left( \hat{v}_{\text{loc}}^{\text{H val}}(r) + \frac{(\hat{v}_{\text{nloc}l}^{\text{X val}} \rho_{nl}^{\text{psp}})(r)}{\rho_{nl}^{\text{psp}}(r)} \right) \quad (3.63)$$

It should be noticed that the constructed pseudo-orbitals and therefore the pseudopotential in the previous expression exist only numerically (i.e. are constructed on a grid). Therefore, to obtain an analytic expression, the analytic function,

<sup>9</sup>An explicit expression radial expression for both terms is omitted here. A derivation of these terms can be found e.g. in Ref. [WAHN 2002].

$$\hat{v}_{\text{loc}l}^{\text{psp}}(r) = \frac{1}{r^2} \sum_{k=0}^{k_{\text{max}}} A_{lk} r^{n_{lk}} e^{B_{lk} r^2}, \quad (3.64)$$

is fitted on the numerical expression (3.63). Thereby, each of the  $l$  pseudopotential components is fitted individually with  $A_{lk}$ ,  $n_{lk}$  and  $B_{lk}$  being the fitting parameters.

So far, we considered the HF equation for the radial part of one-particle orbitals. Thereby, the pseudopotential was local for any fixed  $l$ . Now, we generalize the concept of pseudopotentials to the entire atomic orbital. This generalization is important when treating systems beyond single atoms but also to understand the application of pseudopotentials to many-electron wavefunctions in VMC and DMC, later on.

Typically, norm-conserving pseudopotentials are set up and derived in terms of an angular momentum dependent non-local operator<sup>10</sup>,  $\hat{v}_{\text{nloc}}^{\text{psp}}$ , as found in

$$\langle \mathbf{r}_i | \hat{v}_{\text{nloc}}^{\text{psp}} | \mathbf{r}'_i \rangle = \frac{\delta(r - r')}{r^2} \sum_l \sum_{m=-l}^l \langle \Omega | lm \rangle \hat{v}_{\text{loc}l}^{\text{psp}}(r) \langle lm | \Omega' \rangle. \quad (3.65)$$

Here,  $\langle \Omega | lm \rangle = Y_{lm}(\Omega)$  are the spherical harmonics, and  $\Omega$  are the spherical coordinates.  $\hat{v}_{\text{loc}l}^{\text{psp}}$  are the pseudopotential operators from eq.(3.64) that are local in the radial coordinate for a fixed quantum number,  $l$ . However, it is important to notice that  $\hat{v}_{\text{nloc}}^{\text{psp}}$  is non-local due to its dependence on  $l$ .

The expression for  $\hat{v}_{\text{nloc}}^{\text{psp}}$  can be simplified as follows. The repulsive part  $l(l+1)/2r^2$  of the potential in eq.(3.62) pushes an electron outward with increasing angular momentum. Also, all components  $\hat{v}_{\text{loc}l}^{\text{psp}}$  at large  $r$  reduce to the effective Coulomb potential,  $-Z^{\text{eff}}/r$ , independently of  $l$ . Hence,  $\hat{v}_{\text{nloc}}^{\text{psp}}$  can be approximated by a multiplicative local potential,  $\hat{v}_{\text{loc}l_{\text{max}}+1}^{\text{psp}}$ , plus a few  $l$ -dependent “short-range corrections” for  $l \leq l_{\text{max}}$  (where  $l_{\text{max}}$  is appropriately chosen),

$$\langle \mathbf{r}_i | \hat{v}_{\text{nloc}}^{\text{psp}} | \mathbf{r}'_i \rangle \approx \delta(r - r') \hat{v}_{\text{loc}l_{\text{max}}+1}^{\text{psp}}(r) + \Delta \hat{v}_{\text{nloc}}^{\text{psp}}(\mathbf{r}_i, \mathbf{r}'_i), \quad (3.66)$$

$$\text{with} \quad \Delta \hat{v}_{\text{nloc}}^{\text{psp}}(\mathbf{r}_i, \mathbf{r}'_i) := \sum_{l=0}^{l_{\text{max}}} \frac{\delta(r - r')}{r^2} \Delta \hat{v}_{\text{loc}l}^{\text{psp}}(r) \sum_{m=-l}^l Y_{lm}^*(\Omega) Y_{lm}(\Omega') \quad (3.67)$$

$$\text{and} \quad \Delta \hat{v}_{\text{loc}l}(r) := \hat{v}_{\text{loc}l}^{\text{psp}}(r) - \hat{v}_{\text{loc}l_{\text{max}}+1}^{\text{psp}}(r). \quad (3.68)$$

$\Delta \hat{v}_{\text{nloc}}^{\text{psp}}$  is defined to be the non-local pseudopotential from which the local component,  $\hat{v}_{\text{loc}l_{\text{max}}+1}^{\text{psp}}(r)$ , is subtracted. Eq.(3.66) to (3.68) are now a truncated expression for the non-local pseudopotential.

---

<sup>10</sup>See for example the reference M. Fuchs, M. Scheffler Computer Physics Communications 119 67-98 (1999).

For the nitrogen atom, Figure 5.2 presents the two pseudopotential components,  $\hat{v}_{loc}^{psp}$  (local) and  $\Delta\hat{v}_{loc}^{psp} = \hat{v}_{loc}^{psp} - \hat{v}_{loc}^{psp}$  (called non-local component) for three pseudopotentials used in this work. The first is generated by Claudia Filippi following the described procedure above [Filippi, private communication] and is optimized to describe the atom. The respective coefficients are listed Appendix B. The second pseudopotential is the Stevens-Basch-Kraus (SBK) one and is taken from Ref. [STEVENS 1984]. For this SBK pseudopotential, a different approach was chosen to obtain the analytic expression (3.64) for its pseudopotential components. In particular, expression (3.64) was inserted into the pseudo-HF equations as an ansatz, while all parameters in that expression were optimized to approximate the eigenvalues  $\epsilon_{ln}$ . The third pseudopotential, called MF in this thesis, was taken from Ref. [LESTER 2001, GREEFF 1998] and was constructed similarly to the SBK pseudopotential.

### 3.4.2 Pseudopotentials in VMC

So far, the treatment of pseudopotentials was done in an independent particle picture, in particular by HF (DFT would be possible, too). Now, we are interested in constructing a many-electron pseudopotential for  $N$  electrons with coordinates  $\mathbf{r} = \mathbf{r}_1, \dots, \mathbf{r}_N$ , and in applying it to the many electron trial wavefunction,  $\Psi_T$ . We are then also able to construct the new Hamiltonian for pseudo-orbitals and to evaluate its local energy,  $E_L = \hat{H}^{psp} \Psi_T / \Psi_T$ .

Following Ref. [FAHY 1990], the many-electron pseudopotential acts as an effective one-body operator. This allows us to write the many-electron pseudopotential,  $\hat{V}_{nloc}^{psp}$ , as a sum of one-particle operators,

$$\hat{V}_{nloc}^{psp} := \sum_{i=1}^N \hat{V}_{nloc\,i}^{psp}. \quad (3.69)$$

The one-particle operator,  $\hat{V}_{nloc\,i}^{psp}$ , only acts on the  $i^{th}$  electron, while all other electron coordinates are kept fixed. In a formal quantum mechanical notation, this can be written as

$$\hat{V}_{nloc\,i}^{psp} := \hat{1}_1 \otimes \hat{1}_2 \cdots \otimes \hat{v}_{nloc\,i}^{psp} \cdots \otimes \hat{1}_N. \quad (3.70)$$

Here,  $\hat{v}_{nloc\,i}^{psp}$  is the non-local one-particle operator from eq.(3.66) and  $\hat{1}_j$  is the unity operator with  $j = 1, \dots, i-1, i+1, \dots, N$ .

Now, we want to apply  $\hat{V}_{nloc}^{psp}$  on  $\Psi_T$ ,

$$\langle \mathbf{r} | \hat{V}_{nloc}^{psp} | \Psi_T \rangle = \int \langle \mathbf{r} | \hat{V}_{nloc}^{psp} | \mathbf{r}' \rangle \langle \mathbf{r}' | \Psi_T \rangle d\mathbf{r}', \quad (3.71)$$

where the unity-operator,  $\int |\mathbf{r}' \rangle \langle \mathbf{r}'| d\mathbf{r}'$ , is inserted. When expanding  $\hat{V}_{nloc}^{psp}$  as in

eq.(3.69) and use the notation  $|\mathbf{r}\rangle = |\mathbf{r}_1\rangle|\mathbf{r}_2\rangle\cdots|\mathbf{r}_N\rangle$ , we can write eq.(3.71) as

$$\begin{aligned} \langle \mathbf{r} | \sum_{i=1}^N \hat{V}_{\text{nloc } i}^{\text{psp}} | \Psi_T \rangle &= \int_{\mathbb{R}^3} \langle \mathbf{r} | \sum_{i=1}^N \hat{V}_{\text{nloc } i}^{\text{psp}} | \mathbf{r}' \rangle \langle \mathbf{r}' | \Psi_T \rangle d^3 \mathbf{r}_i \\ &= \sum_{i=1}^N \int_{\mathbb{R}^3} \langle \mathbf{r}_i | \hat{v}_{\text{nloc } i}^{\text{psp}} | \mathbf{r}'_i \rangle \langle \mathbf{r}' | \Psi_T \rangle d^3 \mathbf{r}_i. \end{aligned} \quad (3.72)$$

In the last step, we have used that  $\hat{V}_{\text{nloc } i}^{\text{psp}}$  only acts on the  $i^{\text{th}}$  electron coordinates and becomes the single-particle operator  $\hat{v}_{\text{nloc } i}^{\text{psp}}$  according to eq.(3.70). Since  $\hat{v}_{\text{nloc } i}^{\text{psp}}$  is known from eq.(3.66), we can finally write the action of the many-electron pseudopotential on  $\Psi_T$  as,

$$(\hat{V}_{\text{nloc}}^{\text{psp}} \Psi_T)(\mathbf{r}) = \sum_{i=1}^N \int_{\mathbb{R}^3} (\delta(r_i - r'_i) \hat{v}_{\text{loc } l_{\text{max}}+1}^{\text{psp}}(r_i) + \Delta \hat{v}_{\text{nloc}}^{\text{psp}}(\mathbf{r}_i, \mathbf{r}'_i)) \Psi_T(\mathbf{r}'_1, \dots, \mathbf{r}'_i, \dots, \mathbf{r}'_N) d^3 \mathbf{r}'_i, \quad (3.73)$$

where  $\Delta \hat{v}_{\text{nloc}}^{\text{psp}}(\mathbf{r}_i, \mathbf{r}'_i)$  is given in eq.(3.67). For further convenience, let us divide the last expression into a local and a non-local many-electron pseudopotential operator,  $\hat{V}_{\text{nloc}}^{\text{psp}} = \hat{V}_{\text{loc } l_{\text{max}}+1}^{\text{psp}} + \Delta \hat{V}_{\text{nloc}}^{\text{psp}}$ , defined as

$$\hat{V}_{\text{loc } l_{\text{max}}+1}^{\text{psp}} \Psi_T(\mathbf{r}) := \sum_{i=1}^N \hat{v}_{\text{loc } l_{\text{max}}+1}^{\text{psp}}(r_i) \Psi_T(\mathbf{r}'_1, \dots, \mathbf{r}'_i, \dots, \mathbf{r}'_N) \quad (3.74)$$

$$\text{and } (\Delta \hat{V}_{\text{nloc}}^{\text{psp}} \Psi_T)(\mathbf{r}) := \sum_{i=1}^N \int_{\mathbb{R}^3} \Delta \hat{v}_{\text{nloc}}^{\text{psp}}(\mathbf{r}_i, \mathbf{r}'_i) \Psi_T(\mathbf{r}'_1, \dots, \mathbf{r}'_i, \dots, \mathbf{r}'_N) d^3 \mathbf{r}'_i. \quad (3.75)$$

Following now Ref. [MITAS 1991], we will write the new Hamiltonian from eq.(2.4) as a sum of a local part,  $\hat{H}_{\text{loc}}^{\text{e psp}}$  (which includes  $\hat{V}_{\text{loc } l_{\text{max}}+1}^{\text{psp}}$ ), and the non-local part,  $\Delta \hat{V}_{\text{nloc}}^{\text{psp}}$ ,

$$\hat{H}^{\text{e psp}} = \hat{H}_{\text{loc}}^{\text{e psp}} + \Delta \hat{V}_{\text{nloc}}^{\text{psp}}. \quad (3.76)$$

The contribution of  $\hat{H}_{\text{loc}}^{\text{e psp}}$  to the local energy is obtained as discussed in Section 3.2. The second contribution by  $\Delta \hat{V}_{\text{nloc}}^{\text{psp}}$  to the local energy is given by expression

$$\frac{(\Delta \hat{V}_{\text{nloc}}^{\text{psp}} \Psi_T)(\mathbf{r})}{\Psi_T(\mathbf{r})} = \sum_{i=1}^N \frac{\sum_{l=0}^{l_{\text{max}}} \Delta \hat{v}_{\text{loc } l}^{\text{psp}}(r_i) \sum_{m=-l}^l Y_{lm}(\Omega_i) \int_{\Omega_i} Y_{lm}^*(\Omega'_i) \Psi_T(\mathbf{r}_1, \dots, \mathbf{r}'_i, \dots, \mathbf{r}_N) d\Omega'_i}{\Psi_T(\mathbf{r}_1, \dots, \mathbf{r}_i, \dots, \mathbf{r}_N)}. \quad (3.77)$$

It describes the action of the non-local part of the pseudopotential onto the many-electron trial wavefunction. To obtain the last equation, we substituted the expression



for  $\Delta\hat{v}_{\text{nloc}}^{\text{psp}}(\mathbf{r}_i, \mathbf{r}'_i)$  from eq.(3.67) into eq.(3.75). Then we integrated over the delta functions of the radial coordinates,  $r_i$ , of all electrons. To finally evaluate eq.(3.77), only 2-dimensional surface integrals over the angular coordinates,  $\Omega'_i$ , for each electron remain to be solved. To do so, our VMC code provides three technical choices of numerical integration. (1) The Tetrahedron symmetry integration uses 4 points on the sphere to calculate the integral<sup>11</sup>. (2) The Octahedron symmetry integration uses 6 points and (3) the Icosahedron symmetry integration 12, 24 and 86 points. For a more technical discussion about these integration techniques, see Ref. [MITAS 1991].

### 3.4.3 Pseudopotentials in DMC - The Pseudopotential Localization Approximation

The evaluation of non-local pseudopotentials in VMC can “simply” be obtained by numerical integration in two dimensions and can systematically be controlled. Not so for DMC, there a complication arises with the non-locality of pseudopotentials. In the following, we point out this difficulty which can then be avoided when doing the pseudopotential localization approximation.

In Section 3.3.2, we introduced the Green’s function,  $G = G_{\text{diff}}G_{\text{rate}}$ , when iteratively solving the Schrödinger equation. So far, we interpreted  $G(\mathbf{r}' \leftarrow \mathbf{r}, \delta\tau)$  as the probability amplitude for one walker to move from position  $\mathbf{r}$  to  $\mathbf{r}'$  (in imaginary time). This interpretation is valid if and only if  $G$  is positive. It is clear that the diffusion term,  $G_{\text{diff}}$ , is always positive. This is not so for  $G_{\text{rate}}$ . Let us focus on  $G_{\text{rate}}$  and recall its explicit expression,

$$G_{\text{rate}}(\mathbf{r}, \mathbf{r}', \delta\tau) = \langle \mathbf{r} | e^{-\delta\tau(\hat{V}^e - E_T)} | \mathbf{r}' \rangle. \quad (3.78)$$

If  $\hat{V}^e$  were a local operator, it could be shown that the matrix representation of  $G_{\text{rate}}$  is diagonal with only positive eigenvalues<sup>12</sup>. But for non-local operators, like  $\hat{V}_{\text{nloc}}^{\text{psp}}$ , the matrix representation of  $G_{\text{rate}}$  may also have non-diagonal elements. In turn,  $G_{\text{rate}}$  is not guaranteed to be positive for all  $\mathbf{r}, \mathbf{r}'$  and  $\delta\tau$  [FOULKES 2001].

Following now Ref. [MITAS 1991], the Hamiltonian  $\hat{H}^{\text{e psp}}$  is again written as in eq.(3.76). Then, the importance sampled Schrödinger eq.(3.48) becomes

<sup>11</sup>The integral of a function  $f$  defined on the unit sphere is approximated as  $\frac{1}{4\pi} \int_{4\pi} f(\Omega) d\Omega \approx \frac{1}{4} \sum_{i=1}^4 f(a_i)$ . The  $a_i$  are equally distributed on the sphere [MITAS 1991].

<sup>12</sup>For illustration, the following equality may be used,  $\exp\left\{\begin{pmatrix} a & 0 & 0 \\ 0 & b & 0 \\ 0 & 0 & c \end{pmatrix}\right\} = \begin{pmatrix} e^a & 0 & 0 \\ 0 & e^b & 0 \\ 0 & 0 & e^c \end{pmatrix}$ ,

which then can serve for generalization.

$$\begin{aligned} \frac{df(\mathbf{r}, \tau)}{d\tau} = & \frac{1}{2} \nabla^2 f(\mathbf{r}, \tau) - \nabla[f(\mathbf{r}, \tau) \mathbf{v}(\mathbf{r})] \\ & - \left[ \frac{(\hat{H}_{\text{loc}}^{\text{psp}} - E_T) \Psi_T(\mathbf{r})}{\Psi_T(\mathbf{r})} \right] f(\mathbf{r}, \tau) - \left[ \frac{(\Delta \hat{V}_{\text{nloc}}^{\text{psp}} \Psi)(\mathbf{r})}{\Psi(\mathbf{r})} \right] f(\mathbf{r}, \tau). \end{aligned} \quad (3.79)$$

Please notice the important difference between  $\Psi$  and  $\Psi_T$ .<sup>13</sup> As pointed out above, sampling this equation according to the previous DMC formalism would allow walkers to change their signs. “This is likely to be a very noisy procedure as walkers with opposite signs would almost completely cancel” [MITAS 1991]. It is the last term of eq.(3.79) that contains the non-local part of the pseudopotential,  $\Delta \hat{V}_{\text{nloc}}^{\text{psp}}$ , and gives rise to a potential sign change in the sampling process. The idea now is to get rid of this last term by evaluating  $\Delta \hat{V}_{\text{nloc}}^{\text{psp}}$  not with the unknown wavefunction,  $\Psi$ , but instead with the known trial wavefunction,  $\Psi_T$ . The result is a differential equation with no non-local operators as will be seen as follows.

When adding and subtracting the term  $\Delta \hat{V}_{\text{nloc}}^{\text{psp}} \Psi_T / \Psi_T$  to eq.(3.79), we get

$$\frac{df(\mathbf{r}, \tau)}{d\tau} = \frac{1}{2} \nabla^2 f(\mathbf{r}, \tau) - \nabla[f(\mathbf{r}, \tau) \mathbf{v}(\mathbf{r})] \quad (3.80)$$

$$- \left[ \frac{(\hat{H}_{\text{loc}}^{\text{psp}} + \Delta \hat{V}_{\text{nloc}}^{\text{psp}} - E_T) \Psi_T(\mathbf{r})}{\Psi_T(\mathbf{r})} \right] f(\mathbf{r}, \tau) - \epsilon(\mathbf{r}) f(\mathbf{r}, \tau) \quad (3.81)$$

with

$$\epsilon(\mathbf{r}) = \left[ \frac{(\Delta \hat{V}_{\text{nloc}}^{\text{psp}} \Psi)(\mathbf{r})}{\Psi(\mathbf{r})} - \frac{(\Delta \hat{V}_{\text{nloc}}^{\text{psp}} \Psi_T)(\mathbf{r})}{\Psi_T(\mathbf{r})} \right]. \quad (3.82)$$

The  $\epsilon$ -term is the difference of the pseudopotential applied to the unknown sampled wavefunction,  $\Psi$ , and the trial wavefunction,  $\Psi_T$ . When neglecting this  $\epsilon$ -term, the Schrödinger eq.(3.81) becomes a differential equation with only local terms. Therefore, this approximation is called **Pseudopotential Localization Approximation** and is exact when  $\Psi_T$  is the true ground state wavefunction,  $\Psi_0$ . It can be shown that the localization error in the total energy approaches zero quadratically as  $\Psi_T$  approaches an exact eigenfunction of  $\hat{H}^e$  [MITAS 1991]. But unlike for the fixed-node error, no variational principle holds and nothing can be said about the sign of the pseudopotential localization error.

---

<sup>13</sup> $\Psi^T$  is the fixed guiding function and  $\Psi$  is the wavefunction that becomes the ground state in DMC.

### 3.4.4 Interdependence of the Fixed-Node and Pseudopotential Localization Approximation

What makes it even more difficult to estimate the pseudopotential localization error is its inherent interdependency with the fixed-node approximation. This interdependence becomes evident when considering the expression

$$\frac{\left[ (\hat{H}_{\text{loc}}^{\text{psp}} + \Delta \hat{V}_{\text{nloc}}^{\text{psp}} - E_{\text{T}}) \Psi_{\text{T}} \right] (\mathbf{r})}{\Psi_{\text{T}}(\mathbf{r})}, \quad (3.83)$$

in the previous Schrödinger eq.(3.81). Following a similar discussion in Ref. [MITAS 1991], this expression is singular at the nodal surface where the denominator is zero (and the numerator can be assumed to be non-zero since  $\Psi_{\text{T}}$  is generally not an eigenfunction of these operators). Before doing the pseudopotential localization approximation and omitting the  $\epsilon$ -term in eq.(3.81), these singularities occur twice in this equation but with opposite sign. For that reason, they cancel each other. But when omitting the  $\epsilon$ -term, the cancellation of the two singularities does not happen any more.

Before elaborating on the interdependence of both errors, let us introduce the term “critical regions” for regions that are close to the nodal surface, i.e. where the above expression (3.83) may become large. Now, when walkers sample the ground state, it is possible that some of them move into these critical regions where the trial wavefunction is small. This is possible, since the true ground state wavefunction (which is different from  $\Psi^{\text{T}}$ ) could still have larger amplitudes in these critical regions. And these larger amplitudes also lead to a larger walker density. These walkers would then contribute to a pseudopotential localization error. To conclude, the fixed-node error always results in a contribution in the pseudopotential localization error.

## 3.5 Correlated Sampling

The last section of this chapter will briefly introduce the Correlated Sampling (CS) technique [FILIPPI 2000] which was recently developed and allows to calculate interatomic forces more effectively with both VMC and DMC. The idea of this technique is to introduce statistical correlation for calculating total energies at different nuclear geometries. This correlation then allows to greatly reduce the statistical error when considering differences of those total energies of their respective geometries.

### 3.5.1 Correlated Sampling in VMC

The main idea of this CS technique is to calculate the total energies at different geometries from a single set of sampling points. Following Ref. [FILIPPI 2000], we first

define a primary nuclear geometry  $\mathbf{R}$  (e.g. the experimental equilibrium geometry). For this geometry, a primary set of  $M$  walkers,  $\{\mathbf{r}_i\}_{i=1,\dots,M}$ , may be obtained from distribution  $|\Psi_T(\mathbf{R})|^2$ . A secondary nuclear geometry  $\mathbf{R}^{(s)}$  is then given for a (fixed) nuclear displacement,  $\mathbf{R} \rightarrow \mathbf{R}^{(s)}$ . Based on this displacement,  $\Psi_T$  and  $\hat{H}^e$  are then transformed into  $\Psi_T^{(s)}$  and  $\hat{H}^{e(s)}$  by replacing  $\mathbf{R}$  with  $\mathbf{R}^{(s)}$ . The VMC total energy at the secondary geometry can now be written as

$$E_{\text{VMC}}^{(s)} = \frac{\int \left( \Psi_T^{(s)}(\mathbf{r}) \right)^2 E_L^{(s)}[\Psi_T^{(s)}(\mathbf{r})] d\mathbf{r}}{\int \left( \Psi_T^{(s)}(\mathbf{r}) \right)^2 d\mathbf{r}}, \quad (3.84)$$

with the local energy,  $E_L^{(s)} = \hat{H}^{e(s)}\Psi_T^{(s)}/\Psi_T^{(s)}$ . If one sampled the above equation using Monte Carlo integration, one would need a set of sampling points generated from this secondary distribution,  $|\Psi_T^{(s)}|^2$ . But since the aim of this CS technique is to use the same set of sampling points stemming from the primary distribution  $|\Psi_T|^2$  when sampling eq.(3.84), this equation will be re-written,

$$E_{\text{VMC}}^{(s)} = \frac{\int |\Psi_T(\mathbf{r})|^2 E_L^{(s)}[\Psi_T^{(s)}(\mathbf{r})] \cdot \omega(\mathbf{r}) d\mathbf{r}}{\int |\Psi_T(\mathbf{r})|^2 \cdot \omega(\mathbf{r}) d\mathbf{r}} \approx \frac{\sum_{i=1}^M E_L^{(s)}[\Psi_T^{(s)}(\mathbf{r}_i)] \cdot \omega(\mathbf{r}_i)}{\sum_{i=1}^M \omega(\mathbf{r}_i)}, \quad (3.85)$$

in analogy to eq.(3.28) in Section 3.4.2, with weights

$$\omega := \frac{|\Psi_T^{(s)}(\mathbf{r})|^2}{|\Psi_T(\mathbf{r})|^2}. \quad (3.86)$$

In the last step in eq.(3.85), Monte Carlo integration is applied with the important improvement that only the primary walkers,  $\mathbf{r}$ , are used when obtaining the secondary VMC energy,  $E_{\text{VMC}}^{(s)}$ . This means that  $E_{\text{VMC}}^{(s)}$  is not generated independently from  $E_{\text{VMC}}$ . Hence, the fluctuation of the difference  $E_{\text{VMC}}^{(s)} - E_{\text{VMC}}$  is reduced.

The CS technique applied in this thesis uses eq.(3.85) with a slight modification, the **space-warp coordinate transformation**. This transformation generates so called secondary walkers,  $\mathbf{r}^{(s)}$ , for each primary walker,  $\mathbf{r}$ , with the aim to improve the representation of  $\Psi_T^{(s)}(\mathbf{r})$  by  $\Psi_T^{(s)}(\mathbf{r}^{(s)})$ . For this transformation, it will be assumed that walkers translate rigidly with the nucleus if the walkers are adjacent to the displaced nucleus, whereas this transformation should become less important for walkers at larger distances to any nuclei.

A possible space-warp transformation which fulfills these assumptions and is used in our algorithm is found in

$$\mathbf{r}_i^{(s)}[\mathbf{r}_i] = \mathbf{r}_i + \sum_{\alpha}^{N_{\text{atom}}} (\mathbf{R}_{\alpha}^{(s)} - \mathbf{R}_{\alpha}) \cdot W_{\alpha}(\mathbf{r}_i, \{\mathbf{R}_{\beta}\}), \quad (3.87)$$

where

$$W_\alpha(\mathbf{r}_i, \{\mathbf{R}_\beta\}) := \frac{(\mathbf{r}_i - \mathbf{R}_\alpha)^{-4}}{\sum_{\beta=1}^{N_{atom}} (\mathbf{r}_i - \mathbf{R}_\beta)^{-4}} \quad (3.88)$$

decays sufficiently rapidly for larger electron-nuclear distances [FILIPPI 2000]. Now, when substituting the secondary walkers  $\mathbf{r}^{(s)}$  into eq.(3.85), we obtain

$$E_{\text{VMC}}^{(s)} = \frac{\int |\Psi_T(\mathbf{r}^{(s)})|^2 E_L^{(s)}[\Psi_T^{(s)}(\mathbf{r}^{(s)})] \cdot \omega(\mathbf{r}^{(s)}) d\mathbf{r}^{(s)}}{\int |\Psi_T(\mathbf{r})|^2 \cdot \omega(\mathbf{r}) d\mathbf{r}}. \quad (3.89)$$

With the introduced transformation in eq.(3.87), the integral over  $\mathbf{r}^{(s)}$  in the previous equation can now be reduced to an integral over  $\mathbf{r}$ ,

$$E_{\text{VMC}}^{(s)} = \frac{\int |\Psi_T(\mathbf{r}^{(s)}(\mathbf{r}))|^2 E_L^{(s)}[\Psi_T^{(s)}(\mathbf{r}^{(s)}(\mathbf{r}))] \cdot \omega(\mathbf{r}^{(s)}(\mathbf{r})) \cdot |\mathbf{J}(\mathbf{r})| d\mathbf{r}}{\int |\Psi_T(\mathbf{r}^{(s)}(\mathbf{r}))|^2 \cdot \omega(\mathbf{r}^{(s)}(\mathbf{r})) \cdot |\mathbf{J}(\mathbf{r})| d\mathbf{r}}. \quad (3.90)$$

To account for this transformation in the last equation, the volume element,  $d\mathbf{r}^{(s)} = |\mathbf{J}(\mathbf{r})| d\mathbf{r}$ , is included. Thereby, we use the common Jacobi matrix with matrix elements<sup>14</sup>  $J_{ij}(\mathbf{r}) = \partial \mathbf{r}_i^{(s)} / \partial \mathbf{r}_j$  which are determined by the transformation in eq.(3.87). When applying Monte Carlo integration again, the last equation finally becomes

$$E_{\text{VMC}}^{(s)} \approx \frac{\sum_{i=1}^M E_L^{(s)}[\Psi_T^{(s)}(\mathbf{r}_i^{(s)}(\mathbf{r}_i))] \cdot \omega(\mathbf{r}_i^{(s)}(\mathbf{r}_i)) \cdot \mathbf{J}(\mathbf{r}_i)}{\sum_{j=1}^M \omega(\mathbf{r}_j^{(s)}(\mathbf{r}_j)) \cdot \mathbf{J}(\mathbf{r}_j)}, \quad (3.91)$$

which is sampled at the primary set of walkers. To conclude, the total energies,  $E_{\text{VMC}}$  and  $E_{\text{VMC}}^{(s)}$ , at the primary and secondary geometries are sampled with the same reference set of walkers leading to a substantial reduction in the fluctuation when considering their differences.

### 3.5.2 Correlated Sampling in DMC

The implementation of CS in DMC resembles the methodology described for VMC with one additional modification, the branching (birth/death) process. To account for this branching, the primary and secondary walkers (see last section) must be re-weighted according to a branching factor. In particular, for the primary walkers this re-weighting factor is the one from a normal DMC calculation,  $e^{-\delta\tau(E_L(\mathbf{r}') + E_L(\mathbf{r}) - 2E_T)/2}$ , see eq.(3.59). For the secondary walkers, the factor is obtained similarly, whereas

<sup>14</sup> $\mathbf{J}$  is a  $(3M \times 3M)$ -dimensional matrix where  $J_{ij}(\mathbf{r}) = \partial \mathbf{r}_i^{(s)} / \partial \mathbf{r}_j$  is a  $(3 \times 3)$ -dimensional sub-matrix since  $\mathbf{r}_i$  and  $\mathbf{r}_i^{(s)}$  are 3 dimensional vectors.

the local energy,  $E_L^{(s)} = \hat{H}^{e(s)} \Psi_T^{(s)} / \Psi_T^{(s)}$ , in the re-weighting factor is evaluated at the secondary geometry,  $\mathbf{R}^{(s)}$ . Thereby, the same primary walkers are used in analogy to expression (3.85).

In a diffusion process described by DMC, it is important to notice, that the dynamics of the secondary walkers depend on the dynamics of the primary ones (for all generations). Consequently, the dynamics of the secondary walkers is not necessarily the right one (i.e. as one would find for an independent evolution of walkers for the secondary geometry). We will see later that the DMC total energy for the secondary geometries are upper bounds for the true DMC total energy.

### 3.5.3 Re-Centered versus Orbitals Re-Optimized Correlated Sampling

The described CS method in VMC and DMC is also referred to as **re-centered CS method** which uses one reference trial wavefunction obtained at the primary geometry. In this method, the secondary trial wavefunction,  $\Psi^{(s)}$  in eq.(3.85), is obtained by replacing (re-centering) the primary with the secondary nuclear geometry. An improvement upon this method is obtained when the secondary trial wavefunction is not “simply” based on this re-centering procedure. But in addition, the HF determinant is re-optimized with a HF calculation for the secondary geometry before constructing the secondary trial wavefunction. The re-optimized determinants then allow for a more accurate description of the secondary trial wavefunction, known as **orbital re-optimized CS method**. A further improvement can be achieved when the Jastrow parameters, in addition to the re-optimized HF orbitals, are optimized at each secondary geometry.

# Chapter 4

## Results

The last section gave a theoretical description of both the VMC and DMC methods. This chapter presents and discusses the results we obtained through their applications. Calculated VMC and DMC binding energies, equilibrium geometries and vibrational frequencies for a set of molecules will be compared with reference values by other quantum chemical methods. At the end of this chapter, we discuss VMC and DMC results for H-bonds in malonaldehyde and di-ammonia.

### 4.1 Binding Energies

The correlation and binding energies are investigated for nine molecules:  $\text{H}_2$ ,  $\text{N}_2$ ,  $\text{O}_2$ ,  $\text{OH}$ ,  $\text{CO}$ ,  $\text{Si}_2$ ,  $\text{H}_2\text{O}$ ,  $\text{NH}_3$  (ammonium) and  $\text{C}_3\text{O}_2\text{H}_4$  (malonaldehyde). These molecules are chosen to assess VMC and DMC calculations for a set of molecules with different electron configurations and bond types. The  $\text{H}_2$  molecule is special as it is a two electron system with a nodeless wavefunction. For that reason, no fixed-node error occurs. This is contrary to all atoms and molecules with more than two electrons.  $\text{H}_2$  together with  $\text{H}_2\text{O}$ ,  $\text{NH}_3$  and  $\text{OH}$  are X-H type molecules with single bonds. The  $\text{OH}$  radical,  $\text{O}_2$  and  $\text{Si}_2$  are molecules with non-zero total spin and an open shell electron configuration, where the latter two molecules,  $\text{O}_2$  and  $\text{Si}_2$ , have double bonds. All molecules investigated are based on first row elements, except for the second row  $\text{Si}_2$ , that is also interesting for its large inter-nuclear distance. The iso-electronic molecules  $\text{CO}$  and  $\text{N}_2$  are troublesome due to their triple bonds. Quantum chemical calculations reflect this, showing severe problems for  $\text{N}_2$  to achieve chemical accuracy [FELLER 1998]. We chose malonaldehyde ( $\text{C}_3\text{O}_2\text{H}_4$ ) for its strong H-bond contributing to the binding energy (explicitly discussed in Section 4.4).

### 4.1.1 Terminology - Binding Energy

The theoretical **binding energy**,  $E^b$ , is defined as difference obtained from the molecular and atomic total energies given in eq.(2.9). For the molecule, the total energy has been calculated within the harmonic approximation of the Born-Oppenheimer surface around the equilibrium geometry,  $\mathbf{R}_0$  (see also Appendix A.1),

$$E_0^{\text{tot}}(\text{molecule}) = E_0^{\text{BOS}}(\mathbf{R}_0) + \sum_{i=1}^{3M-5 \text{ or } 6} \frac{\hbar\omega_i}{2}. \quad (4.1)$$

$M$  is the number of nuclei and  $\omega_i$  are the harmonic vibrational frequencies, where  $i$  denotes all degrees of freedom for internal vibrations<sup>1</sup>. The second addend corresponds to the nuclear vibrational energy at zero temperature and is referred to as **zero point energy**,  $E_{\text{zpe}}$ . To compare with available experimental data, we consider the experimentally measurable Gibbs free energy. It relies on a finite temperature and pressure. The reader should notice that all experimental binding energies later on will refer to zero temperature.

When solving the many-particle Schrödinger eq.(2.1), relativistic effects are omitted. Yet, relativistic corrections are proportional to the forth power of the nuclear charge, and thus negligible for light second row elements [KOCH 2001].

The **correlation contribution to the binding energy** is defined in eq.(2.19) when replacing the total with the binding energy. Also, molecular **bond orders** will be used to describe and define chemical bonds,

$$\text{Bond Order} := \frac{N_{\text{bond}} - N_{\text{anti-bond}}}{2}, \quad (4.2)$$

where  $N_{\text{bond}}$  and  $N_{\text{anti-bond}}$  are the number of bonding and anti-bonding orbitals within the molecular orbital scheme.

### 4.1.2 Technicalities

#### Construction of the Trial Wavefunction, $\Psi_T$

For all binding energy calculations, the trial wavefunction,  $\Psi_T$ , is constructed with the  $\mathcal{J}(553)$  Jastrow factor (introduced in Section 3.2.2) and with a single Slater determinant. The Slater determinant is previously obtained by a HF calculation using the program package GAMESS [SCHMIDT 1993]. Thereby, we use HF basis sets with radial contracted Gaussian type orbitals (GTO) centered on the nuclei (see Appendix 4.A for a definition of GTOs and the explicit documentation of the construction of our

<sup>1</sup>The number of internal vibrations is  $3M - 6$  for  $M > 2$ . For  $M=2$ , the number of internal vibrations is 1.



basis sets). Depending on the spin state of our molecules, two types of HF calculations are performed, i.e. RHF for closed shell and ROHF for open shell electron configurations (introduced in Section 2.3). For atoms and molecules, Table 4.1 presents (1) the used HF methods, (2) the spin quantum number,  $s$ , of the total spin,  $\langle \hat{S} \rangle$ , (3) the multiplicity,  $m$ , of  $\langle \hat{S}_z \rangle$  given by  $2s + 1$  and (4) the respective bond orders. Also, CF pseudopotentials will be used (introduced in Section 3.4).

	H <sub>2</sub> , NH <sub>3</sub> , H <sub>2</sub> O	OH	Si <sub>2</sub> , O <sub>2</sub>	CO, N <sub>2</sub>	C <sub>3</sub> O <sub>2</sub> H <sub>4</sub>	H	C, O, Si	N
HF type	RHF	ROHF	ROHF	RHF	RHF	ROHF	ROHF	ROHF
Spin $s$	0	0.5	1	0	0	0.5	1	1.5
Mult. $m$	1	2	3	1	1	2	3	4
Bond Ord.	1	1	2	3	-	-	-	-

Table 4.1: This table lists the type of HF calculations performed, the spin quantum number  $s$  of the total spin  $\langle \hat{S} \rangle$ , the multiplicity  $m$  of  $\langle S_z \rangle$  and the bond order for all atoms and molecules

## VMC and DMC Calculations

The procedure of a VMC and DMC calculation was explicitly described in Section 3.3 and 3.4. In a VMC calculation, we use 30,000 blocks and a block size of 20 walkers accounting for a total of 600,000 walkers. The optimization procedure of the trial wavefunction is done at 4000 sampling points and is performed five times (i.e. the cycle of re-calculating the sampling points with VMC and re-optimizing  $\Psi_T$ ). From these cycles, we then take the best trial wavefunction which has the smallest variance  $\sigma_{\text{VMC}}^2$ . Usually, the lowest variance also corresponds with the lowest total energy,  $E_0^e$ . However, in instances where this is not the case in our calculations (possibly due to a statistical error in the variance itself), we choose the  $\Psi^T$  with the lowest variance (see Figure 3.4 for an illustration of plotted variances and respective total energies).<sup>2</sup>

Based on the chosen trial wavefunction, a subsequent DMC calculation is performed. The diffusion time step is  $\delta\tau=0.1 \text{ Ha}^{-1}$ , the number of diffusion blocks is 4,000 with a block size of 50 steps and a population of 40 walkers (this results in 8 million accepted sampling points during a single DMC run). For all VMC and DMC calculations, the experimental equilibrium geometries are used as listed in Table 4.6.

<sup>2</sup>There is a controversial debate if the lowest variance or the lowest total energy gives a more reliable criterion for selecting the best  $\Psi_T$  since both are afflicted with a statistical error [F. Schautz, private communication]. However, we chose the variance as criterion to be consistent.

### Zero Point Energy and Error Bars

Treated within the harmonic approximation, the zero point energy in eq.(4.1) is calculated from the harmonic vibrational frequencies,  $\omega_i$ . For the molecules  $\text{H}_2$ ,  $\text{N}_2$ ,  $\text{O}_2$ ,  $\text{CO}$  and  $\text{H}_2\text{O}$ , all frequencies are calculated with HF, VMC and DMC as presented in Section 4.3. For  $\text{Si}$ ,  $\text{OH}$  and  $\text{NH}_3$ , experimental frequencies are taken from Ref. [NIST 2003]. For  $\text{C}_3\text{O}_2\text{H}_4$ , all (twenty-one) frequencies are considered from a DFT PBE-LDA calculation and are taken from Ref. [ISMER 2002].

For the calculated binding energy, the statistical error bar is calculated as a sum of the statistical error bars of the molecule and of the free atoms. We use the standard notation for a statistical error bar, i.e.  $18.29(1) := 18.29 \pm 0.01$ . Notice that the probability of being within one standard deviation is 67%, within two standard deviations 95% and within three 99.7%. All unit-conversions used are listed in Appendix A.6.

### 4.1.3 Results and Discussion

For all investigated molecules, Table 4.2 lists the calculated HF, VMC and DMC total and binding energies. Deviations with respect to experimental binding energies are presented in Table 4.3.<sup>3</sup>

We begin our discussion by presenting our results obtained by DMC. For all molecules, the calculated negative binding energies show an overestimation on average by 0.2 eV (or 3.2%) with respect to experimental values.<sup>4</sup> In particular, the best agreement with experiment is found for  $\text{H}_2$  with a deviation of 0.002(3) eV. Here, we see that the absence of nodes in the  $\text{H}_2$ -wavefunction allows for a very accurate prediction of the experimental binding energy. For all other molecules, we find deviations which are larger than chemical accuracy ( $\approx 0.043$  eV). We find that the group of the three X-H-type molecules,  $\text{H}_2$ ,  $\text{NH}_3$  and  $\text{OH}$  with single bonds, have results closest to the experimental values (i.e. with deviations of less than -0.14 eV). The largest deviation is observed for the triple-bonded  $\text{N}_2$  (-0.47 eV), followed by the double-bonded  $\text{O}_2$  (-0.41 eV). At the same time,  $\text{N}_2$  and  $\text{O}_2$  also show the largest contributions to the DMC correlation energy per electron, i.e.  $E_{C/e} = 1.12$  eV for  $\text{N}_2$  with 10 electrons and  $E_{C/e} = 1.15$  eV for  $\text{O}_2$  with 12 electrons (see Figure 4.1). These largest correlation contributions suggest that correlation effects are particularly important for molecules with multiple bonds.

When comparing the DMC results with those obtained by VMC, we find that DMC binding energies clearly show systematically improved results. The largest improvement upon VMC binding energies by DMC are found for  $\text{CO}$  (-0.95 eV), for  $\text{O}_2$  (-0.92

<sup>3</sup>Binding energies are noted as negative quantities throughout this thesis. Please note then, an overestimation of the binding energy is equivalent to an underestimation of its absolute value!

<sup>4</sup>Since the experimental binding energy for malonaldehyde is about one order of magnitude larger than for all the others, it is omitted in all following averages.

		$E_{\text{atom}}$ [in Ha]	$E_{\text{molecule}}$ [in Ha]	$E_{\text{zpe}}$ [in eV]	$E^{\text{b}}$ [in eV]	$E_{\text{expt}}$ [in eV]
$\text{H}_2$	HF	-0.5000	-1.1330	-0.271	-3.347	
	VMC	-0.5000	-1.1722(2)	-0.277	-4.409(6)	
	DMC	-0.5000	-1.1746(1)	-0.274	-4.477(3)	-4.480
$\text{N}_2$	HF	-9.6478	-19.4751	-0.169	-4.715	
	VMC	-9.7584(4)	-19.8390(9)	-0.159	-8.61(4)	
	DMC	-9.7692(1)	-19.8853(2)	-0.149	-9.29(1)	-9.761
$\text{O}_2$	HF	-15.6658	-31.3650	-0.122	-0.787	
	VMC	-15.8355(6)	-31.814(1)	-0.108	-3.79(7)	
	DMC	-15.8487(3)	-31.8741(8)	-0.103	-4.71(2)	-5.117
$\text{Si}_2$	HF	-3.6806	-7.4212	-0.032	-1.6001	
	VMC	-3.7537(3)	-7.5906(6)	-0.032	-2.23(3)	
	DMC	-3.7658(1)	-7.6450(3)	-0.032	-3.05(1)	-3.225
CO	HF	-5.3191	-21.2652	-0.141	-7.486	
	VMC	-5.3986(3)	-21.606(1)	-0.141	-9.97(6)	
	DMC	-5.4096(1)	-21.6650(5)	-0.138	-10.93(2)	-11.110
OH	HF		-16.2683	-0.251	-2.538	
	VMC		-16.4759(9)	-0.232	-3.59(4)	
	DMC		-16.5136(3)	-0.232	-4.26(1)	-4.393
$\text{H}_2\text{O}$	HF		-16.9058	-0.555	-5.976	
	VMC		-17.1827(9)	-0.585	-8.86(4)	
	DMC		-17.2116(2)	-0.585	-9.29(1)	-9.510
$\text{NH}_3$	HF		-11.4594	-0.895	-7.584	
	VMC		-11.7131(9)	-0.895	-11.48(4)	
	DMC		-11.7380(4)	-0.895	-11.86(1)	-11.999
$\text{C}_3\text{O}_2\text{H}_4$	HF		-50.3279	-1.784	-26.489	
	VMC		-51.261(2)	-1.784	-36.2(1)	
	DMC		-51.3997(8)	-1.784	-38.31(5)	-39.383

Table 4.2: This table shows calculated HF, VMC and DMC total and binding energies. The zero point energies are calculated as stated in the text. All experimental binding energies are taken from Ref. [POPLE 1992] except for silicon and  $\text{C}_3\text{O}_2\text{H}_4$  which are taken from Ref. [NIST 2003]. Note that for CO in the  $E_{\text{atom}}$  column, the listed energies refer to the C-atom.

	$\Delta E_{\text{HF}}^{\text{b}}$		$\Delta E_{\text{VMC}}^{\text{b}}$		$\Delta E_{\text{DMC}}^{\text{b}}$		Bond Ord.
	[in eV]	[in %]	[in eV]	[in %]	[in eV]	[in %]	
H <sub>2</sub>	1.132	25.3	0.069(6)	1.5	0.002(3)	0.1	1
N <sub>2</sub>	5.046	51.7	1.151(46)	11.8	0.468(13)	4.8	3
O <sub>2</sub>	4.329	84.6	1.327(65)	25.9	0.411(22)	8.0	2
Si <sub>2</sub>	1.624	50.4	0.992(31)	30.8	0.172(15)	5.3	2
CO	1.854	42.2	1.134(63)	10.2	0.182(24)	1.6	3
OH	3.624	32.6	0.805(41)	18.3	0.137(14)	3.1	1
H <sub>2</sub> O	3.533	37.8	0.646(14)	6.8	0.219(14)	2.3	1
NH <sub>3</sub>	4.414	36.8	0.521(36)	1.1	0.136(15)	1.1	1
C <sub>3</sub> O <sub>2</sub> H <sub>4</sub>	12.9	32.8	3.213(107)	8.2	1.069(47)	2.7	1&2

Table 4.3: This table shows the deviations of the binding energies with respect to the experimental values calculated with HF, VMC and DMC. All values are based on those in Table 4.2.

eV) and for Si (-0.82 eV). The smallest improvements are found for all X-H type molecules, ranging between -0.07 eV (H<sub>2</sub>) and -0.67 eV (OH). These findings show that VMC results are not sufficient and can substantially be improved by a DMC calculation.

For all our VMC and DMC results, we also find a systematic overestimation of the binding energies. These overestimations imply that either the negative molecular total energies are too high or the atomic energies are too low. Let us focus on VMC first. Since the variational character of VMC only allows positive errors, the overestimation in the binding energy must be a result of a larger error in the molecular total energy. In turn, the same variational principle in quantum mechanics implies that the correlated VMC trial wavefunctions must be poorer (i.e. has a larger deviation from the true wavefunction) for molecules than for atoms. We can use the finding of poorer trial wavefunctions for molecules when further discussing our DMC results. Supposing that a poorer trial wavefunction leads to a poorer nodal surface, the fixed-node error would then be larger in molecules than in atoms. Since the fixed-node approximation is variational, this would explain (at least part of) the overestimation in the molecular DMC total and binding energies.

Besides the fixed-node error, also other errors might play a role in the overestimation of the DMC binding energies. The time step will be discussed in Section 5.5 and is found to have an influence on the overestimation of the N<sub>2</sub> binding energy as large as 0.1 eV (2.5 mHa). Also, the pseudopotential localization error can have a significant influence. Since a substantial part of this thesis is devoted to help explaining these deviations, we will commit the entire Chapter 5 to further examine possible errors.

To conclude, we find that VMC calculations are not sufficient when calculating total and binding energies and can be substantially improved with a subsequent DMC calculation. Also, the findings from our selected set of molecules suggest that X-H

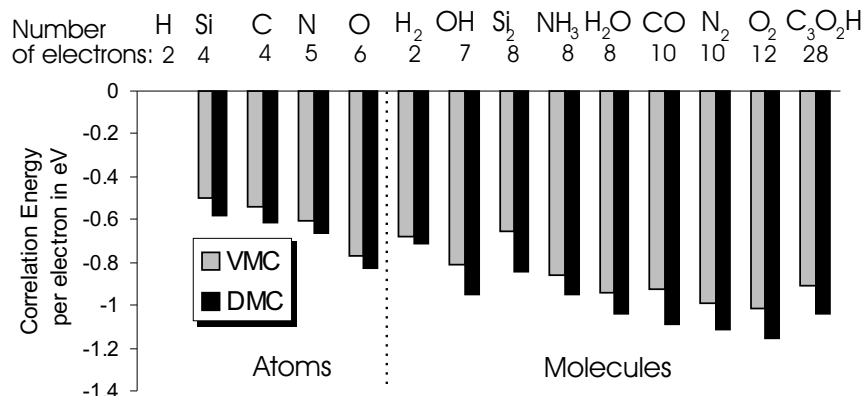


Figure 4.1: For all atoms and molecules, this table shows the VMC and DMC correlation energies divided by the number of valence electrons. All energies are based on Table 4.2.

type molecules with single bonds are relatively better described than others. For the multiple-bonded molecules  $N_2$  and  $O_2$ , our calculations show the largest deviations from the experimental binding energies. But at the same time, we find that correlation effects are particularly important for these two molecules. Also, our results show that the atoms are already better described in VMC and DMC calculations than compared to molecule. This will be further investigated in Chapter 5.

#### 4.1.4 Comparison with other Quantum Chemical Methods and DMC References

This section aims to compare our QMC binding energies with reference values by quantum chemical<sup>5</sup> and density functional methods. In order to do so, we briefly introduce two main quantum chemical approaches in addition to density functional theory.

1. Based on many-body perturbation theory, the second order perturbation method **Møller-Plesset (MP2)** [Moller 1934] is the least-expensive traditional method. It approximately accounts for correlation energy most economically compared to other quantum chemical approaches. And it scales with system size,  $O(m^5)$ , where  $m$  is a measure of the molecular size [KOCH 2001]. Beyond MP2, the more expensive **Coupled Cluster (CC)** method is complete to the infinite order in perturbation theory but is limited to a subset of possible excitations. CCSD(T)

<sup>5</sup>Generally, quantum chemical methods refer to post-Hartree Fock techniques which include static and dynamic correlation.

is a commonly used CC method which includes single, double and approximate (perturbatively determined) triple excitations.

2. An alternative to CC is the **Configuration Interaction (CI)** method (already introduced in Section 2.4). The QCISD(T) [POPLE 1987] is a commonly used CI method that includes single, double and triple single-orbital excitations as well as quadratic corrections. Both methods, CCSD(T) and QCISD(T) are among the most accurate, but also most computational expensive wavefunction based techniques available. They both scale with  $O(m^7)$ , whereas for comparison, the HF method scales with  $O(m^4)$  [KOCH 2001].
3. When compared to previous quantum chemical methods, **Density Functional Theory (DFT)** is the most cost effective method to account for correlation energies. Its scaling factor is similar or even better than for HF<sup>6</sup>. Rather than being based on a wavefunction, the energy is computed as a functional of the electron density. The DFT method is exact in theory, however, it requires approximations for the exchange-correlation functional. The **BLYP** approach with the Becke exchange functional and the Lee-Yang-Parr correlation functional [LEE 1988] is widely used. The improved **B3LYP** hybrid functional additionally includes the exact exchange.

The following comparison in Table 4.4 refers to quantum chemical methods in their standard approaches using basis sets that are commonly used in quantum chemistry. Thereby, we present results obtained for two different basis sets. The first basis, 6-311G\*, is very similar to ours with the same number of GTOs [POPLE 1992] and is listed in the first line for each molecule in that table. The second basis, cc-pCVTZ, is three times larger [FELLER 1998] and is listed in the second line for each molecule.<sup>7</sup> Then, we compare with more accurate but very costly CCSD(T) reference calculations where the basis set limit is extrapolated beyond the aug-ccpV5Z basis [FELLER 1998]. To put our findings in perspective, we then compare our results with reference results for a broader set of molecules. Figure 4.2 illustrates the deviations from experimental values for VMC and DMC and for all reference methods with the larger basis set.

We begin the discussion by considering the average absolute deviations of the calculated and reference binding energies from the experimental value (listed at the bottom of Table 4.4). For the larger basis, the average deviations of the BLYP, MP2 and CCSD(T) values are very similar as for DMC (0.22 eV). When comparing to CCSD(T), the DMC results are better for the X-H molecules and slightly worse for the other molecules. A significant improvement by about a factor of 3 is obtained for B3LYP compared to all other averages. This improvement also holds for all individual

<sup>6</sup>A definite scaling number in DFT depends on the basis and functionals chosen. The scaling is  $O(m^4)$  for the B3LYP,  $O(m^3)$  for LDA or GGA and can even be reduced to  $O(m^1)$  with additional approximations.

<sup>7</sup>Used basis set abbreviations can be found in Ref.[JENSEN 2002].

this work		references						
$\Delta E_{\text{HF}}$	$\Delta E_{\text{QMC}}$	$\Delta E_{\text{HF}}$	$\Delta E_{\text{BLYP}}$	$\Delta E_{\text{B3LYP}}$	$\Delta E_{\text{MP2}}$	$\Delta E_{\text{QCISD}}$	$\Delta E_{\text{CCSD(T)}}$	$\Delta E_{\text{CCSD(T)}}^{\text{limit}}$
<b>H<sub>2</sub></b>								
1.132	-0.002(3)	1.189	0.005	-0.012	0.725	0.525	-	-
		1.111	0.003	-0.034	0.255	-	-0.220	-
<b>N<sub>2</sub></b>								
5.046	0.47(1)	5.203	-0.269	0.250	0.563	1.422	-	-
		4.880	-0.488	0.016	-0.0024	-	0.364	0.104
<b>O<sub>2</sub></b>								
4.33	0.41(2)	3.864	-0.815	-0.172	0.017	0.824	-	-
(4.033 <sup>UHF</sup> )		3.721	-0.683	-0.0130	0.190	-	0.189	0.075
<b>Si<sub>2</sub></b>								
1.624	0.18(2)	1.783	0.058	0.216	0.716	0.784	-	-
		1.516	-0.110	0.079	0.289	-	0.141	0.000
<b>OH</b>								
1.854	0.13(1)	1.891	0.117	0.190	0.72	0.755	-	-
		1.683	-0.072	-0.012	0.151	-	-0.074	0.013
<b>CO</b>								
3.624	0.18(2)	3.812	-0.052	0.308	0.082	0.815	-	-
		3.690	-0.112	0.192	-0.267	-	0.189	0.068
<b>H<sub>2</sub>O</b>								
3.533	0.22(1)	3.799	0.52	0.615	1.323	1.544	-	-
		3.3	0.121	0.186	0.169	-	-0.257	0.032
<b>NH<sub>3</sub></b>								
4.414	0.14(2)	4.632	0.290	0.321	1.959	1.976	-	-
		4.251	-0.085	-0.062	0.461	-	-0.503	0.070
Average absolute deviation								
<b>3.19</b>	<b>0.22</b>	<b>3.27</b>	<b>0.26</b>	<b>0.26</b>	<b>0.76</b>	<b>1.08</b>	-	-
		<b>3.02</b>	<b>0.21</b>	<b>0.07</b>	<b>0.22</b>	-	<b>0.27</b>	<b>0.05</b>

Table 4.4: This table compares the deviation of the binding energies from experimental values in eV for our HF and DMC calculations and reference HF, BLYP, B3LYP, QCISD(T) and CCSD(T) calculations. For each molecule, the first row refers to values obtained for the 6-311G\* basis set and are taken from Ref. [POPLE 1992]. The second row refers to values obtained for the cc-pCVQZ basis, there the CCSD(T) values are obtained from [Feller, private communication] and all others from Ref. [NIST 2003]. In the last column, the CCSD(T) limit is additionally presented from Ref. [FELLER 1998] and was obtained by an exponential fit over the total energies obtained for the aug-cc-pVDZ through the aug-ccpV5Z basis. For all listed binding energies, the zero point energy is included. For all references, the binding energies are obtained at the bond length optimized within each method, whereas for HF and DMC calculations, experimental bond lengths are chosen from Table 4.6. In addition to our RHF or ROHF calculations for all molecules as specified in the Table 4.1, we also show the calculated UHF binding energy for O<sub>2</sub>.

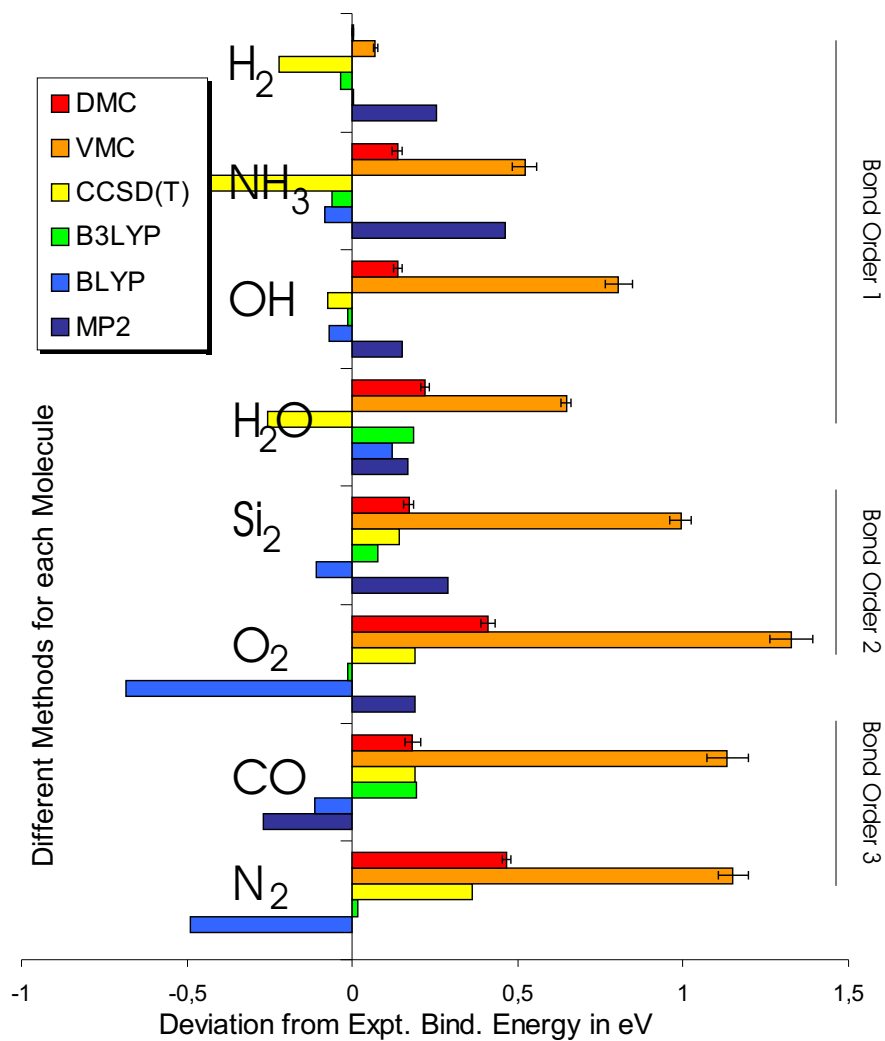


Figure 4.2: This table compares the deviation of the binding energies from experimental values in eV for our VMC and DMC calculations and reference BLYP, B3LYP and CCSD(T) calculations. All values are taken from Table 4.4 with the larger basis set, cc-pCVTZ. The CCSD(T) values are obtained from [Feller, private communication] and all others from Ref. [NIST 2003].



values. This is not surprising since the B3LYP hybrid functional is fitted to the set of G2 molecules<sup>8</sup> to reproduce the experimental binding energies. And our molecules are a subset of G2. The largest average deviation is obtained for HF which is about one order of magnitude larger than for all other methods. Thereby, it should be noted that our HF values agree fairly well with those reference HF values.<sup>9</sup>

In the previous section, we discussed the systematic overestimation of the VMC and DMC binding energy with respect to the experimental value. For all reference methods except for HF, no such a trend can be seen. This is not surprising since these methods do not guarantee to yield equally good atomic or molecular energies. And DFT methods in particular do not provide an upper bound of the total energy. A last observation in this context is the dependence on the basis set of all reference methods. The average deviation from the experimental value reduces for all listed reference methods in Table 4.4 when increasing the basis set. In particular, the reduction for MP2 and B3LYP is by a factor 4. But for BLYP, this improvement is not guaranteed for each molecule, like for N<sub>2</sub>. These results show that both, DFT and quantum chemical methods have a strong dependence on the chosen basis sets. The basis set dependence for QMC will be discussed in Section 5.2.

So far, we compared to reference methods in their standard approaches with commonly used basis sets. In particular for CI and CC methods, further systematic improvement can be achieved when increasing the basis set. Yet, at the same time the numerical effort increases drastically. The last column in Table 4.4 lists results obtained for such an extensive CCSD(T) study. There, the total energies are calculated by an exponential fit through the results obtained for different basis sets up to the aug-ccpV5Z basis. The obtained average absolute deviation by 0.05 eV has the best agreement with experimental values compared to all previous reference and DMC results. However, in Chapter 5 we will show that DMC results can likewise be improved. It is worth mentioning that the largest deviation for CCSD(T) of 0.10 eV is also found for N<sub>2</sub>.

To put our findings in perspective, we now compare with results for the broader G2 test set. We find that BLYP and B3LYP yield slightly larger average deviations for the G2 set compared to our subset of molecules, i.e. 0.32 eV for BLYP and 0.14 eV for B3LYP [PERDEW 2003]. For CCSD(T), we find very similar average deviations for the G2 set and our subset of molecules, i.e. 0.27 eV for the cc-pVTZ basis and 0.06 eV for the complete basis set limit [FELLER 1998]. This comparison suggests that our limited set of selected molecules is already a good representation for a broader set of molecules.

---

<sup>8</sup>The G2 test set consists of 148 molecules, which are listed for example in Ref. [FELLER 1998] and are a selection of first and second row molecules.

<sup>9</sup>It should be said that all reference HF calculations are obtained by an UHF calculation, whereas ours are obtained for RHF or ROHF as stated in Table 4.1. We have additionally listed the UHF value in Table 4.4 for O<sub>2</sub>, since our RHF value previously disagreed by about 0.5 eV from the UHF reference value.

in [eV]	N <sub>2</sub>	O <sub>2</sub>	Si <sub>2</sub>	OH	CO	H <sub>2</sub> O	NH <sub>3</sub>
this work	0.47(1)	0.41(2)	0.18(2)	0.13(1)	0.18(2)	0.22(1)	0.14(2)
reference	0.18(3)	0.27(2)	0.046(9)	0.004(9)	0.13(1)	0.004(9)	0.009(9)

Table 4.5: This table compares our DMC results with those obtained in a recent DMC reference study [GROSSMAN 2002]. In particular, deviations from the experimental binding energies (taken from Table 4.2) are listed.

Before finishing this section, we like to compare our DMC binding energies with a recent DMC reference study, listed in Table 4.5. For our set of molecules, this reference study presents an average absolute deviation of 0.08 eV with respect to the experimental binding energy. This deviation is more than twice as small as compared to our results. In particular, the deviation of the N<sub>2</sub> binding energy is determined to be 0.18(3) eV and is significantly smaller than our deviation of 0.47(1) eV. These differences might have several reasons, like the use of different pseudopotentials or basis sets. The examination of these differences will be part of Chapter 5. However, it can be anticipated that this deviations remain largely unclarified.

To conclude this comparison, we find that our DMC binding energies compete with DFT methods and quantum chemical methods in their standard approaches. However, we have seen that CCSD(T) calculations can be further improved and yield results close to chemical accuracy, yet, at the expense of large numerical effort. But we will show in Chapter 5 that also our DMC results can be significantly improved when increasing the number of determinants in the trial wavefunction or when using different pseudopotentials. In the same Chapter 5, we also hope to clarify the significant differences between our and the reference DMC calculations.

## 4.2 Equilibrium Geometries

In this section, we will investigate the equilibrium geometries for the five molecules H<sub>2</sub>, H<sub>2</sub>O, O<sub>2</sub>, N<sub>2</sub>, and CO, (with bond orders 1, 1, 2, 3, 3, respectively).

### 4.2.1 Terminology

In experimental molecular spectroscopy, the common definition of the equilibrium geometry,  $\mathbf{R}_e = (\mathbf{R}_{1e}, \dots, \mathbf{R}_{Me})$ , for a system of  $M$  nuclei is defined as the global minimum on the Born-Oppenheimer surface [given in eq.(A.1), see Appendix A1]. The **equilibrium bond length** is the distance between two neighboring nuclear coordinates,  $r_{ije} = |\mathbf{R}_{ie} - \mathbf{R}_{je}|$ . Other definitions exist in addition to the one presented. For example, the ground state equilibrium geometry,  $\mathbf{R}_0$ , is defined as the expectation value of the bond length in the ground state. And it differs from  $\mathbf{R}_e$  by considering

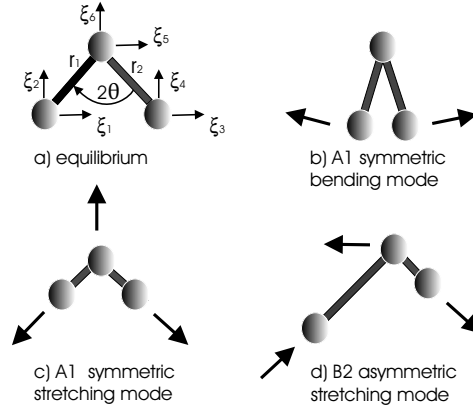


Figure 4.3: The figure a) defines the Cartesian and the polar coordinates to describe the atoms of the water molecule, H-O-H, and b)-d) illustrate its three vibrational frequency modes.

the zero point motion<sup>10</sup>[BANEWELL 1994]. The ambiguity in defining equilibrium geometries is due to the lack of direct measurements for bond lengths (see also Ref. [BANEWELL 1994]). For the theoretical approach in this thesis, we will follow the standard practice and calculate  $\mathbf{R}_e$ .

### The Born-Oppenheimer Surface for Di- and Tri-Atomic Molecules

For di-atomic molecules, the Born-Oppenheimer surface effectively reduces to 1 dimension (i.e. the 6 degrees of freedom for di-atomic molecule are 3 for translations, 2 for rotations and 1 for internal vibrations). For tri-atomic molecules, the Born-Oppenheimer surface is effectively 3-dimensional (i.e. the 9 degrees of freedom are 3 for translations, rotations and vibrations). Figure 4.3 illustrates the 3 vibrational normal modes of the water molecule.

Obtaining the 3-dimensional Born-Oppenheimer surface using QMC methods is very costly due to the large amount of required grid points in real space (7 grid points in each dimension would require 343 points at which the total energy needs to be calculated). To save a substantial amount of computer time, we use a model that effectively maps the 3-dimensional Born-Oppenheimer surface onto 2 dimensions.

The idea of that mapping was suggested by [LANDAU 1963, STRUVE 1989] and is exact for infinitesimal displacements of the atoms from their equilibrium geometry position,  $\mathbf{R}_e$ . First, this model assumes a harmonic treatment of the Born-Oppenheimer surface around  $\mathbf{R}_e$  resulting in the  $(3 \times 3)$ -dimensional force matrix  $\mathbf{H}$  (see Appendix

<sup>10</sup>For comparison, the difference between  $r_e$  and  $r_0$  is 0.01 Å for H<sub>2</sub> and 0.003 Å for N<sub>2</sub> [ENGELKE 1984].

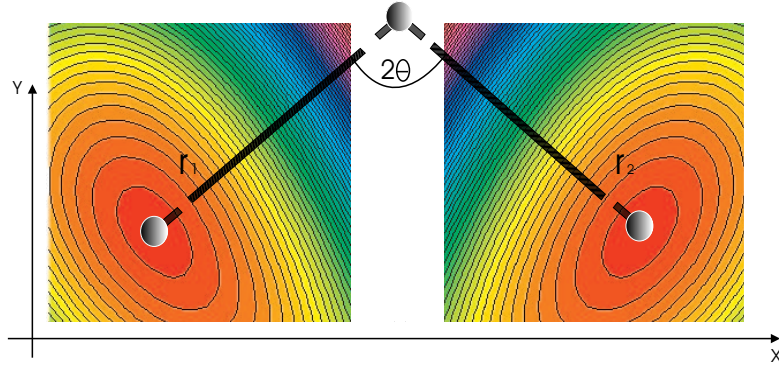


Figure 4.4: This figure shows schematically the two-dimensional BOS for the water molecule dependent on two coordinates. Here, we chose the  $x$ - and  $y$ - axis but these can be transformed into polar coordinates  $r$  and  $2\Theta$ . To obtain this two-dimensional BOS, a second order polynomial in two coordinates (with 12 monomials) is fitted to the total energy at the corresponding grind points.

A1). The second assumption is that the force matrix is diagonal when choosing relative coordinates  $S_i$  with  $i = 1, 2, 3$  as eigenvectors. These are

$$S_1 = r_1 - r_e, \quad S_2 = r_2 - r_e \text{ and } S_3 = \Theta - \Theta_e, \quad (4.3)$$

where  $r_1$  and  $r_2$  are the radial bond coordinates and  $2\Theta$  the bond angle. And  $r_e$  and  $2\Theta_e$  are the bond length and angle in equilibrium. (In Cartesian coordinates, the relative coordinates are explicitly stated in eq.(A.7) as illustrated in Figure 4.3.) For these eigenvectors  $S_i$ , the respective eigenvalues (force constants) are  $\kappa_{ie}$ . Both assumptions in this model are true when considering infinitesimal small displacements. And the total energy in that model can be expressed as

$$E_0^{\text{BOS}}(S_1, S_2, S_3) = \frac{1}{2}\kappa_1 S_1^2 + \frac{1}{2}\kappa_2 S_2^2 + \frac{1}{2}\kappa_3 S_3^2, \quad (4.4)$$

where  $E_0^{\text{BOS}}$  is given in eq.(A.2). Since the two force constants  $\kappa_{1e}$  and  $\kappa_{2e}$  are equal for symmetry reasons, the last equation can further be simplified. Based on that equation,  $r_e$  and  $\Theta_e$  can be determined.

### 4.2.2 Technicalities

We use the orbital re-optimized correlated sampling technique in VMC and DMC (introduced in Section 3.5) to obtain the potential energy surface for each molecule. For

di-atomic molecules, the 1-dimensional energy surface is evaluated at 7 geometries that are chosen with an equi-distance of 0.02 Bohr. Thereby, 7 separate HF calculations are performed for each energy curve to determine the HF optimized molecular orbitals. These HF orbitals are then used in the subsequent orbital re-optimized correlated sampling calculations. As reference geometry for each correlated sampling calculation, we use the value of the experimental bond length. All VMC and DMC input parameters are chosen as in Section 4.1. After the VMC and DMC calculations, a fourth order polynomial is fitted to the seven energy values to obtain an analytic expression for the potential energy curve. The equilibrium bond lengths are then determined as minima from these polynomials.

The equilibrium geometry for the H<sub>2</sub>O molecule is obtained according to eq.(4.4). First, we determine the potential energy curve for the approximate stretching mode described along the coordinate  $S_1$ . Thereby, 7 grid points are chosen to symmetrically stretch and compress the two O-H bonds along these two coordinates at a fixed experimental bond angle. Then, we determine the second energy curve for the approximate bending mode described along the coordinate  $S_3$  (bond angle). Thereby, 7 grid points are chosen as to symmetrically bend the two O-H bonds along that coordinate  $S_3$  at a fixed experimental radius. Based on eq.(4.4), the equilibrium geometries  $r_e$  and  $2\Theta_e$  are then determined as minima from the forth order polynomials fitted along each coordinate.

For all bond lengths and angles, the standard deviation of the mean,  $\bar{\sigma}$ , is determined geometrically. First, the total energies are plotted at the seven grid points with respective error bars. Then, two curves are fitted within these error bars allowing these curves to have the largest difference in their bond lengths and angles<sup>11</sup>. The difference in there bond length/angles gives one standard deviation of the mean.

### 4.2.3 Results and Discussion

Table 4.6 shows the calculated HF, VMC and DMC bond lengths and the bond angle for H<sub>2</sub>O. Also, this table shows their deviations from experimental values.

When focusing on bond lengths calculated with DMC, we find the best agreement with experimental values for the two H-X type molecules H<sub>2</sub> and H<sub>2</sub>O, i.e. with an accuracy of 0.000(1) Å for both molecules. These molecules are then followed by the two iso-electronic, triple-bonded N<sub>2</sub> and CO molecules where both have deviations of 0.004(1) Å from experimental values. We find the largest deviation for O<sub>2</sub> with 0.0140(4) Å. Also, despite the good agreement for the H<sub>2</sub>O bond length we find a deviation of the bond angle for H<sub>2</sub>O of 0.7 % or  $\Delta 2\Theta_{\text{DMC}} = 0.8(1)^\circ$  with respect to the experimental bond angle.

<sup>11</sup>More technically, the first fitted curve is positioned as to cross  $E^{\text{BOS}} + \bar{\sigma}$  on one end of the curve and  $E^{\text{BOS}} - \bar{\sigma}$  on the other end, whereas the opposite is done for the second curve.

[in Å]	$r_{\text{HF}}$	$r_{\text{VMC}}$	$r_{\text{DMC}}$	$\Delta r_{\text{HF}}$	$\Delta r_{\text{VMC}}$	$\Delta r_{\text{DMC}}$	$r_{\text{expt}}$
H <sub>2</sub>	0.732	0.740(1)	0.7414(6)	-0.009	-0.001(1)	0.0004(6)	0.741
N <sub>2</sub>	1.073	1.090(1)	1.0900(6)	-0.021	-0.004(1)	-0.0040(6)	1.094
O <sub>2</sub>	1.161	1.194(1)	1.1930(4)	-0.046	-0.013(1)	-0.0140(4)	1.207
CO	1.107	1.117(1)	1.1190(8)	-0.008	0.002(1)	0.0040(8)	1.115
H <sub>2</sub> O	0.946	-	0.957(1)	-0.011	-	0.000(1)	0.957
in [°]	$2\Theta_{\text{HF}}$	$2\Theta_{\text{VMC}}$	$2\Theta_{\text{DMC}}$	$\Delta 2\Theta_{\text{HF}}$	$\Delta 2\Theta_{\text{VMC}}$	$\Delta 2\Theta_{\text{DMC}}$	$2\Theta_{\text{expt}}$
H <sub>2</sub> O	107.25	-	105.3(1)	2.74	-	0.8(1)	104.51

Table 4.6: This table shows the calculated bond lengths and the bond angle (for H<sub>2</sub>O) for HF, VMC and DMC. The experimental values for H<sub>2</sub>O are taken from [CRC] and for all others from [HERZBERG 1979].

When comparing the DMC bond lengths with those obtained by VMC, we find an insignificant improvement by DMC for the H<sub>2</sub> bond length of 0.001(2) Å. For N<sub>2</sub>, the best estimate by DMC corresponds with the VMC value. Yet, in the cases of O<sub>2</sub> and CO, we observe an insignificant worsening of the DMC bond lengths when comparing with their VMC results, i.e. by 0.001(1) Å for O<sub>2</sub> and by 0.002(1) Å for CO.

As a first conclusion, we find that the correlated sampling VMC and DMC methods yield bond lengths that correspond with experimental values within about 0.01 Å. In particular for the two X-H molecules, our calculated bond lengths agree very well with the experimental values. The double-bonded O<sub>2</sub> molecule shows the largest deviation which again reflects the need for an improved nodal surface as discussed in Section 4.1. Also, we find that a correlated sampling VMC method seems sufficiently accurate when calculating bond lengths, unlike for E<sup>b</sup>. Further investigations of systematic dependencies within this correlated sampling method will be presented in Section 5.8.

#### 4.2.4 Comparison with other Reference Methods

This section compares our calculated bond lengths with HF, MP2, BLYP, CISD(T) and CCSD(T) reference values presented in Table 4.7. For illustration, the deviations from the experimental values are plotted in Figure 4.5 for all methods and molecules.

All reference methods within their chosen basis sets do not yield bond lengths better than our DMC results. In particular, the average absolute deviations from the experimental values are 0.007 Å (CC), 0.01 Å (CI), 0.024 Å (BLYP) and 0.024 Å (MP2) compared to VMC and DMC with 0.005(1) Å for both methods. This good description of the bond length within VMC and DMC is also true for each single reference value with O<sub>2</sub> being the exception. For O<sub>2</sub>, CCSD(T) shows a smaller deviation with 0.003 Å from the experimental value. Even for N<sub>2</sub>, an elaborate CCSD(T) reference calculations for a much larger aug-cc-pV5Z basis (see Table B.1) or even a cc-pV6Z

[inÅ]	this work		references				
	$\Delta r_{\text{HF}}$	$\Delta r_{\text{DMC}}$	$\Delta r_{\text{HF(ref.)}}$	$\Delta r_{\text{BLYP}}$	$\Delta r_{\text{MP2}}$	$\Delta r_{\text{QCISD}}$	$\Delta r_{\text{CCSC(T)}}$
H <sub>2</sub>	-0.009	0.0004(6)	-0.011/-0.007	0.007	-0.003	0.005	0.002
N <sub>2</sub>	-0.021	-0.0040(6)	-0.016/-0.017	0.024	0.036	0.020	0.005
O <sub>2</sub>	-0.046	-0.0140(4)	-0.039/-0.048	0.033	0.039	0.014	0.003
CO	-0.008	0.0040(8)	-0.001/-0.005	0.035	0.035	0.030	0.021
H <sub>2</sub> O	-0.011	0.000(1)	-0.010/-0.011	0.023	0.012	0.013	0.003
[in°]	$\Delta 2\Theta_{\text{HF}}$	$\Delta 2\Theta_{\text{DMC}}$	$\Delta 2\Theta_{\text{HF(ref.)}}$	$\Delta 2\Theta_{\text{BLYP}}$	$\Delta 2\Theta_{\text{MP2}}$	$\Delta 2\Theta_{\text{QCISD}}$	$\Delta 2\Theta_{\text{CCSC(T)}}$
H <sub>2</sub> O	2.74	0.8(1)	0.99/1.42	-1.81	-0.51	-0.51	-0.91

Table 4.7: This table compares the calculated bond lengths and the bond angle (for H<sub>2</sub>O) through DMC with MP2, BLYP, CC and CI reference values. For the reference HF values  $\Delta r_{\text{HF(ref.)}}$ , two sets are presented, the first is taken from [POPLE 1992] (basis: 6-31G\*) and the second one from [NIST 2003](basis: cc-pVDZ). The CC reference value for N<sub>2</sub> is taken from Table B.1 (basis: aug-cc-pV5Z, T. Klüner) and the other CC values from [NIST 2003](basis: 6-311G\*). All other reference values are taken from [POPLE 1992](basis: 6-31G\*). The experimental values are taken from [HERZBERG 1979].

basis [LU 2003] still show a deviation of 0.005 Å from the experimental bond length compared to DMC with 0.004 Å. For H<sub>2</sub>O, the best reference bond angles are obtained with MP2 and CISD(T) which both underestimate the angle by 0.5°. CCSD(T) and BLYP underestimate the bond angle by almost one and two degrees, respectively. In comparison, our DMC result overestimates the experimental value by 0.8(1)°.

At the end, we compare our results with two reference QMC studies. Ref. [FILIPPI 2000] presents calculated bond lengths for seven di-atomic first row molecules where the same correlated sampling technique is applied as in our work. For these molecules, that study predicts an average absolute deviation from the experimental values of 0.019(1) Å for VMC and 0.007(2) Å for DMC. These averages correspond with ours in DMC, whereas our average deviation is significantly lower for VMC. In particular for O<sub>2</sub>, their VMC and DMC results both agree with ours, whereas their results are slightly worse for N<sub>2</sub> with a deviation from the experimental value by 0.010(1) Å for VMC and by 0.007(1) Å for DMC. Another very recently published Ref. [LU 2003] presents the bond length for N<sub>2</sub> calculated with a DMC method based on floating spherical Gaussians (different to our DMC method). Their result agrees very well with respect to the experimental value by 0.001(4) Å and with respect to our bond length by 0.005(5) Å.

To conclude this comparison, we find that our bond lengths calculated with VMC and DMC are comparable or even better compared to those by DFT and quantum chemical methods in their standard approaches. Also, we find that our results are in good agreement with reference values from two DMC studies within the statistical

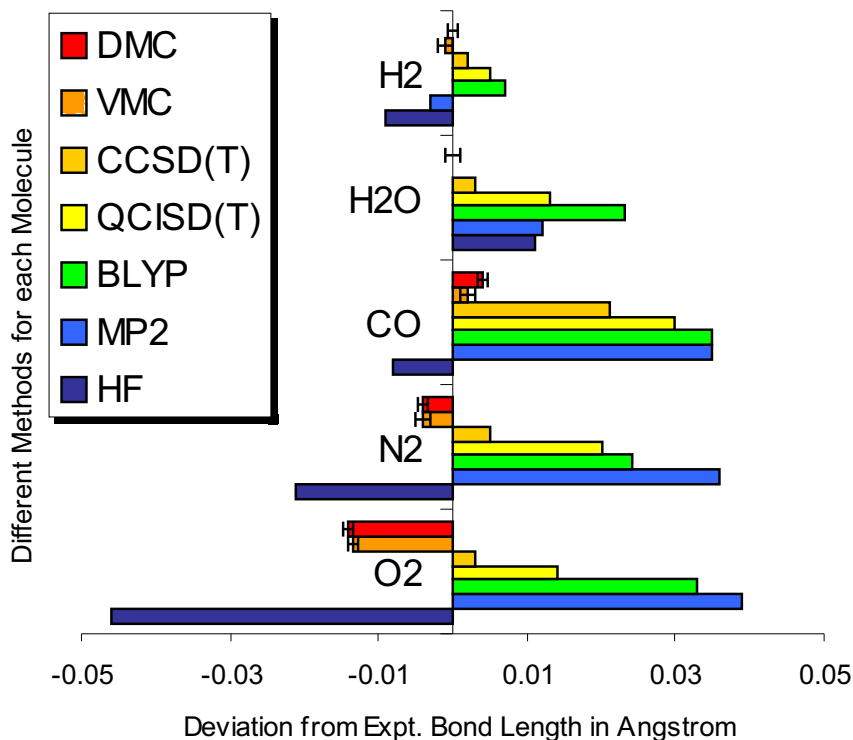


Figure 4.5: This figure compares the deviations of bond lengths from experimental values for our HF, VMC and DMC calculations with reference values by MP2, BLYP, CI and CC. All references are the same as in Table 4.7.

error bar.

## 4.3 Vibrational Frequencies

In Section 4.2, we determined the equilibrium geometries for five molecules. For the same molecules, we will also determine their internal vibrational frequencies.

### 4.3.1 Terminology

In molecular spectroscopy, vibrational frequencies of molecules are often given in the harmonic approximation. Similarly as for equilibrium geometries, other definitions exist for vibrational frequencies that account for excitation and anharmonic effects [HERZBERG 1979]. In this thesis, we follow this standard practice and calculate the harmonic vibrational frequencies,  $\omega_e$ , as eigenvalues from the dynamical matrix  $\mathbf{D}$  within the Born-Oppenheimer approximation (see Appendix A.1).



### 4.3.2 Technicalities - Treatment of Di- and Tri-Atomic Molecules

The harmonic vibrational frequencies are obtained from the potential energy curves calculated in Section 4.2. For di-atomic molecules, the vibrational frequencies are determined by

$$\omega_e = \sqrt{\frac{\kappa_e}{\mu}} \quad \text{and} \quad \kappa_e = \frac{d^2 E_0^{\text{BOS}}(r)}{dr^2} \Big|_{r_e}, \quad (4.5)$$

where  $\mu$  is the reduced mass,  $r$  the relative bond coordinate and  $r_e$  the bond length in equilibrium.

To determine the three vibrational frequencies for  $\text{H}_2\text{O}$ , the same model is used as in Section 4.2.1. Following Appendix A.1, we transform the six Cartesian coordinates<sup>12</sup>,  $\zeta_i$  (defined in Figure 4.3) into six mass-weighted coordinates,  $\eta_i = \xi_i \sqrt{m_i}$ , with  $i \in [1, \dots, 6]$  and  $\boldsymbol{\eta} := (\eta_1, \dots, \eta_6)$ . Furthermore, a matrix  $\mathbf{T}$  is constructed to fulfill the transformation  $\mathbf{S} = \mathbf{T}\boldsymbol{\eta}$ , with  $\mathbf{S} := (S_1, S_2, S_3)$ . The derived expression of  $\mathbf{T}$  is explicitly given in eq.(A.8). The dynamical matrix,  $\mathbf{D}$ , can then be written in terms of the force constant matrix,  $\mathbf{H}$ . Following eq.(A.6), the eigenvalues of  $\mathbf{D}$  are determined by the secular equation,

$$|\mathbf{D} - \omega_{i_e}^2 \hat{\mathbf{1}}| = |\mathbf{T}^t \mathbf{H} \mathbf{T} - \omega_{i_e}^2 \hat{\mathbf{1}}| = 0, \quad (4.6)$$

where  $\omega_{i_e}$  are the three vibrational frequencies with  $i = 1, 2, 3$  and  $\hat{\mathbf{1}}$  is the unity matrix.

To determine these three vibrational frequencies for  $\text{H}_2\text{O}$ , we first need to obtain the three force constants  $\kappa_{1e}$ ,  $\kappa_{2e}$  and  $\kappa_{3e}$  (with  $\kappa_{1e} = \kappa_{2e}$ ). This is done in analogy to expression (4.5). There, the energy curves for the bending and stretching modes are used from Section 4.2. After the force constants have been determined, the vibrational frequencies are then obtained by evaluating eq.(4.6).

The error bars of  $\omega_e$  are determined as for the bond length. Two curves with the largest possible difference in their vibrational frequencies are fitted within the error bars of the seven calculated total energies for each energy curve. The difference in the two vibrational frequencies gives one standard deviation of the mean.

### 4.3.3 Discussion

Table 4.8 shows the vibrational frequencies for HF, VMC and DMC. When looking at the DMC results, we find that all vibrational frequencies are within (or very close) to the statistical error with  $\text{O}_2$  being the exception. The best agreement with experiment is again found for the  $\text{H}_2$  molecule with  $-1(2) \text{ cm}^{-1}$ . The largest deviation is found for  $\text{O}_2$  with a deviation from experiment which is three times its statistical error bar of 27

<sup>12</sup> $\text{H}_2\text{O}$  has  $3N = 9$  Cartesian coordinates which reduce to six due to planar symmetry.

[in $\text{cm}^{-1}$ ]		$f_{\text{HF}}$	$f_{\text{VMC}}$	$f_{\text{DMC}}$	$\Delta f_{\text{HF}}$	$\Delta f_{\text{VMC}}$	$\Delta f_{\text{DMC}}$	$f_{\text{expt}}$
H <sub>2</sub>	D <sub><math>\infty h</math></sub>	4579	4459(69)	4415(2)	163	43(69)	-1(2)	4416
N <sub>2</sub>	D <sub><math>\infty h</math></sub>	2727	2460(104)	2400(38)	367	100(104)	40(38)	2360
O <sub>2</sub>	D <sub><math>\infty h</math></sub>	1972	1744(33)	1665(17)	392	164(33)	85(27)	1580
CO	C <sub><math>\infty v</math></sub>	2274	2277(88)	2225(49)	104	107(88)	55(49)	2170
H <sub>2</sub> O	A <sub>1</sub>	4145	-	3908(52)	313	-	76(52)	3832
	A <sub>1</sub>	1726	-	1691(56)	78	-	43(56)	1648
	B <sub>2</sub>	4205	-	3965(67)	262	-	22(67)	3943

Table 4.8: Frequencies are calculated with HF and the orbital re-optimized correlated sampling VMC and DMC method. The experimental reference values are taken from Ref. [HERZBERG 1979].

$\text{cm}^{-1}$ . This large deviation for O<sub>2</sub> corresponds with findings in Sections 4.1 and 4.2. For H<sub>2</sub>O, we find a better agreement with respect to the experimental value for the anti-symmetric stretching mode, 22(67)  $\text{cm}^{-1}$ , than for both symmetric bending and stretching modes, 43(56)  $\text{cm}^{-1}$  and 76(52)  $\text{cm}^{-1}$ . When comparing the DMC results with the once obtained by VMC, we find a systematic improvement by DMC for all molecules, i.e. by 42  $\text{cm}^{-1}$  (H<sub>2</sub>), by 60  $\text{cm}^{-1}$  (N<sub>2</sub>), by 79  $\text{cm}^{-1}$  (O<sub>2</sub>) and by 52  $\text{cm}^{-1}$  (CO).

As a first result, the obtained DMC vibrational frequencies agree with respect to the experimental value within (or very close to) their statistical errors with the exception for O<sub>2</sub>.

Another finding is that our best estimates for all VMC and DMC vibrational frequencies systematically overestimate the experimental value. Although this overestimation is statistically not significant except for O<sub>2</sub>, it should be noticed that the statistical error is about 2% for DMC and 4% for VMC. However, we will show in Section 5.8 that the best estimate of the vibrational frequency does not change more than a few  $\text{cm}^{-1}$  in the case of N<sub>2</sub> when increasing the evolution time. To interpret this overestimation in VMC and DMC, let us recall that the vibrational frequencies are already overestimated by HF on average by 240  $\text{cm}^{-1}$ . This suggests that subsequent VMC and DMC calculations (that are based on latter HF calculations) do not sufficiently describe the correlation effects that are necessary to yield the true vibrational frequencies. In particular for VMC, this shows that the  $\mathcal{J}$ -factor does not sufficiently compensate the missing correlation of a HF determinant. For DMC, this overestimation in the vibrational frequencies (in the curvature of the energy surface) suggests that the correlated sampling technique introduces a slight positive bias. And this bias appears to be larger for secondary geometries that are further away from the reference geometry.

To conclude, the used correlated sampling method yields DMC vibrational frequencies

[cm <sup>-1</sup> ]	$\Delta f_{\text{HF}}$	$\Delta f_{\text{DMC}}$	$\Delta f_{\text{HF(ref.)}}$	$\Delta f_{\text{BLYP}}$	$\Delta f_{\text{MP2}}$	$\Delta f_{\text{QCISD}}$	$\Delta f_{\text{CCSD(T)}}$	$f_{\text{expt}}$
H <sub>2</sub>	163	-1(2)	230/143	-43	117	-49	-6	4416
N <sub>2</sub>	367	40(38)	398/376	-23	-180	40	-19	2360
O <sub>2</sub>	392	85(27)	418/397	-62	-167	59	23	1580
CO	203	55(49)	269/233	-65	-45	6	-5	2170
H <sub>2</sub> O	313	76(52)	238/298	-264	-56	-81	9	3832
	78	43(56)	179/96	34	87	97	21	1648
	262	22(67)	246/295	-253	-25	-65	2	3943

Table 4.9: This table compares calculated HF and DMC deviations of the vibrational frequency from the experimental values with reference values by HF, BLYP, MP2, CISD(T) and CCSD(T). The first reference value for HF is taken from [POPLE 1992] (basis: 6-31G\*), while the second HF reference value from [NIST 2003] (basis: aug-cc-pVDZ). The CC reference values are taken from [NIST 2003] (basis 6-311G\*), and all other reference values from [POPLE 1992] (basis: 6-31G\*). The experimental values are taken from [HERZBERG 1979].

that agree with the experimental values within (or close to) their error bars of 20-80 cm<sup>-1</sup> or about 2% that we currently aim at. The only exception is found from O<sub>2</sub> similar as in Section 4.1 and 4.2. Also, correlated sampling DMC results systematically improve results from VMC calculations by about 50 cm<sup>-1</sup> for our molecules. Further systematic influences of our used correlated sampling technique on the vibrational frequency will be discussed in Section 5.8.

#### 4.3.4 Comparison with other Reference Methods

Table 4.9 presents our calculated HF and DMC vibrational frequencies and compares them with reference values by HF, BLYP, MP2, CISD(T) and CCSD(T). For our DMC vibrational frequencies, the average absolute deviation from the experimental values is 46(42) cm<sup>-1</sup>. Compared with DMC values, all reference methods show a larger average absolute deviations except for CCSD(T), i.e. for BLYP by 106 cm<sup>-1</sup>, for MP2 by 97 cm<sup>-1</sup> and for CISD(T) by 57 cm<sup>-1</sup>. For CCSD(T), the average deviation of 12 cm<sup>-1</sup> is about four times smaller than for DMC. This is also approximately true for each individual frequency. Finally, we compare our results for N<sub>2</sub> with the same reference DMC study [LU 2003] as in Section 4.2.4. This study presents a vibrational frequency which agrees within 11(38) cm<sup>-1</sup> with the experimental value and within 51(76) cm<sup>-1</sup> with ours.

To conclude the comparison for the vibrational frequencies, we find that our DMC results compare very well with reference values by quantum chemical and DFT methods. Only CCSD(T) reference values seem to be systematically improved compared to our DMC values. All other considered reference methods yield vibrational frequencies with a fluctuation in their results which makes them difficult to compare with our results.

However, the majority (and thus the average value) of their vibrational frequencies has a larger deviation from the experimental value as found for our DMC calculations.

## 4.4 Hydrogen Bonding and QMC

So far, this thesis was concerned with physical properties of molecules predominantly determined by covalent bonding. Thereby, we obtained bond strengths with typical values of several eV. Now, this section investigates hydrogen-bonds which have a strength that is more than one order of magnitude smaller. The H-bonding strength can range from 2 to 40 kcal/mol (0.9 to 1.7 eV) (in contrast, chemical bonds are usually larger than 50 kcal/mol or 2 eV). One commonly distinguishes these strengths in three classes: weak (<3 kcal/mol or 0.1 eV), normal (3-15 kcal/mol or 0.1-0.7 eV) and strong H-bonding (>15 kcal/mol or 0.7 eV) [JEFFREY 1994].<sup>13</sup>

In this thesis, we will examine the H-bond strength and their influence on the proton transfer reaction barriers for two small molecular systems, di-ammonia and malonaldehyde. We chose malonaldehyde since it is considered as a prototype of strong intra-molecular H-bonded systems. Some experimental data and a fair amount of theoretical work are available [BARONE 1996]. Unlike malonaldehyde, di-ammonia is governed by a weak hydrogen bond and is investigated as theoretical benchmark system in some earlier studies [NOVOA 1995]<sup>14</sup>. Here, we will investigate two different equilibrium geometries for di-ammonia that are obtained by two DFT methods [ISMER 2002].

QMC methods promise to be very suitable when describing H-bonding energetics. This will become evident when recalling the underlying interactions of these bonds. We begin by briefly introducing H-bonds and subsequently discuss the proton transfer process.

### 4.4.1 Hydrogen Bonding

H-bonds describe attractive interactions between a proton, covalently bonded to a donor-atom X, and a proton acceptor Y,



where X and Y are electronegative atoms such as O, N or S. Thereby, the proton donor and acceptor can be in the same molecule (like in malonaldehyde) or in different

---

<sup>13</sup>When discussing H-bonding, it is common practice to use kcal/mol. For consistency reason however, we additionally specify the eV value.

<sup>14</sup>Talking about ammonium and working at the Fritz-Haber Institut, I am delighted to remark that Fritz Haber (1868-1934) got the Nobel Prize in Chemistry in 1918 for the development of the procedure of synthetic ammonium production, known as Haber-Bosch-Method today, see also <http://www.nobel.se/chemistry/laureates/1918/index.html>.

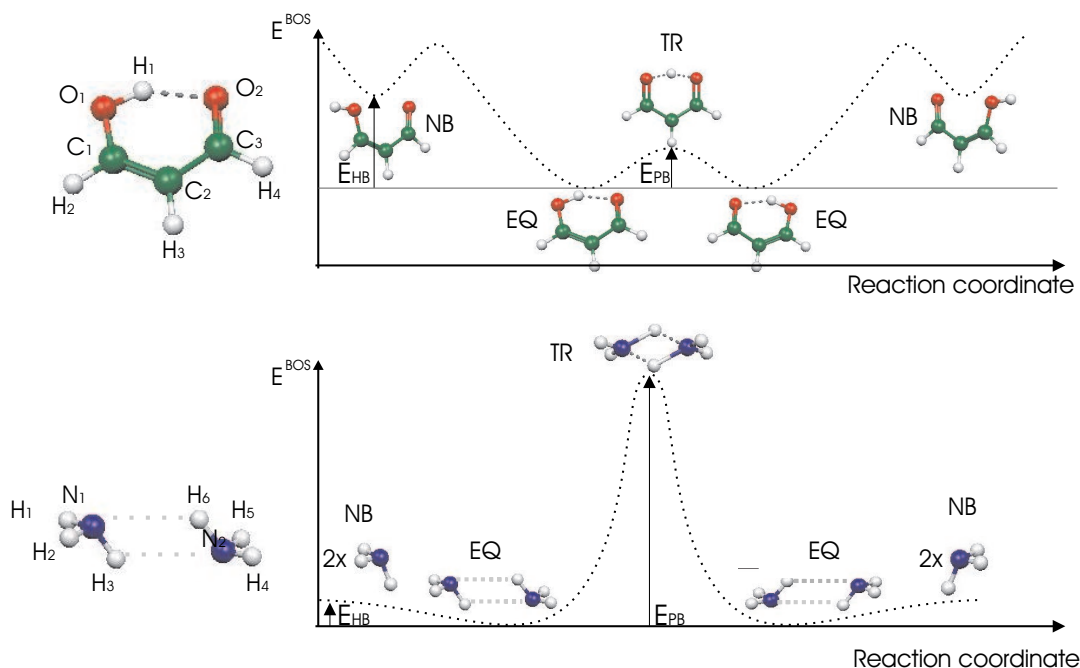


Figure 4.6: The upper and lower graph schematically show the Born-Oppenheimer Surface for malonaldehyde and di-ammonia, respectively. In particular, one sees three local extrema which belong to the non-bonded (NB), equilibrium (EQ) and transitional (TR) structure described in the text. The H-bonding energy  $E_{HB}$  and the proton barrier  $E_{TR}$  are both indicated.

molecules (like in di-ammonia). In the literature, there is a controversy about the exact nature of H-bonding due to their very different strengths. A common description of the nature of H-bonds is given by an electrostatic and induced electrodynamic (van der Waals) interaction [HADZI 1997]. In addition, a covalent contribution has been suggested based on a calculated charge transfer between the acceptor Y and donor X and ranges from 0.01 to 0.03 electrons depending on the H-bonding [SCHEINER 1997]. This charge transfer would then imply a hybridization or a covalent contribution to the H-bonding. Yet in an exclusive electrostatic and van der Waals description, charge transfer can be understood as a static polarization of the electron clouds in the X-H and Y fragments [HADZI 1997]. In the following, let us consider H-bonds in terms of electrostatic and van der Waals interactions.

(1) **The electrostatic interaction** arises from the electronegativity which shifts a fraction  $\delta$  of an electron from the hydrogen H to the proton donor X as indicated in

expression (4.7). This results in a dipole that in turn interacts electrostatically with an electron pair of Y (dipole-dipole interaction).

**(2) Van der Waals interaction**<sup>15</sup> arises from fluctuations in the electron distribution of one molecule. This fluctuation dynamically polarizes the charge distribution of another neighboring molecule and results in an attraction between the two molecules. These fluctuations, specifically the average response to these fluctuations, are exactly described by the true wavefunction and contribute to the dynamic correlation introduced in Section 2.5. Hence, DMC should be suitable in principle to describe these induced electrodynamic interactions which are estimated to contribute about or less than 2 kcal/mol (or 0.05 eV) to the H-bonding energy [SCHEINER 1997].

To calculate H-bond energies for both of our molecules, we introduce the non-bonding (NB) and the equilibrium (EQ) geometry for each molecule as shown in Figure 4.6. The NB geometry is arranged in the way that no H-bridge exists, and it is optimized to yield a local minimum in the Born-Oppenheimer surface. The EQ geometry is optimized to yield a global minimum in the Born-Oppenheimer surface in the presence of an H-bond. Consequently, the H-bonding energy,  $E_{HB}$ , for both molecules is given by

$$E_{HB} = E_0^{BOS}(NB) - E_0^{BOS}(EQ), \quad (4.8)$$

when calculating the electronic ground state energies,  $E_0^{BOS}$ , at the NB and EQ geometry.

#### 4.4.2 Energy Barriers in the Proton Transfer

“The proton transport from one atom to another has been defined as the most general and important reaction in chemistry” [BARONE 1996]. It plays an important role in a multitude of processes such as acid-base neutralization or enzymatic reactions. Two aspects are relevant for the proton transfer. (1) The first aspect is the proton (hydrogen) motion on the Born-Oppenheimer surface from the first equilibrium position, EQ, across a transition (saddle) point, TR, to a neighboring, EQ, position as shown in Figure 4.6. Thereby, the TR geometry is defined as the local maximum of the curve connecting the two EQ positions on the Born-Oppenheimer surface (i.e. the TR point leads to the lowest potential energy barrier along this connection curve). Generally, this first aspect strongly depends on the hydrogen bridge strength and the inter-atomic distances. (2) The second aspect is the rearrangement of the electron system that occurs during the proton transfer. In turn, this determines a geometric rearrangement of the “backbone” in the case of malonaldehyde (see for example Ref. [ISMER 2002]). Consequently, the proton barrier,  $E_{PB}$ , for both molecules is given by

---

<sup>15</sup>The van der Waals interaction, as discovered by London in 1930, is also known as London force, dispersion force or induced electrodynamic interaction.

$\mathcal{J}$ Geo- metry			$E_{\text{tot}}^{\text{HF}}$ [in Ha]	$E_{\text{tot}}^{\text{VMC}}$ [in Ha]	$E_{\text{corr}}^{\text{VMC}}$ [in Ha]	$E_{\text{tot}}^{\text{DMC}}$ [in Ha]	$E_{\text{corr}}^{\text{DMC}}$ [in Ha]
Malonaldehyde							
NB	553	PBE-LDA	-50.3114	-51.2536(16)	-0.9422(16)	-51.3815(6)	-1.0701(6)
EQ	553	PBE-LDA	-50.3279	-51.2614(17)	-0.9335(17)	-51.3995(8)	-1.0716(8)
TR	553	PBE-LDA	-50.3134	-51.2582(17)	-0.9448(17)	-51.3923(7)	-1.0789(7)
Di-Ammonia							
NB	550	PBE	-22.9180	-23.3922(20)	-0.4742(20)	-23.4738(4)	-0.5558(4)
	553	PBE	-22.9180	-23.4256(16)	-0.5076(16)	-23.4748(6)	-0.5568(6)
	550	PBE-LDA	-22.9187	-23.3846(20)	-0.4659(20)	-23.4750(6)	-0.5563(6)
	553	PBE-LDA	-22.9187	-23.4256(16)	-0.5069(16)	-23.4764(6)	-0.5577(6)
EQ	550	PBE	-22.9219	-23.4058(14)	-0.4839(14)	-23.4809(6)	-0.5593(6)
	553	PBE	-22.9219	-23.4231(12)	-0.5012(12)	-23.4810(5)	-0.5591(5)
	550	PBE-LDA	-22.9232	-23.4000(15)	-0.4768(15)	-23.4788(4)	-0.5556(4)
	553	PBE-LDA	-22.9232	-23.4253(12)	-0.5021(12)	-23.4804(5)	-0.5572(5)
TR	550	PBE	-22.8010	-23.2993(16)	-0.4983(16)	-23.3801(6)	-0.5791(6)
	553	PBE	-22.8010	-23.3120(14)	-0.5110(14)	-23.3815(4)	-0.5805(4)
	550	PBE-LDA	-22.8007	-23.3010(17)	-0.5003(17)	-23.3808(4)	-0.5801(4)
	553	PBE-LDA	-22.8007	-23.3160(14)	-0.5153(14)	-23.3825(5)	-0.5818(5)

Table 4.10: This table lists the total and correlation energies for malonaldehyde (MA) and di-ammonia (DA) for a pseudopotential HF, VMC and DMC calculation. For both systems, the total energy is evaluated at the non-bonding (NB), equilibrium (EQ) and transition (TR) geometry as represented in figure 4.6. All geometries indicated in column three are previously obtained within DFT PBE-LDA and PBE [ISMER 2002]. Column two indicates the Jastrow factor used.

$$E_{\text{PB}} = E_0^{\text{BOS}}(\text{TR}) - E_0^{\text{BOS}}(\text{EQ}), \quad (4.9)$$

when calculating the electronic ground state energies,  $E_0^{\text{BOS}}$ , at the TR and EQ geometry.

#### 4.4.3 Technicalities

The used trial wavefunctions are again based on CF basis sets and pseudopotentials with a  $\mathcal{J}(550)$  Jastrow factor. For di-ammonia, we additionally perform calculations with  $\mathcal{J}(550)$ . The VMC calculations for malonaldehyde and di-ammonia are performed with 600,000 walkers (in blocks of 20 walkers). For the Jastrow factor optimization, we use 4,000 walkers and perform five optimization cycles. The DMC calculations for malonaldehyde and di-ammonia have a population of 50 walkers and consist of

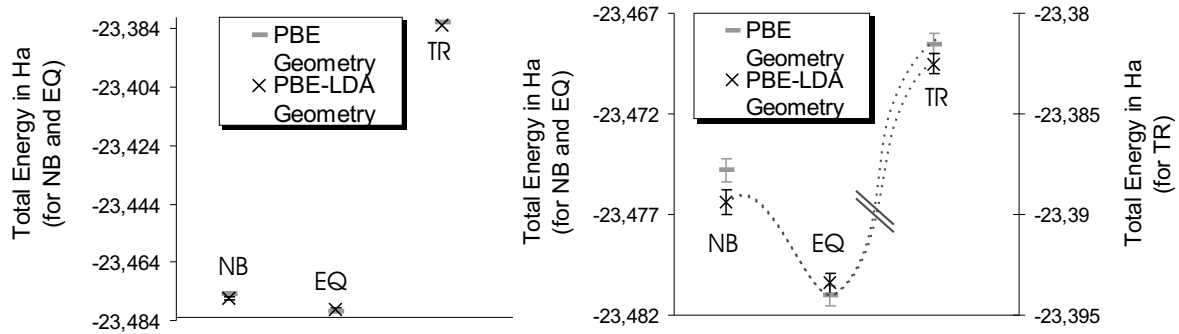


Figure 4.7: These figures show the calculated DMC total energy at the non-bonding (NB), equilibrium (EQ) and transition (TR) structures for di-ammonia. The left figure uses one energy scale, whereas the right one uses two scales for better illustration (the left ordinate belongs to the NB and EQ structures, the right one to the TR structure). The used DFT PBE structures are labeled with black circles and the DFT PBE-LDA optimized structure with gray circles. All values refer to the same Jastrow factor  $\mathcal{J}(553)$ .

160,000 and 100,000 diffusion steps, respectively. The two used geometries, previously obtained with DFT for the different functionals PBE-LDA and PBE, are taken from Ref. [ISMER 2002].

#### 4.4.4 Results and Discussion

Table 4.10 shows the total and correlation energies for malonaldehyde and di-ammonia calculated with HF, VMC and DMC at the introduced non-binding (NB), equilibrium (EQ) and transition (TR) geometries.

We begin our discussion by considering the influence of the Jastrow factor on the DMC total energy for di-ammonia. For all three geometries, we find an insignificant improvement of about 0.03-0.05 eV (1-2 mHa) when comparing the DMC total energies for the two Jastrow factors,  $\mathcal{J}(553)$  and  $\mathcal{J}(550)$ . As of this improvement, we will limit the following discussion to values for the larger Jastrow factor.

The role of different structures will now be discussed for di-ammonia based on Table 4.10. Thereby, we consider the DMC total energies calculated for the NB, EQ and TR geometries optimized by DFT PBE-LDA and PBE. There, we find that the PBE-LDA geometries yield about 0.03 eV (1mHa) lower DMC energies for the NB and TR geometry as for the PBE geometry. This is different for the EQ geometry. There, we find that the PBE structure yields a DMC energy that is lower by about 0.03-0.05 eV (1-2 mHa) as for the PBE-LDA structure. Figure 4.7 illustrates these differences between the PBE-LDA and PBE structures for all three geometries.



[in kcal/mol]	Malonaldehyde		Di-Ammonia		
	$E_{\text{HB}}$	$E_{\text{PB}}$	$E_{\text{HB}}$	$E_{\text{PB,min}}$	$E_{\text{PB,max}}$
HF	0.45	0.39	0.09	3.29	3.30
VMC	0.22(9)	0.09(9)	0.07(7)	2.91(7)	3.02(7)
DMC	0.49(3)	0.20(4)	0.13(3)	2.68(3)	2.71(3)

Table 4.11: This table shows the H-bonding energy  $E_{\text{HB}}$  and the proton barrier  $E_{\text{PB}}$  for malonaldehyde and di-ammonia. Taking the total HF, VMC and DMC energies from table 4.10,  $E_{\text{HB}}$  and  $E_{\text{PB}}$  are then obtained from formulas (4.9) and (4.8). For both molecules, the most appropriate (available) geometry has been chosen as discussed in the text: for di-ammonia, we use the optimized geometries denoted as arguments of the structures: NB (PBE-LDA), EQ (LDA) and TR(PBE-LDA or PBE); for malonaldehyde, only PBE-LDA optimized geometries are used. For all energies, the Jastrow factor  $\mathcal{J}(553)$  has been chosen.

Thanks to the variational principle for the NB and EQ geometries, the lowest total energy gives the best prediction of the true value. This is different for the TR geometry. There, the Born-Oppenheimer surface is a saddle point<sup>16</sup> where the variational principle does not hold any more. Hence, we can not tell which structure is closer to the true one based on the calculated total energies. Therefore, the best prediction of the total energy for the TR geometry is the range of 0.03 eV (1 mHa) between the upper and the lower energy. Figure 4.7 illustrates these results with a dotted line: this line indicates the lowest DMC energies at the NB and EQ geometries and the different DMC energies for the PBE and PBE-LDA structures at the TR geometry.

Let us summarize our results about the different structures. Our finding in the total energies suggest that PBE-LDA are better for the NB geometry whereas the PBE structure are better for the EQ geometry. These findings give an indication when investigating the appropriateness of the PBE-LDA and PBE functionals in DFT (see also next section ).

Under consideration of the previous discussion, our best estimate for the H-bonding energy,  $E_{\text{HB}}$ , and the proton barrier,  $E_{\text{PB}}$ , are calculated and listed in Table 4.11. Since available experimental data have a large uncertainty, we instead compare our results with elaborate CC reference calculations. This comparison, however, will be postponed to the next section. For now, we will just state the “disappointing” finding that the VMC H-bond energies appear to be lower than the HF values for both molecules. In contrast, DMC (and CC calculations) yields values that are larger than by HF. This shows that the inclusion of correlation by the Jastrow factor within VMC does not necessarily improve the HF value for the H-bonding energy. And this shows again the need for a subsequent and more accurate DMC calculation.

<sup>16</sup>In both Figures 4.6 and 4.7, the Born-Oppenheimer surface shows a maximum at the TR point in 1 dimension. However, for di-ammonia, the 18 dimensional Born-Oppenheimer surface has a saddle point at the TR geometry.

[in eV]	$\mathcal{J}$	$E_{\text{HB}}^{\text{HF}}$	$E_{\text{HB}}^{\text{VMC}}$	$E_{\text{HB}}^{\text{DMC}}$	$E_{\text{PB}}^{\text{HF}}$	$E_{\text{PB}}^{\text{VMC}}$	$E_{\text{PB}}^{\text{DMC}}$
PBE	550	0.19	0.37(7)	0.20(2)	3.29	2.90(8)	2.75(3)
	553	-	0.07(5)	0.17(2)	-	3.02(7)	2.70(2)
PBE-LDA	550	0.12	0.42(7)	0.10(2)	3.33	2.69(8)	2.67(2)
	553	-	0.01(5)	0.11(2)	-	2.97(7)	2.66(3)

Table 4.12: This table shows the H-bond energy,  $E_{\text{HB}}$ , and the proton barrier,  $E_{\text{PB}}$ , for di-ammonia calculated with HF, VMC and DMC. The first two lines give  $E_{\text{HB}}$  and  $E_{\text{PB}}$  for the DFT PBE geometry calculated with two Jastrow factors  $\mathcal{J}(550)$  and  $\mathcal{J}(553)$ . The last two lines show the same for the DFT PBE-LDA geometry.

Before comparing our results with reference values, a last finding is obtained when examining the DMC correlation energies in Table 4.10. For both molecules, we find that the correlation energy of the TR geometry is about 0.68 eV (25 mHa) lower for di-ammonia, and 0.19 eV (7 mHa) lower for malonaldehyde, than for corresponding EQ and NB geometries<sup>17</sup>. From these increased values, we can infer that electron correlations are particularly important for the TR geometry. Another finding is that HF yields already H-bond energies in agreement with our DMC results, whereas the proton barrier is significantly overestimated by HF compared to DMC. To conclude, correlation effects are an important aspect in the intra/inter-molecular proton transport process.

#### 4.4.5 Comparison with other Quantum Chemical Methods

Table 4.13 compares the DMC proton barriers,  $E_{\text{PB}}$ , and H-bonding energies,  $E_{\text{HB}}$ , for both molecules with values obtained by DFT, CC and MP2 calculations.<sup>18</sup>

When looking at **di-ammonia** first, our best calculated H-bonding energy of 0.13(3) eV agrees with the CC value of 0.13 eV. The DFT PBE or PBE-LDA methods both underestimate  $E_{\text{HB}}$  by 0.02 eV or 10% (PBE) and by 0.04 eV or 31% (PBE-LDA) with respect to the DMC value. In the same comparison, B3LYP over- or underestimates  $E_{\text{HB}}$  by 0.03 eV depending on the basis set chosen, and MP2 shows similar basis set dependencies as B3LYP. For the di-ammonia proton barrier,  $E_{\text{PB}}$ , no values in the literature are found, except the two obtained by DFT PBE/PBE-LDA. Compared to our DMC values, PBE barriers underestimate the DMC values by 0.61 eV or 23% and PBE-LDA barriers underestimate the DMC values by 0.2 eV or 8%.

When looking at **malonaldehyde**, similar observations hold for the calculated proton barrier,  $E_{\text{PB}}$ . Our DMC value of 0.20(4) eV is in agreement with the CC value of

<sup>17</sup>For clarity, a lower correlation energy has a larger absolute value.

<sup>18</sup>While experimental values exist for these values [TSUZUKI 2001], their error bar is of several kcal/mol which precludes a meaningful comparison with theoretical data.

0.18 eV. Also, all three DFT methods underestimate the DMC value for the proton barrier by about 0.17 eV (PBE), 0.07 eV (PBE-LDA) and 0.11 eV (B3LYP) or by 85% (PBE), 35% (PBE-LDA) and 55% (B3LYP). However, when considering the H-bond energy,  $E_{\text{HB}}$ , the DMC value is in less good agreement with the CC one and is 0.15(3) eV lower. This disagreement might be explained on the one hand by the influence of the chosen PBE-LDA structure at the EQ geometry. (For di-ammonia, we showed earlier an influence of 0.03 - 0.06 eV when choosing different structures at the EQ geometry). On the other hand, also the CC reference value could be too high as a result of an insufficient basis set. To further investigate this slight difference, one could try different geometries which may be obtained e.g. by the correlated sampling technique introduced in Section 3.5. But this is beyond the scope of this thesis.

To conclude, our DMC H-bond energies and proton barriers agree with CC calculations where available and show a deviation of less than 0 - 0.02(4) eV, except in the H-bond energy for malonaldehyde. In particular, we have examined reference values for proton barriers by DFT. For malonaldehyde, we confirm their significant underestimation by about 0.07-0.11 eV or 35-85% with respect to DMC values. For the weakly H-bonded di-ammonia, we find that DFT barriers are about 0.2-0.61 eV or 8-23% lower with respect to our DMC results. Thereby, we set a benchmark calculation since no alternative quantum chemical studies are found in the literature. Finally, we have shown that the PBE functional yields better equilibrium structures for di-ammonia than the PBE-LDA functional.

[in eV]	basis	$E_{\text{HB}}$	$E_{\text{PB}}$
Malonaldehyde			
DMC	CF	0.49(3)	0.20(4)
HF	CF	0.45	0.39
HF	6-31G/6-311G(2d,2p)	-/0.54	0.39/0.38
PBE	plane waves	0.65	0.03
PBE-LDA	plane waves	0.52	0.13
B3LYP	DZP	0.65	0.09
CCSD(T)	DZP	0.64	0.18
MP2	6-311G(2d,2p)	0.61	0.16
Di-Ammonia			
DMC	CF	0.13(3)	2.68(3) - 2.71(3)
HF	CF	0.09	3.29 - 3.30
HF	cc-pVDZ/cc-pVTZ	0.14*/0.08*	-
PBE	plane waves	0.11	2.07
PBE-LDA	plane waves	0.09	2.48
B3LYP	cc-pVDZ/pVTZ	0.19*/0.10*	-
CCSD(T)	cc-pVTZ	0.127**	-
MP2	cc-pVDZ/pV5Z/	0.08**/0.13**	-

Table 4.13: This table compares the DMC H-bonding energies  $E_{\text{HB}}$  and the proton barriers  $E_{\text{PB}}$  for malonaldehyde and di-ammonia with reference energies obtained with three different DFT methods, CC and MP2. The calculated DMC values are taken from table 4.11. All DFT PBE/PBE-LDA reference energies are taken from [ISMER 2002] where geometries are optimized within each method. For malonaldehyde, all other reference energies are taken from [BARONE 1996] where geometries are optimized with B3LYP. For di-ammonia, all energies labeled with \* are taken from [NOVOA 1995] where geometries are optimized with BLYP/6-31++G(2d,2p); energies with \*\* are from [TSUZUKI 2001] where geometries are optimized with MP2/6-311G\*\*.

# Chapter 5

## Methodological Investigations

In the last chapter, we have investigated the applicability of the VMC and DMC methods in calculating physical properties of molecules. Among all investigated molecules, we found that our DMC binding energy for  $\text{N}_2$  had the largest deviation of 17 mHa (0.47 eV or 4.7%)<sup>1</sup> from the experimental value. There exist two DMC reference values in literature which show a deviations of 6 mHa from the experimental value [GROSSMAN 2002, MITAS 1994]. In this section, we examine reasons for this difference and discuss possible improvements in our calculations. In particular, we analyze the role of different approximations within our VMC and DMC methods and investigate the results obtained upon the use of different Jastrow factors, basis sets, pseudopotentials and multi-determinant trial wavefunctions. In addition, we will examine computational parameters which are specific to DMC, i.e. the role of the time step in the diffusion process, the total number of diffusion steps (diffusion time), the population size and the numerical integration method when evaluating the non-local pseudopotential components. We will end this chapter by discussing some methodological dependencies found within the correlated sampling method when determining inter-atomic forces.

### 5.1 Jastrow Factor

In this section, we investigate the dependence of the VMC and DMC results when increasing the degree of the polynomials in our  $\mathcal{J}$ -factor. This corresponds to a successive increase the number of  $\mathcal{J}$ -parameters (see Section 3.2.2) from 3 to 24, while the same HF Slater determinant is used. For all calculations, we use the CF basis and pseudopotential, the time step  $\delta\tau = 0.1 \text{ Ha}^{-1}$  and other input parameters as in Section 4.1.

---

<sup>1</sup>In the last chapter, we have used eV as a typical unit for binding energies. When discussing methodological investigations throughout this chapter, we will consistently use Ha.

$\mathcal{J}$		$E_{\text{VMC}}^{\text{tot}}$	$E_{\text{VMC}}^{\text{corr}}$	$\sigma_{\text{VMC}}$	$\tau_{\text{corr}}$	$E_{\text{DMC}}^{\text{tot}}$	$E_{\text{DMC}}^{\text{corr}}$	$\sigma_{\text{DMC}}$	$\tau_{\text{corr}}$
	#	[in Ha]	[in Ha]	[in Ha]	[Ha <sup>-1</sup> ]	[in Ha]	[in Ha]	[in Ha]	[Ha <sup>-1</sup> ]
220	3	-9.7475(5)	-0.0997(5)	0.346	1.21	-9.7695(8)	-0.1217(8)	0.346	3.29
330	5	-9.7549(4)	-0.1071(4)	0.313	1.19	-9.7690(6)	-0.1212(6)	0.322	3.24
440	7	-9.7553(4)	-0.1075(4)	0.318	1.17	-9.7699(7)	-0.1221(7)	0.327	3.13
550	9	-9.7563(4)	-0.1085(4)	0.315	1.16	-9.7697(6)	-0.1219(6)	0.325	3.21
553	11	-9.7589(4)	-0.1111(4)	0.291	1.17	-9.7694(5)	-0.1216(5)	0.290	2.98
554	16	-9.7593(4)	-0.1115(4)	0.288	1.16	-9.7694(5)	-0.1216(5)	0.288	2.93
555	24	-9.7616(4)	-0.1138(4)	0.284	1.14	-9.7700(5)	-0.1222(5)	0.284	2.81
025*	24	-9.7610(4)	-0.1132(4)	0.273	1.11	-9.7697(3)	-0.1219(3)	0.284	2.61

Table 5.1: For the N-atom, this table lists the VMC and DMC total and correlation energies, the standard deviations of the local energies, and the correlation time calculated for different Jastrow factors,  $\mathcal{J}$  (i.e. for different numbers of parameters). For all calculations, we use to Jastrow factor with independent parameters,  $a_{\alpha n}$ ,  $b_n$  and  $c_{\alpha n}$ , (ipot=4 in our code) except for the calculation in the last row. That Jastrow factor,  $\mathcal{J}(025^*)$  (ipot=3 in our code), is allowed to have dependent  $a_{\alpha n}$ ,  $b_n$  and  $c_{\alpha n}$  parameters (note that  $\mathcal{J}(025^*)$  has no  $a_{\alpha n}$ , one  $b_n$  and only  $c_{\alpha n}$  parameters but has the same number of parameters as  $\mathcal{J}(555)$  (for the used notation, see Section 3.2.2). For all VMC and DMC calculations, we choose the CF pseudopotential and basis, the time step,  $\delta\tau = 0.1 \text{ Ha}^{-1}$ , a fixed scaling factor  $\kappa = 0.8$  and other input parameters as in Section 4.1.

$\mathcal{J}$		$E_{\text{VMC}}^{\text{tot}}$	$E_{\text{VMC}}^{\text{corr}}$	$\sigma_{\text{VMC}}$	$\tau_{\text{corr}}$	$E_{\text{DMC}}^{\text{tot}}$	$E_{\text{DMC}}^{\text{corr}}$	$\sigma_{\text{DMC}}$	$\tau_{\text{corr}}$
		[in Ha]	[in Ha]	[in Ha]	[Ha <sup>-1</sup> ]	[in Ha]	[in Ha]	[in Ha]	[Ha <sup>-1</sup> ]
220		-19.8046(13)	-0.3295(13)	0.73	1.90	-19.8845(3)	-0.4094(3)	0.74	3.43
330		-19.8174(11)	-0.3423(11)	0.66	1.84	-19.8840(3)	-0.4089(3)	0.68	3.45
440		-19.8244(11)	-0.3493(11)	0.64	1.81	-19.8843(4)	-0.4092(4)	0.69	3.29
550		-19.8314(11)	-0.3563(11)	0.64	1.82	-19.8854(3)	-0.4103(3)	0.68	3.28
553		-19.8390(9)	-0.3639(9)	0.55	1.61	-19.8853(2)	-0.4102(2)	0.59	3.24
554		-19.8441(11)	-0.3690(11)	0.55	1.56	-19.8852(3)	-0.4101(3)	0.58	3.13
555		-19.8464(9)	-0.3713(9)	0.55	1.52	-19.8855(3)	-0.4104(3)	0.57	3.10
025*		-19.8499(9)	-0.3748(9)	0.54	1.48	-19.8856(2)	-0.4105(2)	0.57	3.09

Table 5.2: This table gives the same information as the previous Table 5.1 but for the N<sub>2</sub>-molecule, instead.

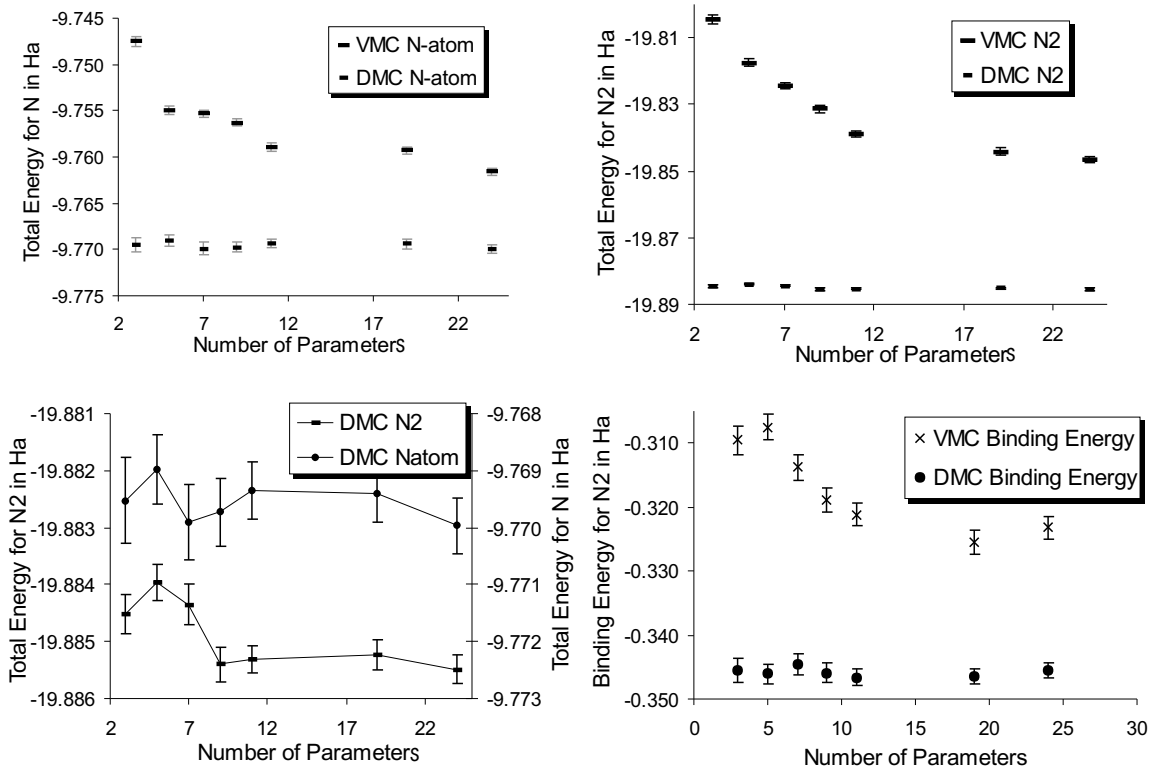


Figure 5.1: The upper two diagrams show the VMC and DMC total energy of the N-atom (left hand side) and the N<sub>2</sub>-molecule (right hand side) for different Jastrow factors (and respective numbers of parameters). The two lower diagrams show the DMC total energies for N and N<sub>2</sub> on a smaller scale (left hand side) and the VMC and DMC binding energy for N<sub>2</sub> (right hand side). All values are taken from Table 5.2 and 5.1.

For N and N<sub>2</sub>, Table 5.1 and 5.2 present the calculated VMC and DMC total and correlation energies, the standard deviations of the local energies and the correlation time. The respective binding energies<sup>2</sup> are plotted in Figure 5.1.

When increasing the number of  $\mathcal{J}$ -parameters successively from 3 to 24, we find that the VMC total energy decreases monotonically by 14(1) mHa for N and by 42(1) mHa for N<sub>2</sub>. In contrast, the DMC total energy does not change significantly. These changes in DMC are within one standard error (N-atom) or close to one standard error of 1 mHa (N<sub>2</sub>-molecule). Nevertheless, for the N<sub>2</sub>-molecule, one could assume a slight improvement in these DMC total energies for larger  $\mathcal{J}$ -factors by about 1 mHa. But these improvements are not larger than two standard errors and are therefore again

<sup>2</sup>In Chapter 4, the zero point energy was included in all discussed binding energies. Throughout Chapter 5, the zero point energy will be omitted to simplify the discussion.

not significant. We furthermore find the reduction of the standard deviation of the local energy for N by a factor of 0.8 in VMC and DMC, and for N<sub>2</sub> by a factor of 0.7 (VMC) and 0.8 (DMC) for the improved  $\mathcal{J}$ -factor.

As a first summary, we find a significant decrease in the VMC total energy and in the variances when increasing the number of  $\mathcal{J}$ -parameters. This implies an improvement in the quality of  $\Psi_T$ . At the same time, we find that the DMC total energy is fairly independent and does not significantly change when increasing the number of  $\mathcal{J}$ -parameters. This behavior is also illustrated in the two upper and the one lower left diagram of Figure 5.1.

Similar results are found when looking at the binding energies that are presented in the lower right diagram of Figure 5.1. There, we see that larger  $\mathcal{J}$ -factor has no significant influence on the DMC binding energy as well. This is different for VMC, there we find a general decrease in the binding energy by more than 10 mHa when increasing the number of  $\mathcal{J}$ -parameters. Thanks to the variational character in VMC, this implies that the N<sub>2</sub>-molecule is relatively (to the N-atom) better described by  $\Psi_T$  for larger  $\mathcal{J}$ -factors than it is for smaller  $\mathcal{J}$ -factors.

A similar observation can be made for di-ammonia in the last section, i.e. in Table 4.10. When using the  $\mathcal{J}(553)$ -factor with eleven instead of the  $\mathcal{J}(550)$ -factor with nine parameters, the VMC total energy decreases by several tens of mHa for different geometries. Whereas the DMC total energy did not change by more than a standard error of 1 mHa.

As a conclusion from our investigations for different  $\mathcal{J}$ -factors, we find that the number of  $\mathcal{J}$ -parameters is rather important for the VMC total energy and for respective binding energies. Not so for DMC calculations, there the influence of the number of  $\mathcal{J}$ -parameters has no significant influence much larger than the standard errors we currently aim at, for both, the total and binding energy.<sup>3</sup>

## 5.2 The Basis Set

So far, we used the “minimal” CF basis set of *3s3p1d* Gauss type orbitals (GTOs) as listed in Table B.3 in the appendix. This minimal basis set consists of 36 basis functions for N<sub>2</sub> and allows for the lowest computational costs. In this section, we examine the VMC and DMC total energies when using two larger basis sets in which the one-particle orbitals of the HF Slater determinant are expanded. Also, by using the results of the last section, we will limit this investigation to the  $\mathcal{J}(553)$ -factor.<sup>4</sup>

<sup>3</sup>We have tested the influence of the  $\mathcal{J}$ -factor also for most other calculations in this thesis. But the results have been omitted in the previous discussion, since we have found the same stated conclusion.

<sup>4</sup>All calculations in this section are additionally performed for the  $\mathcal{J}(550)$ -factor showing no significant difference in agreement with Section 5.1.



Basis	$E_{\text{HF}}^{\text{tot}}$	$E_{\text{VMC}}^{\text{tot}}$	$\sigma_{\text{VMC}}$	$E_{\text{VMC}}^{\text{corr}}$	$E_{\text{DMC}}^{\text{tot}}$	$E_{\text{DMC}}^{\text{corr}}$
N						
CF	-9.6478	-9.7584(4)	0.30	-0.1106(4)	-9.7692(1)	-0.1214(1)
CF+	-9.6487	-9.7607(3)	0.28	-0.1120(3)	-9.7697(1)	-0.1210(1)
cc-pCVQZ	-9.6482	-9.7569(7)	0.39	-0.1087(7)	-9.7721(2)	-0.1239(2)
N <sub>2</sub>						
CF	-19.4751	-19.840(1)	0.55	-0.364(1)	-19.8853(2)	-0.4102(2)
CF+	-19.4846	-19.843(1)	0.55	-0.358(1)	-19.8867(2)	-0.4021(2)
cc-pCVQZ	-19.4847	-19.841(1)	0.67	-0.356(1)	-19.8947(3)	-0.4100(3)

Table 5.3: This table shows the HF, VMC and DMC total and correlation energies, and the standard deviation of the local energies for the three different basis sets, CF, CF+ and cc-pCVQZ. For all VMC and DMC calculations, we use the CF pseudopotential,  $\mathcal{J}(553)$ ,  $\delta\tau = 0.1 \text{ Ha}^{-1}$  and other input parameters as in Section 4.1.

### 5.2.1 Selection and Construction of the HF Basis Set

The two new basis sets are selected as follows. The first one, CF+, is obtained by partly un-contracting the CF basis and increasing the variational flexibility in the HF calculation. In more detail, the eight primitive s- and p- GTOs are split into two contracted GTOs with three (primitive) GTOs and into one contracted GTO with two (primitive) GTOs. This results in  $5s5p1d$  GTOs with 52 basis functions for N<sub>2</sub>. To select the second basis, we first calculated the HF total energies for a range of available HF basis sets taken from Ref.[GAUSSIAN 2003] (Table B.2 in the appendix lists these HF total energies). Then we select the basis with the lowest HF energy for N<sub>2</sub>. In our selection, we have to restrict our final choice to basis sets without f- and higher orbitals which our QMC code can presently not handle. The selected basis, cc-pCVQZ, has  $8s7p5d$  GTOs with 118 basis functions for N<sub>2</sub>.

For both new basis sets, the HF total energy leads to a decrease for N<sub>2</sub> and N with respect to the minimal CF basis, i.e. for N<sub>2</sub> by 2 mHa (CF+) and 10 mHa (cc-pCVQZ), and for N by 1 mHa (CF+) and 0.4 mHa (cc-pCVQZ), see also Table B.2. This clearly shows that the HF energy for the minimal CF basis for N<sub>2</sub> is not converged. However, when looking at this table, we also see that our “best” selected cc-pCVQZ basis still differs by almost 5 mHa from the energy for the largest tested basis. This larger difference of 5 mHa is due to the additional f- and g-orbitals. This implies that our largest HF basis does still not yield a converged HF energy. This is different for the N-atom, where the HF energy is found to be converged already for the CF+ and cc-pCVQZ basis.

### 5.2.2 Results & Discussion

The calculated HF, VMC and DMC total energies for the three basis sets, CF, CF+ and cc-pCVQZ, and the same CF pseudopotential are listed in Table 5.3. The resulting HF, VMC and DMC binding energies are listed in Table 5.4.

This paragraph first states our detailed findings before beginning the discussion (and can be skipped). When using the CF+ basis instead of the CF basis, the total energy decreases for N by 2(1) mHa (VMC) and by 0.5(2) mHa (DMC). For N<sub>2</sub>, the total energy decreases by 3(2) mHa (VMC) and by 1.4(4) mHa (DMC). When considering instead the larger cc-pCVQZ basis with respect to the CF basis for N, we find an increase in the total energy by 2(1) mHa (VMC) but a decrease by 2.9(3) mHa (DMC). For N<sub>2</sub>, we obtain a decrease by 1(2) mHa (VMC) and by 9.4(5) mHa (DMC). When looking at the variance for the CF+ basis and compare with the CF basis,  $\sigma$  decreases by a factor of 0.9 for N but remains unchanged for N<sub>2</sub>. In the contrary, when using the largest cc-pCVQZ basis instead of the CF one,  $\sigma$  increases by a factor of 1.3 for N and by 1.2 for N<sub>2</sub>.

As a first observation for the CF+ basis, we obtain a slight decrease in the VMC and DMC total energies of 1-3 times the statistical error, by 2.3(7)-3(2) mHa for VMC and by 0.5(2)-1.4(4) mHa for DMC, compared to values for the CF basis. However, the binding energy is unchanged (i.e. the improvement in the total energy of N and N<sub>2</sub> is similar and “cancels”).

When analyzing our finding for the cc-pCVQZ basis, the VMC results are a little surprising. On the one hand, the VMC total energy increases slightly for N by 2(1) mHa but does not significantly change for N<sub>2</sub> by -1(2) mHa when comparing with respective results for the CF basis. On the other hand, the standard deviation of the local energy increases (by a factor of 1.3 for N and by 1.2 for N<sub>2</sub>) with respect to results by the CF basis. These findings of an increased variance and a more or less unchanged VMC total energy suggest that the quality of the VMC trial wavefunction is poorer for the larger cc-pCVQZ basis (together with the  $\mathcal{J}(553)$ -factor) than for the CF basis.

One might wonder now why  $\Psi_T$  is poorer for an increased HF basis even if the HF total energy is improved for the increased HF basis. However, it is true that a larger HF basis does not necessarily lead to an improved description of  $\Psi_T$  which can be understood as follows. The one-electron (molecular) orbitals in the determinantal part of  $\Psi_T$  are optimized on the HF level. This means that the HF Slater determinant is optimized without including static and dynamic correlation. Since these HF optimized molecular orbitals are then fixed when constructing the correlated  $\Psi_T$  and when optimizing the  $\mathcal{J}$ -parameters, there is no guarantee that the “improved” HF wavefunction also leads to an improvement of the correlated  $\Psi_T$ . It would be interesting in a further study to simultaneously optimize these molecular orbitals in addition to the  $\mathcal{J}$ -parameters. But this is beyond the scope of that thesis.

For the DMC energies, however, we stated already a significant decrease by 2.9(3)

Basis	$E_{\text{HF}}^b$ [in Ha]	$E_{\text{VMC}}^b$ [in Ha]	$E_{\text{DMC}}^b$ [in Ha]	$\Delta E_{\text{DMC}}^b$ [in Ha]
CF	-0.1795	-0.3232(9)	-0.3469(4)	-0.0172(4)
CF+	-0.1872	-0.3216(7)	-0.3473(4)	-0.0168(4)
cc-pCVQZ	-0.1883	-0.327(2)	-0.3505(7)	-0.0136(7)

Table 5.4: This table shows the HF, VMC and DMC binding energies for  $\text{N}_2$  based on Table 5.3. The last column lists the deviation of the DMC total energy from the experimental value (which is -0.3641 Ha, see Table 4.2).

mHa for N and by 9.4(5) mHa for  $\text{N}_2$  (for the cc-pCVQZ basis compared with the CF one). These significant decreases in the DMC results seem rather surprising. When starting with a poorer  $\Psi_T$  with a larger variance, one would generally not expect lower (better) DMC total energies. Therefore, this increase may be accidental. A possible explanation for this larger “unexpected” decrease in  $E_{\text{DMC}}$  (when comparing with results for the CF basis) may be as follows. Since the fixed-node error has a variational character with only positive contributions, we can already rule it out to be the reason for this decrease in  $E_{\text{DMC}}$ . However, the pseudopotential localization error does not satisfy a variational principle for  $E_{\text{DMC}}$  and increases quadratically in  $(\Psi_T - \Psi_0)$  see Section 3.4.3. Therefore, the decrease in the DMC total energy for N and  $\text{N}_2$  could be explained with the poorer trial wavefunction,  $\Psi_T$ , which results in a negative pseudopotential localization error.

One way to confirm this finding of an increase pseudopotential localization error is to use an even larger basis. But also the non-local components of the pseudopotentials determine this error when evaluating eq.(3.81). Therefore, we examine this question in the next section when using different pseudopotentials.

Finally, we like to consider the binding energy in Table 5.4 for this cc-pCVQZ basis and compare with results by the CF basis. We find a lowering (improvement) in the binding energy by 4(3) mHa (VMC) and by 4(1) mHa (DMC) and thus a closer agreement with the experimental value. Yet, these improvements may be considered accidental since the change in the VMC binding energy is based on an increase (worsening) by 2(1) mHa in the atomic VMC energy. For the DMC binding energy, it remains unclear whether the additional decrease of 4 mHa is due to an increased pseudopotential localization error.

To conclude this section, we find that the selected basis set has a considerable influence on the VMC and DMC results. For the CF+ basis, we find slight improvements in the VMC and DMC total energy. But these improvements cancel in the binding energy and become insignificant when comparing with values for the CF basis. For the cc-pCVQZ basis, however, we find a significant improvement in the DMC total and binding energy (and somewhat unchanged VMC total energies). Yet, our findings

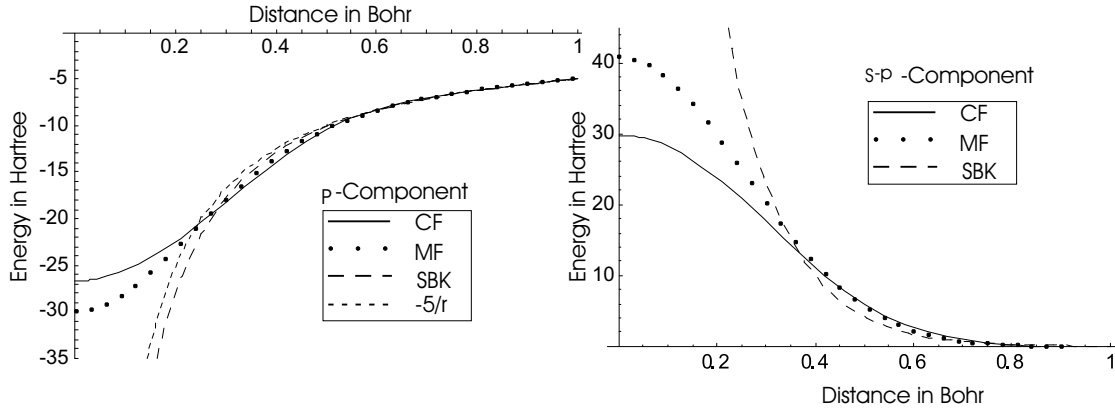


Figure 5.2: For the N-atom, these two diagrams show the angular momentum dependent components of three different pseudopotentials, CF, MF and SBK (see Section 3.4). The diagram on the left hand side compares the respective local  $l$  components, the diagram on the right hand side compares the non-local s-p components.

of larger variances for this cc-pCVQZ basis leave some doubt in these improvements in DMC. If we confirmed this finding (as we will do in the next section), we would obtain an important result for later QMC investigations: When constructing an appropriate correlated VMC trial wavefunctions, it is crucial to consider the obtained variances, even if the VMC total energies seem to be unchanged or when the DMC energies are apparently lowered (improved).

## 5.3 Pseudopotential

Two questions remain to be answered. Can we reduce the deviation of 17(1) mHa from the experimental binding energy for the CF pseudopotential? Is the found improvement of 4(1) mHa in the last section fortuitous for the increased cc-pCVQZ basis set and the CF pseudopotential? In this section, we will examine QMC results for three different pseudopotentials, CF, MF and SBK, which are introduced in Section 3.4. For illustration, their local and non-local radial components are plotted in Figure 5.2. To get an additional feeling about the role of the basis for different pseudopotentials, we will also consider two further basis sets. They are denoted here as MF and pV7CV5Z and taken from Ref.[GAUSSIAN 2003]. The MF basis is constructed from  $7s7p1d$  GTOs with 66 basis functions for  $N_2$ . The pV7CV5Z basis is constructed from  $12s11p9d$  GTOs (constructed by merging the two basis sets, cc-pCV5Z+ and cc-pV7Z) with 198 basis functions for  $N_2$ .

PSP	Basis	$E_{\text{HF}}^{\text{tot}}$	$E_{\text{VMC}}^{\text{tot}}$	$\sigma$	$E_{\text{VMC}}^{\text{corr}}$	$E_{\text{DMC}}^{\text{tot}}$	$E_{\text{DMC}}^{\text{corr}}$
N							
CF	CF+	-9.6487	-9.7607(3)	0.28	-0.1120(3)	-9.7697(1)	-0.1210(1)
MF	MF	-9.6289	-9.7402(4)	0.29	-0.1113(2)	-9.7487(3)	-0.1200(3)
SBK	pV7ZCV5Z	-9.6443	-9.7551(2)	0.28	-0.1108(2)	-9.7649(3)	-0.1206(3)
CF	cc-pCVQZ	-9.6482	-9.7569(7)	0.39	-0.1087(7)	-9.7721(2)	-0.1239(2)
MF	cc-pCVQZ	-9.6283	-9.7384(3)	0.39	-0.1101(3)	-9.7520(2)	-0.1237(2)
SBK	cc-pCVQZ	-9.6437	-9.7559(7)	0.44	-0.1122(7)	-9.7649(5)	-0.1212(5)
N <sub>2</sub>							
CF	CF+	-19.4846	-19.843(1)	0.55	-0.358(1)	-19.8867(2)	-0.4021(2)
MF	MF	-19.4420	-19.802(1)	0.56	-0.360(1)	-19.8442(3)	-0.4022(5)
SBK	pV7ZCV5Z	-19.4769	-19.8368(3)	0.56	-0.3599(3)	-19.8829(5)	-0.4060(4)
CF	cc-pCVQZ	-19.4847	-19.841(1)	0.67	-0.356(1)	-19.8947(3)	-0.4100(3)
MF	cc-pCVQZ	-19.4449	-19.8028(5)	0.66	-0.3579(5)	-19.8527(4)	-0.4078(4)
SBK	cc-pCVQZ	-19.4755	-19.834(1)	0.76	-0.359(1)	-19.8827(6)	-0.4072(6)

Table 5.5: This table presents the HF, VMC and DMC total and correlation energies and the standard deviation of the local energies for three different pseudopotentials, CF, MF and SBK (specified in the first column) and the, MF, cc-pCVQZ and pV7ZCV5Z basis sets (specified in the second column). For all calculations, we choose the  $\mathcal{J}(553)$ -factor and the time step,  $\delta\tau = 0.1 \text{ Ha}^{-1}$ , except for the pV7ZCV5Z basis where  $\delta\tau=0.0025 \text{ Ha}^{-1}$  is chosen (in this calculation, larger time steps caused an instability in the population evolution). All other input parameters are as in Section 4.1. The SBK pseudopotential calculations are done by M. Fuchs.

### 5.3.1 Results & Discussion

For all three pseudopotentials, Table 5.5 presents the calculated HF, VMC and DMC total and correlation energies. Based on these data, the respective binding energies are calculated and listed in Table 5.6. To simplify the discussion, we will limit our examination of the VMC and DMC results for each pseudopotential to those obtained from the basis which leads to the lowest variance (together with the chosen  $\mathcal{J}(553)$ -factor). As a further limitation, only binding and correlation energies can be considered since total energies are rescaled by different pseudopotentials.

Let us consider the correlation energy for the N-atom first. The three VMC calculations for the respective pseudopotentials agree within 1 mHa which is about twice the error bar that we aim at here. The same agreement is found for all three correlation energies with DMC. For additional analysis, one can also consider the difference between the VMC and DMC correlation energy for each respective pseudopotential which is 9.0(2) mHa (CF), 8.7(5) mHa (MF) and 9.8(6) mHa (SBK). Since these differences all agree within their statistical accuracy, they show that the DMC results

yield a consistent improvement upon VMC for all three pseudopotentials. All these findings suggest that the N-atom is systematically well described by the three different pseudopotentials. For  $N_2$ , however, an analogous discussion can not be led since the correlation energy depends on the HF total energy. And in the last section, we demonstrated that these HF values are not converged for example for the CF+ basis (not so for N, where we found that all HF energies for basis sets larger than CF+ are converged).

A further result is the large similarity between the MF and CF pseudopotential calculations for VMC and DMC. This can be seen in the binding energy (i.e. with a difference of 0(4) mHa for VMC and 0(1) mHa for DMC). The same holds for the discussed correlation energy for N and  $N_2$ .<sup>5</sup> Also, the variances for both pseudopotential calculations are very similar. All these findings correspond with our expectation, since both pseudopotentials show a similar qualitative behavior in their local and non-local components, such as the finite value at the nucleus (see Figure 5.2).

When comparing now with the SBK pseudopotential, we find an additional drop (improvement) of the binding energy by 5(3) mHa (VMC) and by 6(2) mHa (DMC). This improvement appears to be systematic when going from VMC (5 mHa) to DMC (6 mHa) and suggests consistency in both methods (similar as found when going from VMC to DMC in the atomic correlation energy). Since we showed consistency within the atomic correlation energies for all three pseudopotentials, we expect this improvement by 6 mHa from an improved result for the  $N_2$  DMC total energy. However, the conclusion we can draw from these findings is that the SBK pseudopotential yields binding energies that are closer to the experimental value.

When resuming the discussion about the cc-pCVQZ basis from Section 5.2, we find further confirmation that the cc-pCVQZ basis is not as appropriate as the CF basis when constructing  $\Psi_T$ . Additionally, we have found similar VMC and DMC atomic correlation energies for all three pseudopotentials. When comparing these “well behaved” VMC atomic correlation energies with the VMC result for the cc-pCVQZ basis, we find a slight increase between 2(1) and 3(1) mHa. In contrast, the same comparison shows a significant decrease in the DMC correlation energy between 2.9(3) and 3.9(5) mHa.<sup>6</sup> Since these findings in the correlation energies suggest the same inconsistent behavior as in the last section (i.e. a slight increase in the VMC correlation energies and a significant decrease in the DMC correlation energy), we have further evidence that the cc-pCVQZ basis yields to “misbehaved” results.

To conclude, we have found a good agreement within our VMC and DMC results for

---

<sup>5</sup>Although we mentioned some reservation when comparing the correlation energies for  $N_2$ , it can be assumed that these two basis sets (i.e. CF+ and MF) yield similar deviation from the true HF limit due to their similar sizes.

<sup>6</sup>An analog discussion for  $N_2$  shows a similar underestimation of the negative correlation energy, i.e. the correlation energy is increased by 2-4 mHa (VMC), whereas the DMC correlation energy is decreased by 4-8 mHa (DMC). But again, this comparison needs to be treated with reservations for reasons mentioned earlier.

PSP	Basis	$E_{\text{VMC}}^b$ [in Ha]	$E_{\text{DMC}}^b$ [in Ha]	$\Delta E_{\text{DMC}}^b$ [in Ha]
CF	CF+	-0.322(2)	-0.3473(4)	-0.0168(4)
MF	MF	-0.322(2)	-0.347(1)	-0.017(1)
SBK	pV7ZCV5Z	-0.327(1)	-0.353(1)	-0.011(1)
CF	cc-pCVQZ	-0.327(2)	-0.3505(7)	-0.0136(7)
MF	cc-pCVQZ	-0.326(2)	-0.3487(8)	-0.0154(8)
SBK	cc-pCVQZ	-0.322(2)	-0.353(2)	-0.011(2)

Table 5.6: This table shows the VMC and DMC binding energies for  $\text{N}_2$  based on the total energies in Table 5.5. The last column lists the deviation of the DMC binding energy from the experimental value (which is -0.3641 Ha, see Table 4.2). For all values, the zero point energy is excluded.

all our three pseudopotentials when describing the N-atom. Also the VMC and DMC binding energies show good agreement for the MF and CF pseudopotential. Substantial systematic improvements in the  $\text{N}_2$  VMC and DMC total energies have been found for the SBK pseudopotential leading to an improved binding energy (i.e. to the current best estimate with a deviation of 11(1) mHa to the experimental value). Finally, we have found further evidence that the “improved” DMC total energies obtained by the cc-pCVQZ basis in the previous section are influenced by a negative pseudopotential localization error. Hence, the improvement of 4(1) mHa in the DMC binding energy obtained for the cc-pCVQZ basis is most likely fortuitous.

### 5.3.2 Comparison with other QMC Calculations

For N and  $\text{N}_2$ , Table 5.7 presents a compilation of available reference DMC total, correlation and binding energies. The reference values closest to the (negative) experimental value are the two DMC binding energies for the SBK pseudopotential with deviations of 6(3) mHa [MITAS 1994] and 6(1) mHa [GROSSMAN 2002]. Both studies only differ in the HF basis set. The next best reference result has already a deviation of 29(1) mHa from the experimental value and is obtained by an all-electron DMC calculation (also for one determinant) [FILIPPI 1996]. A reference binding energy with the largest deviation of 36(100) mHa [SUBRAMANIAM 1992] is obtained by a Greens function QMC method [LESTER 1994] which is an alternative to the short-time approximated DMC method that we use.

So far, our best binding energies overestimate the (negative) experimental value by 17(1) mHa (CF pseudopotential) and by 11(1) mHa (SBK pseudopotential). In comparison, our SBK binding energy slightly overestimates the two reference values obtained for the same pseudopotential, i.e. our value slightly differs by 5(2) mHa to the value by Grossman and has no significant change of 5(4) mHa to the value by Mitas.

PSP	Basis	$E_{\text{DMC}}^{\text{tot}}$	$E_{\text{DMC}}^{\text{corr}}$	$E_{\text{DMC}}^{\text{tot}}$	$E_{\text{DMC}}^{\text{corr}}$	$E_{\text{DMC}}^{\text{b}}$	Ref.
		$\text{N}_2$		$\text{N}$			
-	-	-	-	-	-	-0.3641	expt.
CF	CF+	-19.8867(2)	-0.4021(2)	-9.7697(1)	-0.1210(1)	-0.3473(4)	this work
SBK	pV7ZCV5Z	-19.8829(5)	-0.4060(5)	-9.7649(3)	-0.1206(3)	-0.353(1)	this work
References in QMC							
SBK	Gaussian	-19.888(2)	-0.410(2)	-9.7649(5)	-0.121(1)	-0.358(3)	Mitas
TM	Gaussian	-	-	-9.7944(6))	-0.120(1)	-	Mitas
PC	Gaussian	-	-	-9.7715(9)	-0.121(1)	-	Mitas
SBK	Gaussian?	-	-	-	-	-0.358(1)	Gross.
all-el.	Gaussian	-109.487(1)	-0.494(1)	-54.5760(8)	-	-0.335(3)	Filippi
all-el.	Gaussian	-109.5046(3)	-	-	-	-	Lüchow
all-el.	-	-109.52(8)	-0.53(8)	-54.57(2)	-	-0.4(1)	Sub.

Table 5.7: This table compiles reference total, correlation and binding energies in Hartree. Thereby, all fixed-node DMC calculations are done with a trial wavefunction based on a single Slater determinant. The respective pseudopotential and basis for each reference calculation is listed in the first two columns. The references (Ref.) noted in the last column are (1) [MITAS 1994] where the pseudopotentials PC = Pacious and Christiansen, TM=Troullier Martins are abbreviated, (2) [GROSSMAN 2002] where natural orbitals (nat. orb.) are abbreviated, (3) [FILIPPI 1996] the DMC total energy for  $\text{N}_2$  is taken from this ref., for N we use -54.5760(8) mHa [private communication], both values are for one determinant, (4) [MANTE 2001], (5) [SUBRAMANIAM 1992]. Our binding energies are taken from Table 5.5 and 5.6.



In a more detailed comparison between our SBK results and those by Mitas, we find an excellent agreement between his and our atomic total energy with 0(1) deviation.<sup>7</sup> For N<sub>2</sub> in contrast, our DMC total energy is 5(3) mHa higher (thereby, the HF value of Mitas and our calculations agrees within 1 mHa, i.e. -19.478 mHa by Mitas and -19.477 mHa by us).

These slight differences between our results and those by Grossman and Mitas need further clarification. One could speculate that the differences might be a result of the different HF basis sets, i.e. Mitas uses a *6s6p1d* GTOs basis set which is smaller than our basis with *12s11p9d* GTOs. In the last section, we found that the HF basis can have an influence of several mHa to the binding energy. However, we confirmed our SBK VMC and DMC results for *12s11p9d* GTOs with very similar results found for a second smaller basis with *8s7p5d* GTOs.<sup>8</sup> This agreement in our results does not answer this question. Another possible explanation of these deviations could be the different implementation of the DMC method. Therefore, it is interesting in later studies to further investigate these results in doing a more accurate QMC calculation with MCSCF determinants for Mitas' or our basis set.

In a last comparison with the all-electron DMC calculation by C. Filippi, we find a binding energy with a deviation which is almost twice as large as our deviation for the CF pseudopotential calculation. This shows that an all-electron DMC calculation for one determinant with affordable numerical effort does not give better results than our pseudopotential calculations.

To conclude this comparison, we have found that our N<sub>2</sub> DMC binding energy for the SBK pseudopotential slightly differs from two reference DMC values. In this comparison, we found that our DMC total energy is in good agreement for the atom but is significantly higher for the molecule. Nevertheless, our results obtained by the two other pseudopotentials, CF and MF, yield deviations in the binding energies that are even larger. Only a more accurate DMC calculation using MCSCF determinants might give an answer.<sup>9</sup>

<sup>7</sup>Mitas has obtained atomic correlation energies for three different pseudopotentials (although two of them are not discussed in this thesis). As can be seen in Table 5.7, all his results are between -0.120 to -0.121 Ha. That range is exactly the same as we find for our three pseudopotential calculations in Table 5.5. This once again confirms our previous assertion that the atom is already well described within our DMC calculations.

<sup>8</sup>The results for the *8s7p5d* basis have not been discussed since they show an increased variance. However, they are listed in Table 5.5.

<sup>9</sup>To help explaining the remaining difference of 17(1) mHa to the experimental value, we also investigate our CF pseudopotential with an elaborate CC calculation. Thorsten Klüner (FHI, Berlin) calculated the N<sub>2</sub> binding energy for our pseudopotential and then for all-electrons as comparison (for a set of five different basis sets). The results are listed in Table B.1 in the appendix. When choosing the largest basis (aug-cc-pV5Z), the deviations from the experimental value are 2 mHa for the pseudopotential and 5 mHa for the all-electron calculations. This pseudopotential calculation agrees already fairly well with the experimental value. But this agreement should be considered with reservation for two reasons. (1) The total energy for the next smaller basis (aug-cc-pVQZ)

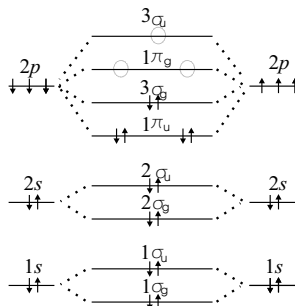


Figure 5.3: This scheme illustrates the molecular orbitals for the  $N_2$ -molecule. Thereby, the  $1\sigma_g$  and  $1\sigma_u$  orbitals are eliminated in our calculations by the use of pseudopotentials.

## 5.4 MCSCF

So far, we could not resolve the discrepancy between our best estimate of the binding energy and the experimental value. Thereby we have always used a single determinant in the construction of previous trial wavefunctions. In this section, we will further extend  $\Psi_T$  by including additional determinants (excited states). In doing so, we hope to improve  $\Psi_T$  and thereby to reduce the fixed-node and pseudopotential localization error (i.e. both errors vanish if  $\Psi_T$  is the true ground state). In particular, we will focus on the  $N_2$  molecule since previous results suggest consistency in the description of the N-atom as was elaborated in the last section.

### 5.4.1 MCSCF Trial Wavefunctions

To find the appropriate determinants when expanding  $\Psi_T$  in determinants as noted in eq.(3.15), we choose the Multi-Configuration Self-Consistent Field (MCSCF) method<sup>10</sup>. First, we determine a set of molecular orbitals (MOs) with a HF calculation for  $N_2$ . Based on these MOs, we then perform a MCSCF calculation with an active space with 3 highest occupied MOs and 3 lowest unoccupied MOs. This means that the determinants within the  $N_2$  MCSCF wavefunction are constructed out of 2 inactive and 6 active HF-MOs which are illustrated in the occupation scheme in Figure

---

increases already by 20 mHa for N and by 40 mHa for  $N_2$  compared to results for the largest basis, see Table B.1. (2) Our DMC total energies are already lower than the respective CC values, i.e. by 13 mHa for N and by 9 mHa for  $N_2$ . (1) and (2) imply that the CC values may not be well enough converged, yet. But despite these concerns, this CC calculation for our pseudopotential seems to yield a  $N_2$  binding energy which is within chemical accuracy (2 mHa) to the experimental value. This agreement supports that our used CF pseudopotential is generally well constructed (see also Section 3.4).

<sup>10</sup>One could also use the CI method, but MCSCF additionally optimizes the MOs insider the determinants. This additional optimization gives rise to an additional improvement of the determinants.

5.3. The following MCSCF calculation then yields the optimized MCSCF wavefunction. From the obtained MCSCF wavefunction, we then extract the determinants with the largest coefficients (the procedure of how to obtain the determinants is summarized in Appendix A.4).

Table 5.8 presents the 17 most important determinants and their weights which are extracted from the previous MCSCF calculation. In this table, these determinants are identified by their electron excitations. After the ground state Slater determinant, the next two important determinants with weights 0.123 represent double excitations of two electrons noted as  $\pi_u^2 \rightarrow \pi_g^2$ . Thereby, two electrons are excited from the double-degenerated  $\pi_u$  MO (i.e. one electron from  $\pi_{u1}$  and the second from  $\pi_{u2}$ ) into the double-degenerated MOs  $\pi_g$  (i.e. one electron into  $\pi_{g1}$  and one into  $\pi_{g2}$ , see also Figure 5.3). The next determinants are the four that describe two single excitations,  $1\pi_{u1}1\pi_{u2} \rightarrow 1\pi_{g1}1\pi_{g2}$ , where two determinants have weights 0.078 and two determinants weights 0.049. Etc. These additional determinants are required to adequately describe the static correlation when constructing the correlated  $\Psi_T$  (see also Section 2.5). In the following, we will present the VMC and DMC total energies when including different numbers of determinants.

## 5.4.2 Results & Discussion

In a first set of calculations, we will optimize the Jastrow factor of  $\Psi_T$ . In a second set, the optimization also includes the coefficients of the determinants. For all calculations, we use the  $\mathcal{J}(550)$  Jastrow factor and the CF basis set and pseudopotential. All VMC and DMC total energies are summarized in Table 5.9. In the same table, the obtained DMC binding energy is listed. These binding energies are calculated from the  $N_2$  DMC total energy for *multiple determinants*, whereas the N-atom total energy is obtained for a *single determinant* and the same  $\mathcal{J}(550)$ -factor. This treatment with different numbers of determinants is justified for two reasons. First, our previous results suggest already a good description of the N-atom. Secondly, for the  $N_2$  molecule we only allow excitations into the  $1\pi_{g1}$ ,  $1\pi_{g2}$  and  $3\sigma_u$  MOs. Similar excitations are not possible for the N-atom. Since any excitation within the  $1s, 2s$  and  $2p$  configuration violates the spin multiplicity of 4 for the N ground state, the HF Slater determinant is the best approximation within this confined active space of  $1s, 2s$  and  $2p$  atomic orbitals. If one had allowed excitations beyond the  $1s, 2s$  and  $2d$ , one would have needed to include MOs beyond  $3\sigma_u$  for the molecule. (See also Figure 5.3 for this argument.)

### Optimization of the Jastrow Factor only

When optimizing only the  $\mathcal{J}$ -factor for 7, 41 and 56 determinants with fixed coefficients, we find an expected monotonic decrease in the DMC total energy for an increasing number of determinants. This improvement upon the single HF determinant is 5(1) mHa when using 56 determinants. The behavior of the VMC total energy

Det. #	Coef.	opt. Coef.	Electron Configuration ( $2\sigma_g, 2\sigma_u, 1\pi_{u1}, 1\pi_{u2}, 3\sigma_g, 1\pi_{g1}, 1\pi_{g2}, 3\sigma_u$ )	Electron Excitation
1	0.9665	0.09849	22222000	HF ground state
2	-0.1228	-0.0784	22022020	$1\pi_{u1}^2 \rightarrow 1\pi_{g2}^2$
3	-0.1228	-0.0784	22202200	$1\pi_{u2}^2 \rightarrow 1\pi_{g1}^2$
4	0.0778	0.0429	22+- 2+- 0	$1\pi_{u1}^+ 1\pi_{u2}^- \rightarrow 1\pi_{g1}^+ 1\pi_{g2}^-$
5	0.0778	0.0429	22- +2- +0	$1\pi_{u1}^- 1\pi_{u2}^+ \rightarrow 1\pi_{g1}^- 1\pi_{g2}^+$
6	0.0493	0.0316	22++2- -0	$1\pi_{u1}^+ 1\pi_{u2}^+ \rightarrow 1\pi_{g1}^+ 1\pi_{g2}^-$
7	0.0493	0.0316	22- - 2++0	$1\pi_{u1}^- 1\pi_{u2}^- \rightarrow 1\pi_{g1}^- 1\pi_{g2}^+$
8	0.0430	0.0235	22- 2+0+-	$3\sigma_g^+ 1\pi_{u1}^- \rightarrow 1\pi_{g2}^+ 3\sigma_u^-$
9	0.0430	0.0235	22+2- 0- +	$3\sigma_g^- 1\pi_{u1}^+ \rightarrow 1\pi_{g2}^- 3\sigma_u^+$
10	-0.0072	-0.0430	222- ++0-	$3\sigma_g^+ 1\pi_{u2}^- \rightarrow 1\pi_{g1}^+ 3\sigma_u^-$
11	-0.0072	-0.0430	222+- - 0+	$3\sigma_g^- 1\pi_{u2}^+ \rightarrow 1\pi_{g1}^- 3\sigma_u^+$
12	0.0275	0.0286	22+- 2- +0	$1\pi_{u1}^+ 1\pi_{u2}^- \rightarrow 1\pi_{g1}^- 1\pi_{g2}^+$
13	0.0275	0.0286	22- +2+- 0	$1\pi_{u1}^- 1\pi_{u2}^+ \rightarrow 1\pi_{g1}^+ 1\pi_{g2}^-$
14	0.0048	0.0162	22- 2+0- +	$3\sigma_g^+ 1\pi_{u1}^- \rightarrow 1\pi_{g2}^+ 3\sigma_u^-$
15	0.0048	0.0162	22+2- 0+-	$3\sigma_g^- 1\pi_{u1}^+ \rightarrow 1\pi_{g2}^- 3\sigma_u^+$
16	-0.0066	-0.0162	222- +- 0+	$3\sigma_g^+ 1\pi_{u2}^- \rightarrow 1\pi_{g1}^+ 3\sigma_u^-$
17	-0.0066	-0.0162	222+- +0-	$3\sigma_g^- 1\pi_{u2}^+ \rightarrow 1\pi_{g1}^- 3\sigma_u^+$

Table 5.8: This table lists the first 17 determinants with largest coefficients when expanding the optimized MCSCF wavefunction for  $N_2$ . The second and third column lists the MCSCF coefficients before and after the optimization of  $\Psi_T$ . Thereby, the sum of the squared coefficients is one. In the MCSCF calculation, we define the active space as the 3 highest occupied MOs and the 3 lowest unoccupied MOs,  $1\pi_{u1}$ ,  $1\pi_{u2}$ ,  $3\sigma_g$ ,  $1\pi_{g1}$ ,  $1\pi_{g2}$ ,  $3\sigma_u$ . The two lowest MOs,  $2\sigma_g, 2\sigma_u$ , are fixed resulting in a total of 8 MOs. Then, each determinant is constructed out of these 8 MOs. This construction is indicated in the forth column, where “+” indicates an occupied MO with a spin up and “-” with a spin down electron or by a pair of electrons indicated by “2”. In the last column, we use the common notation, where we indicate from which and into which MOs the electrons are excited in each determinant. Thereby, each  $\pi$  or  $\sigma$  represents a single electron.

Opt.	No. of Det.	$E_{\text{VMC}}$ [in Ha]	$\sigma_{\text{VMC}}$ [in Ha]	$E_{\text{DMC}}$ [in Ha]	$t_{\text{corr}}$ [in 1/Ha]	$E_{\text{DMC}}^{\text{b}}$ [in 1/Ha]
$\mathcal{J}$ only	1 (HF)	-19.831(1)	0.64	-19.8854(3)	3.28	-0.346(1)
	7	-19.855(1)	0.53	-19.8884(2)	2.87	-0.349(1)
	41	-19.849(1)	0.55	-19.8907(3)	3.19	-0.351(1)
	56	-19.847(1)	0.57	-19.8906(3)	3.32	-0.351(1)
$\mathcal{J}$ and Det.	7	-19.8618(8)	0.52	-19.8941(2)	2.81	-0.355(1)
	17	-19.8624(8)	0.53	-19.8952(2)	2.74	-0.356(1)
	41	-19.8645(9)	0.52	-19.8959(2)	2.82	-0.357(1)
	56	-19.8627(9)	0.51	-19.8947(2)	2.78	-0.355(1)

Table 5.9: This table shows the VMC and DMC total energies which are calculated for 1, 7, 17, 41 and 56 determinants. The last column lists the DMC binding energy. The binding energy is calculated together with the atomic DMC total energy obtained for a single Slater determinant and the same  $\mathcal{J}$ (550)-factor (i.e. -9.7697(6) mHa, see Table 5.1). The upper part of this table lists the results obtained by optimizing the  $\mathcal{J}$ -factor, the lower part is obtained by additionally optimizing the coefficients of the determinants.

is slightly different. Although we find a decrease in the VMC total energy from 1 and 7 determinants by 24(2) mHa, the total energy slightly increases again by 7(2) mHa when going from 7 over 41 to 56 determinants. Also, the variance increases from 0.53 to 0.57.

One might wonder about the decrease (improvement) in the DMC total energy on the one hand, while on the other the VMC total energy and the variance increase again for a number of determinants larger than 7. The reason for this behavior could be similar as discussed in Section 5.2 for the cc-pCVQZ basis. In a MCSCF calculation, the MCSCF determinants are optimized to already describe correlation effects, i.e. mainly static but increasingly dynamic correlation for a larger number of determinants. But when including the  $\mathcal{J}$ -factor, it could be possible that the determinant coefficients stemming from the MCSCF calculation are not appropriate any more. Therefore, we will additionally optimize these determinant coefficients.

### Optimization of the Jastrow Factor and the MCSCF Determinant Coefficients

The VMC and DMC results are illustrated in Figure 5.4 when simultaneously optimizing both, the  $\mathcal{J}$ -parameters and the determinant coefficients. For both, the VMC and DMC total energy, we find a monotonic decrease with the exception of an insignificant increase from 41 to 56 determinants by 2(2) mHa for VMC and a slight increase by 1.2(4) mHa for DMC. Hence, the largest decrease in the total energy is 34(2) mHa for VMC and 10(1) mHa for DMC when going from 1 to 41 determinants.

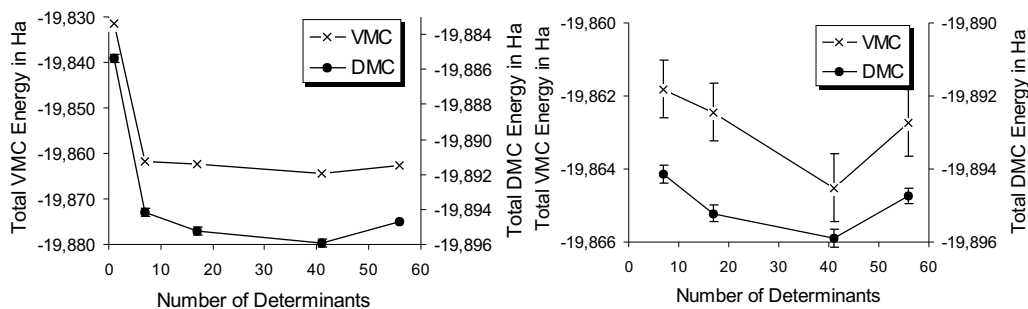


Figure 5.4: These figures show the behavior of the total energy calculated with VMC (left scale) and DMC (right scale) for 1, 7, 17, 41 and 56 determinants in each diagram. (In the left diagram, error bars are smaller than the symbols.) The right diagram excludes the results for a single determinant in order to enlarge the energy scale to make the error bars visible. Here, the  $\mathcal{J}(550)$ -parameters of and all determinant coefficients are simultaneously optimized.

As a first observation, we confirm the necessity to optimize both, the  $\mathcal{J}$ -parameters and the MCSCF coefficients. Their simultaneous optimization yields an additional decrease in the total energies by about 15 mHa (VMC) and by 5 mHa (DMC). Also, the VMC total energy and the variance decreases monotonically for an increasing number of determinants.

At the same time, these improvements also lead to a lower DMC binding energy of -0.357(1) mHa (for 41 determinants). This binding energy now shows the smallest deviation of 7(1) mHa from the experiment compared to 17(1) mHa with a single determinant. This gives an improvement by 10(2) mHa or by 3% of the experimental binding energy. And when comparing with the one determinant result for the SBK pseudopotential, we still find an improvement by 4(2) mHa.

This significant improvement in the  $N_2$  DMC total and binding energy can be traced back to a reduction of the fixed-node error in the  $N_2$ -molecule. The reduction of that error becomes evident when recalling the variational character of the fixed-node approximation and the two findings (1) that the variance reduces by a factor of 0.8 and (2) the VMC total energy decreases by 34(2) mHa when using  $\Psi_T$  with 41 determinants instead of one. Both findings show that  $\Psi_T$  is improved. Supposing that the improved quality of the multi-determinant  $\Psi_T$  leads to an improved nodal surface, this change of 10 mHa indicates that the single-determinant  $\Psi_T$  resulted in a larger fixed-node error that is now (at least partly) corrected. This correction corresponds to 2.5% of the correlation energy or 2.7% of the binding energy. At the same time, also the pseudopotential localization error reduces for a better representation of  $\Psi_T$ . But since this error does not follow a variational principle, the resulting change could be either

negative or positive, and could have contributed to the improvement of 10(2) mHa or worked against.

To conclude, the inclusion of multiple determinants in  $\Psi_T$  substantially improves the VMC and DMC binding energy with a remaining deviation of 7(1) mHa or 1.9% to the experimental value. Also, we find that the additional optimization of the coefficients of the MCSCF determinant is important and yields an additional significant decrease in the VMC and DMC total energy (compared to results obtained by exclusively optimizing the  $\mathcal{J}$ -parameters). When looking for further strategies to improve upon the remaining deviation of 7(1) mHa, our calculations suggest that further increasing the number of determinants (within the chosen active space) will not necessarily improve the DMC result. Instead, one could increase the active space of the MCSCF calculation and also include 3d orbitals (see also the Grossman study in the next subsection). But also, since we found a further improvement by 6(2) mHa when using the SBK pseudopotential in the last section, it would be interesting to investigate the DMC result with this SBK pseudopotential and a multi-determinant  $\Psi_T$ . But this is beyond the scope of this work.

### 5.4.3 Comparison with other QMC MCSCF References

In a QMC study, Grossman investigated the total energy for the phosphorus molecule  $P_2$  which has the same number of valence electrons as  $N_2$  [GROSSMAN 2002]. In the construction of  $\Psi_T$ , he obtained the determinants with the same MCSCF method, but with 16 lowest unoccupied MOs, compared to our 3. This study shows an improvement of the DMC total energy of 7(1) mHa when increasing the number of determinants from 1 to 269. This agrees fairly well with our previous improvement of 10(2) mHa.

In another study, the  $N_2$  VMC and DMC total energy was investigated with an all-electron calculation in Ref.[FILIPPI 1996]. For a  $\Psi_T$  with 17 determinants, this study shows an improvement in the total energy by 62(1) mHa (VMC) and by 18(2) mHa (DMC) compared to a single-determinant  $\Psi_T$ . If we add the same determinants<sup>11</sup> in our (pseudopotential) calculation, the corresponding improvements are 31(2) mHa (VMC) and 10(1) mHa (DMC). Here, our deviation from the reference values is not surprising, since an improvement in the all-electron wavefunction has larger effects than in our pseudo-electron wavefunction. Now, when considering the binding energies, their deviations from the experimental value are  $E_{\text{DMC}}^b = -0.029(3)$  Ha (1 determinant) and  $E_{\text{DMC}}^b = -0.011(3)$  mHa (17 determinants).<sup>12</sup> Their obtained binding

<sup>11</sup>Not only the number of 17 determinants is equal in our and the reference calculation, but also the electronic configuration (all excitations as listed in Table 5.8) of each determinant. However, our 17 determinants are only optimized to account for the spatial symmetry (resulting in 9 free coefficients to optimize), whereas the 17 determinants in the reference calculation are arranged to additionally account for spin symmetry (resulting in 5 free parameters to optimize) [FILIPPI 1996]. Nevertheless, the resulting spin contamination in our calculation is usually neglected.

<sup>12</sup>In Ref.[FILIPPI 1996], no binding energies are calculated. However, these stated binding ener-

energy significantly improves for 17 determinants with respect to experiment. When comparing to our deviation of 7(1) mHa from the experimental binding energy, the all-electron result for 17 determinants are in good agreement with ours (within the error bar of 4 mHa). Hence, this rather good agreement confirms that our pseudopotential calculations yield similar results then all-electron calculations.

---

gies are obtained in a similar manner as we calculated our previous binding energies. Thereby, we use the atomic DMC total energy, -54.5760(8) mHa, obtained for one determinant [Filippi, private communication].



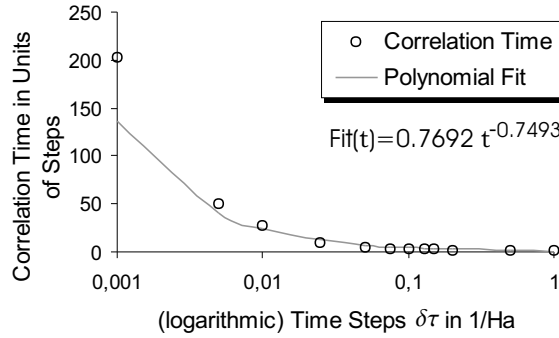


Figure 5.5: For  $\text{N}_2$ , the calculated DMC correlation time,  $t_{\text{corr}}$ , is plotted over the time step,  $\delta\tau$ . All values are taken from Table 5.10.

## 5.5 Time Steps

For all previous calculations, we have used the time step  $\delta\tau = 0.1 \text{ Ha}^{-1}$  (except for the SBK pseudopotential calculations, where  $\delta\tau = 0.0025 \text{ Ha}^{-1}$  was used<sup>13</sup>). In this section, we will examine the influence of different time steps on the DMC total energy. On the one hand, the time step should ideally be zero to make the short time approximation negligible (see Section 3.3.2). On the other hand, the efficiency in the DMC process drastically decreases for smaller time steps since the correlation time,  $t_{\text{corr}}$ , increases. That increase is demonstrated in Figure 5.5 where  $t_{\text{corr}}$  is plotted over the logarithmic time step scale (for smaller time steps,  $t_{\text{corr}}$  must increase larger than an exponential function, since  $t_{\text{corr}}$  can not be appropriately described by a polynomial fit function for smaller time steps when plotting it over a logarithmic scale).

In practice, one commonly performs calculations with several larger time steps and then extrapolates these calculated DMC total energies to the value at  $\delta\tau = 0$  [Schautz, private communication]. Ref.[UMRIGAR et al. 1993] now suggests for our DMC algorithm that the total energy converges, and can already be approximated with a DMC total energy that is obtained for a single time step of the order of  $\delta\tau = 0.1 \text{ Ha}^{-1}$  (i.e. for two elements, Be and  $\text{Li}_2$ , this reference proposes a plateau in the DMC total energy for  $\delta\tau < 0.1 \text{ Ha}^{-1}$ , such that the total energy does not change any more for smaller time steps).

In this section, we examine the convergence behavior of the DMC total energy at different time steps with  $0.001 < \delta\tau < 1 \text{ Ha}^{-1}$  for N and  $\text{N}_2$  and two different basis sets (CF and cc-pCVQZ). All results are illustrated in Figure 5.6. From our calculations, the  $\text{N}_2$  DMC total energies for the CF basis are listed in Table 5.10 for 12 different time steps. To account for the additional increase in the correlation time for smaller

<sup>13</sup>For SBK pseudopotentials, we found an instability in the population evolution for time steps larger than  $\delta\tau = 0.0025 \text{ Ha}^{-1}$  (see Section 5.3).

time steps as shown in Figure 5.5), we also need to increase the number of diffusion steps within one block (for example, at  $\delta\tau = 0.001$  with  $t_{\text{corr}} = 203$ , we use 12,000 steps within one block).<sup>14</sup>

### 5.5.1 Results & Discussion for Different Time Steps

When looking at the DMC total energy for the CF basis first, the upper diagram in Figure 5.6 on the left hand side shows an increase in the total energy when starting from  $\tau = 0.5 \text{ Ha}^{-1}$  and going down to smaller values. For both N and N<sub>2</sub>, the total energy reaches a maximum and then decreases up to 4.6(8) mHa for N<sub>2</sub> and up to 1.2 (5) mH for N. The diagram in the second row presents the same data over a logarithmic scale. The constant negative slope of the DMC total energy for small time steps (over the logarithmic scale) suggests that the total energy is still not converged for our smallest time step. For the cc-pCVQZ basis in contrast, we find a different trend illustrated on the right hand side of Figure 5.6. The DMC total energy monotonically increases for both N and N<sub>2</sub> for small time steps. On a logarithmic scale, the slopes of the N and N<sub>2</sub> total energies becomes horizontal for small time steps which suggests that the total energy is converged for even smaller time steps.

In the above results, two findings appear to be peculiar. First, we do not find the expected plateau in the DMC total energies for smaller time steps for both basis sets. In particular for the CF basis, the DMC total energies do not seem to converge. And secondly, the behavior for smaller time steps seems to depend on the chosen basis set, i.e. for small time steps, the total energy decreases for the CF basis and increases for the cc-pCVQZ basis.

We have not really understood the reason for these results. One possible explanation for both of these finding could be the occurrence of a pseudopotential localization error which would allow an explanation of the negative and positive deviation (depending on the basis set). But this findings could also be a result from the used DMC implementation. However, these changes in the total energies appear to be less important for the binding energy when looking at the two bottom diagrams in Figure 5.6. In particular, the largest decrease in the binding energy for the CF basis is between  $\delta\tau = 0.1 \text{ Ha}^{-1}$  and  $\delta\tau = 0.01 \text{ Ha}^{-1}$  with  $2.5 \pm 1.0 \text{ mHa}$ . But this lowering in the binding energy appears to be slightly reversed for even smaller time steps. For the cc-pCVQZ basis all differences are within  $1.3 \pm 1.5 \text{ mHa}$  and are not significant.

As a conclusion from our time step investigation, we find a behavior of the DMC total energy which is different from our expectation of a plateau for time steps smaller than  $0.1 \text{ Ha}^{-1}$ . For the CF basis, we find a maximum in the total energy and an additional significant decrease by 5(1) mHa for the smallest time step investigated. In the contrary, no plateau was found for the cc-pCVQZ basis. However, the binding

---

<sup>14</sup>As a rule of thumb, we try to keep the block size as large as ten times the correlation time,  $t_{\text{corr}}$  [private communication, C. Filippi], while keeping the number of 8000 diffusion blocks fixed.

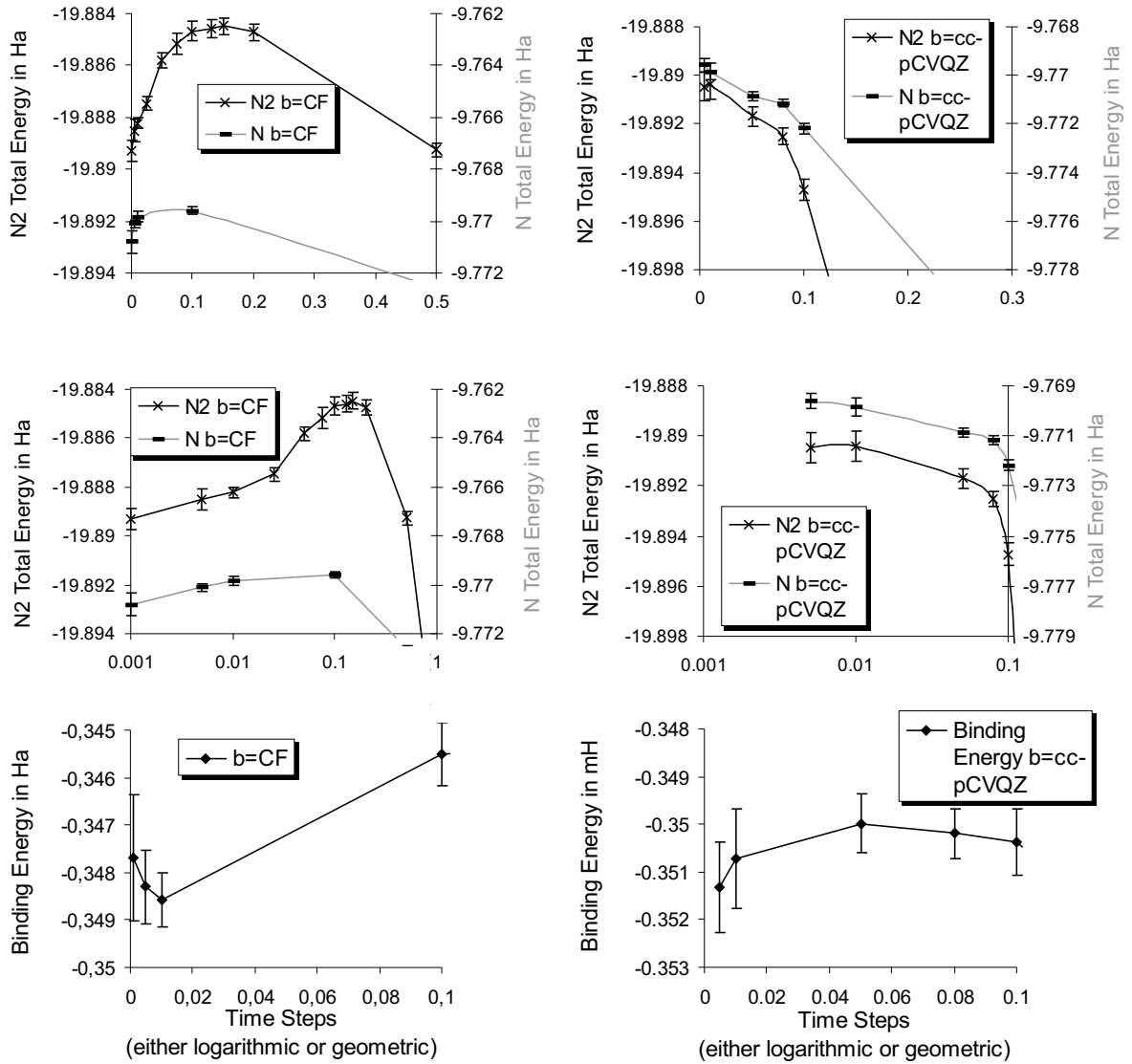


Figure 5.6: The diagrams show the time step convergence for the DMC total energy for N and N<sub>2</sub> for two different basis sets, CF and cc-pCVQZ. All diagrams on the left hand side refer to the CF basis, all diagrams on the right hand side to the cc-pCVQZ basis. In particular, the first diagram in each column shows the total energy behavior for N and N<sub>2</sub>. All abscissas are assigned an equi-distant energy scale for a better comparison where the left scale refers to the N<sub>2</sub> and the right one to N (indicated through the gray color). The diagrams in the second row show the same information but on a logarithmic time step scale. The two diagrams on the bottom show the binding energy over different time steps. As input, we use a single Slater determinant, the  $\mathcal{J}(553)$ -factor and other parameters as listed in Table 5.10.

## 5.6. TIME EVOLUTION IN DMC

Input				Output			
$\delta\tau$	Steps/Block	Blocks	Total Points	$E_{\text{DMC}}^{\text{tot}}$	$\delta\tau_{\text{eff}}$	$\tau_{\text{eff}}$	$t_{\text{corr}}$
[in Ha <sup>-1</sup> ]	#	#	[# in million]	[in Ha]	[in Ha <sup>-1</sup> ]	[in Ha <sup>-1</sup> ]	#
0.001	12000	8000	3840	-19.8893(4)	0.001	96000	202.62
0.005	600	8000	192	-19.8885(4)	0.0049	23952	49.93
0.01	600	8000	192	-19.8882(2)	0.0099	47664	26.96
0.025	100	12000	48	-19.8875(3)	0.0244	29328	9.87
0.05	50	12000	24	-19.8858(3)	0.0474	28446	5.29
0.075	50	8000	16	-19.8852(4)	0.0688	27512	3.92
0.1	50	8000	16	-19.8853(2)	0.0886	35452	3.23
0.13	50	8000	16	-19.8846(3)	0.1105	44216	2.62
0.15	50	8000	16	-19.8845(3)	0.1240	49616	2.54
0.2	50	8000	16	-19.8847(3)	0.1543	61732	2.22
0.5	50	8000	16	-19.8893(3)	0.2635	105400	1.68
1	50	8000	16	-19.8952(3)	0.3055	122208	1.78

Table 5.10: This table shows the N<sub>2</sub> DMC total energy for different time steps,  $\delta\tau$ , using the CF basis set. In particular, the number of diffusion steps per block, the number of blocks and the resulting total number of sampling points [number/block  $\times$  (number of blocks)  $\times$  (number of populations, nconf=40)] are listed. This table also shows the resulting effective time step,  $\delta\tau_{\text{eff}}$ , the effective diffusion time,  $\tau_{\text{err}} = \delta\tau_{\text{eff}} \times \text{number/block} \times (\text{number of blocks})$ , and the correlation time,  $t_{\text{corr}}$ .

energy is less effected when going to smaller time steps. But still, we find a drop of  $2.5 \pm 1.0$  mHa for the CF basis (and no significant change for the cc-pCVQZ basis). However, this finding suggests that the influence of the time step should be investigated in all future studies.

## 5.6 Time Evolution in DMC

So far, we have used a fixed population size of 40 walkers. In this section, we examine the influence of the waker size on the DMC total energy for N<sub>2</sub>. At the same time, we will examining the time evolution of the DMC total energy. To do so, we choose four different population sizes with 3,10, 50 and 130 walkers, a time step of  $\delta\tau = 0.1$  Ha<sup>-1</sup>, a block size of 50 walkers, 8000 blocks and the  $\mathcal{J}(553)$  Jastrow-factor. Figure 5.7 presents the time evolution of the N<sub>2</sub> DMC total energy for these four population sizes.

We find that the calculation with the smallest population (of 3 walkers) also shows the largest fluctuation throughout the entire diffusion time. This fluctuation then reduces for an increasing number of walkers. And when comparing the two largest populations

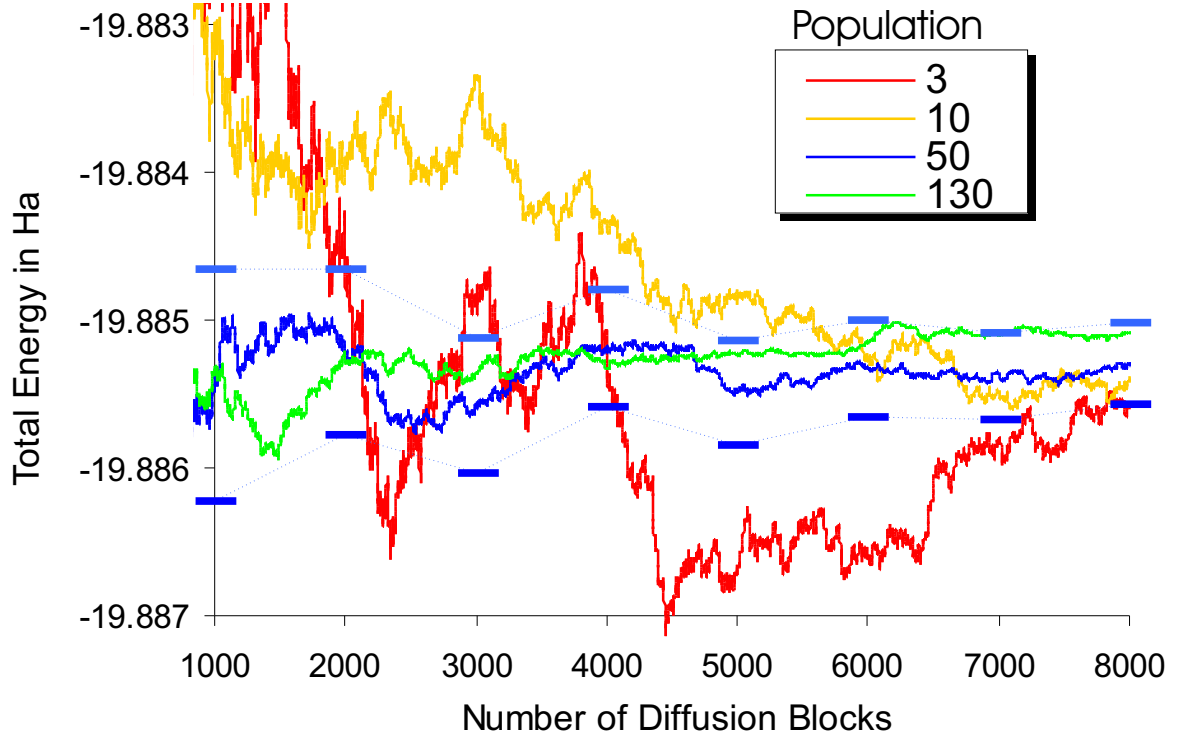


Figure 5.7: This figure shows the time evolution of the DMC total energy for  $N_2$  calculated with different population sizes of 3, 10, 50 and 130 walkers. This time evolution is plotted over the number of blocks starting with 1000 blocks (the initial blocks are omitted due to large fluctuation in the total energy). For the population of 50 walkers (blue line), the statistical error bar is included. The explicit values for the  $N_2$  DMC total energies (and errors) after 8000 blocks are -19.886(1) Ha (3 walkers), -19.8854 (6) Ha (10 walkers), -19.8853(3) Ha (50 walkers) and -19.8851(2) Ha (130 walkers). For all calculations, a block size of 50 walkers,  $\mathcal{J}(553)$  and  $\delta\tau = 0.1 \text{ Ha}^{-1}$  is used.

## 5.7. DIFFERENT QUADRATURE RULES

nquad	Basis	$E_{\text{DMC}}(\text{N})$	$E_{\text{DMC}}(\text{N}_2)$
#		[in Ha]	[in Ha]
4	CF	-9.7693(1)	-19.8853(2)
6	CF	-9.7692(1)	-19.8848(2)
12	CF	-9.7691(1)	-19.8853(2)
86	CF	-9.7692(1)	-19.8849(2)
4	cc-pCVQZ	-9.7724(2)	-19.8947(4)
6	cc-pCVQZ	-9.7721(2)	-19.8938(4)
12	cc-pCVQZ	-9.7722(2)	-19.8942(4)
86	cc-pCVQZ	-9.7721(2)	-19.8948(4)

Table 5.11: For the N-atom and  $\text{N}_2$ , this table presents the DMC total energies for different numbers of quadrature points and two different basis sets both specified in the first two columns. The VMC trial wavefunctions used for these calculations are previously optimized using four quadrature points. For all calculations, 8,000 blocks, a block size of 50 walkers, a population size of 40 walkers,  $\mathcal{J}(553)$  and  $\delta\tau = 0.1 \text{ Ha}^{-1}$  is used.

(50 and 130 walkers), their DMC total energies evolve very similarly. Also, for all four walker sizes, the final DMC energy after 8000 blocks agrees within their statistical errors (listed in the caption).

As a conclusion, we find that the choice of our four population sizes has no significant effect on the results after a sufficient long time evolution (like 8000 blocks in our case with a resulting diffusion time of  $\tau = 40,000 \text{ Ha}^{-1}$ ). Also, the DMC total energy for the two larger populations seem to be converged already after 4000 blocks (other than for the two smaller populations). These findings suggest that all calculations in the previous sections with walker sizes of 50 (or 40) and a block size of 4000 are not significantly influenced by the number of walkers. And the evolution time is chosen sufficiently long in our calculations.

## 5.7 Different Quadrature Rules

In all previous sections, we have used four quadrature points to evaluate the two-dimensional surface integral in eq.(3.77) for any VMC and DMC calculation (see also Section 3.4.2). In this section, we investigate the influence of different quadrature points on the DMC total energy for two different basis sets, CF and cc-pCVQZ. In particular, 4, 6, 12 and 86 quadrature points are chosen at which the two-dimensional surface integral is evaluated in a DMC calculation. Table 5.11 presents the DMC total energies obtained by the different numbers of quadrature points and basis sets for N and  $\text{N}_2$ . All DMC calculations are based on the same trial wavefunction<sup>15</sup>. Further

<sup>15</sup>In the optimization of  $\Psi_{\text{T}}$ , four quadrature points are used in each VMC run.

VMC and DMC input parameters are specified in the caption.

We find that all deviations in the DMC total energy for different quadrature points for N and N<sub>2</sub> are within (or close to) one standard deviation. Our results indicate that the 6 point quadrature method yields slightly higher total energies for both basis sets and for N and N<sub>2</sub> when comparing with all other results. But these differences are not significant. Therefore, our results could not identify any significant influence on the DMC total (binding) energy when evaluating the non-local components of the pseudopotential for different numbers of quadrature points.

## 5.8 Correlated Sampling

In Section 4.2 and 4.3, we used the VMC and DMC orbital re-optimized correlated sampling method to determine the equilibrium geometry and the vibrational frequency for selected molecules. In this section, we examine the convergence of these two physical properties for N<sub>2</sub> over the diffusion time (the number of blocks). In particular, we will compare these results obtained by the *orbital re-optimized* correlation sampling method with the *re-centered* correlated sampling method (introduced in Section 3.5.3). The first method uses a re-optimized HF wavefunction for each geometry of the potential energy curve, whereas the second method uses a re-centered reference HF wavefunction for each geometry. Also, we like to investigate the influence of the selected reference (or primary) geometry by calculating the potential energy surface for different reference points.

### 5.8.1 The Potential Energy Curve and the Diffusion Time

Figure 5.8 presents the N<sub>2</sub> potential energy surface after 2000, 4000, 6000 and 8000 diffusion blocks (in Section 4.2 and 4.3 we used 4000 for all calculations). The derived bond lengths and vibrational frequencies are listed in this same figure. We find that when going from 2000 to 4000, to 6000 and to 8000 blocks, the respective changes in the equilibrium bond length are 0.0001(15) Å, 0.0004(11) Å and 0.0001(9) Å. The vibrational frequency changes by 1(91) cm<sup>-1</sup>, 3(73) cm<sup>-1</sup> and 0(65) cm<sup>-1</sup>, accordingly.

To summarize, the observed changes in the bond lengths and vibrational frequencies for different block lengths are several times smaller than the assessed statistical error bars, which is less than 0.001 Å for the bond length and less than 30-60 cm<sup>-1</sup> in the vibrational frequency. In turn, our results suggest that not much more accuracy is gained for more than 2000 blocks (or a diffusion time larger than  $\tau = 10.000$  Ha<sup>-1</sup>). Therefore, we can conclude that both physical properties are well converged for our calculations with 4000 blocks.

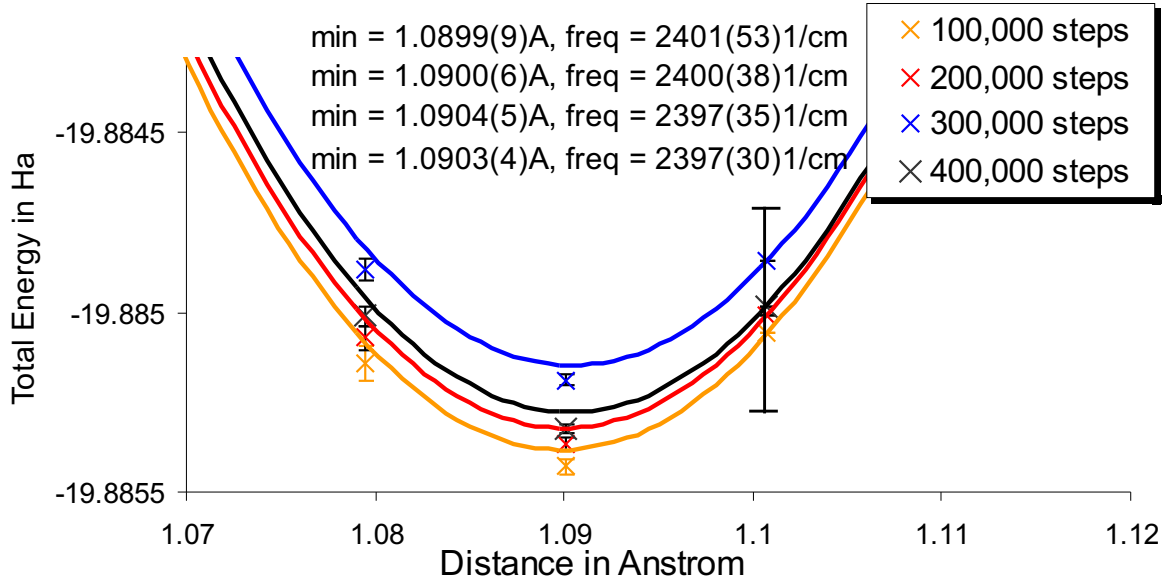


Figure 5.8: For different numbers of diffusion blocks, this figure presents the potential energy surface for  $N_2$  calculated with the orbital re-optimized correlated sampling DMC method. The two derived physical properties, bond length and vibrational frequency, are listed in the diagram for different numbers of diffusion blocks. For these calculations, we use the reference geometry 1.101 Å, the CF pseudopotential, the CF basis,  $\delta\tau=0.1 \text{ Ha}^{-1}$ ,  $\mathcal{J}(553)$ , a block size of 50 walkers and a population of 40 walkers. The error bars in the bond length and the vibrational frequency are obtained as described in Section 4.2 and 4.3. It should be noticed, that the indicated error bars in the total energies refer to the difference in the total energy with respect to the reference geometry. And for the total energy at the reference geometry, this diagram shows the error bar for a normal (uncorrelated) DMC calculation. (Since the uncorrelated error bars are in the order of 1mHa, we only included a single error bar for the total energy after diffusion 200,000 steps.)



### 5.8.2 Orbital Re-Optimized versus Re-Centered Correlated Sampling

Before discussing the two correlated sampling (CS) methods, let us consider “uncorrelated” VMC and DMC calculations for different geometries. They are presented in the first two diagrams in Figure 5.9. These diagrams show significant fluctuations in the VMC (left diagram) and DMC (right diagram) total energies between different geometries (i.e. fluctuations of several times the statistical error). Hence, the physical properties derived from such uncorrelated VMC and DMC calculations are subject to very large errors. This shows the need for the CS methods as used in this thesis.

In Section 4.2, we used the orbital re-optimized correlated sampling method. Now, we will compare this method with the re-centered correlation sampling method. Figure 5.9 shows the calculated  $N_2$  potential energy curves by applying both CS methods in VMC (second row) and in DMC (third row). Thereby, the reference geometry 1.08 Å (left diagrams) and 1.101 Å (right diagrams) is used. (In Figure 5.9, the reference geometry is indicated with a circle.) Let us first compare the two different methods, then, we will discuss the influence of the reference geometry.

When comparing the re-centered with the re-optimized CS calculations (at the 1.08 Å reference geometry), we see a systematic improvement of the vibrational frequency by 389(182)  $\text{cm}^{-1}$  (VMC) and by 149(104)  $\text{cm}^{-1}$  (DMC), respectively. For the bond length, we find no significant difference, i.e. by 0.001(2) Å (VMC) and by 0.000(2) Å (DMC). In the same comparison but at a different reference geometry at 1.101 Å, we find similar systematic improvements of the vibrational frequency but a slight worsening for the bond length (i.e. by 0.005(3) Å (VMC) and by 0.002(1) Å (DMC) with respect to the experimental value at 1.094 Å.)

To summarize the difference between the re-centered and orbital reoptimized CS method, we find that the vibrational frequency is significantly improved (more than twice than the error bar) for the re-optimized CS method. This improvement is in agreement with our expectation, since the optimized HF determinant (in the orbital re-optimized CS method) allows for an improved  $\Psi_T$  at the secondary geometries. When recalling that the fixed node error is variational, it becomes evident that an improved  $\Psi_T$  lowers the total energy at the secondary geometries and thus the curvature in the potential energy curve. At the same time, no significant change has been found in the bond length (only a slight but insignificant worsening when using the re-optimized CS method).

Now, we discuss our findings when comparing the two different reference geometries. The difference obtained by the re-centered CS method at the two reference geometries are not significant in the frequencies (i.e. 179(176)  $\text{cm}^{-1}$  for VMC and of 30(117)  $\text{cm}^{-1}$  for DMC). While for the bond length, we find slight differences of 0.009(3) mHa (VMC) and 0.004(2) mHa (DMC) for the two reference geometries. In the same comparison between the two reference geometries for the re-optimized CS method, we find a similar

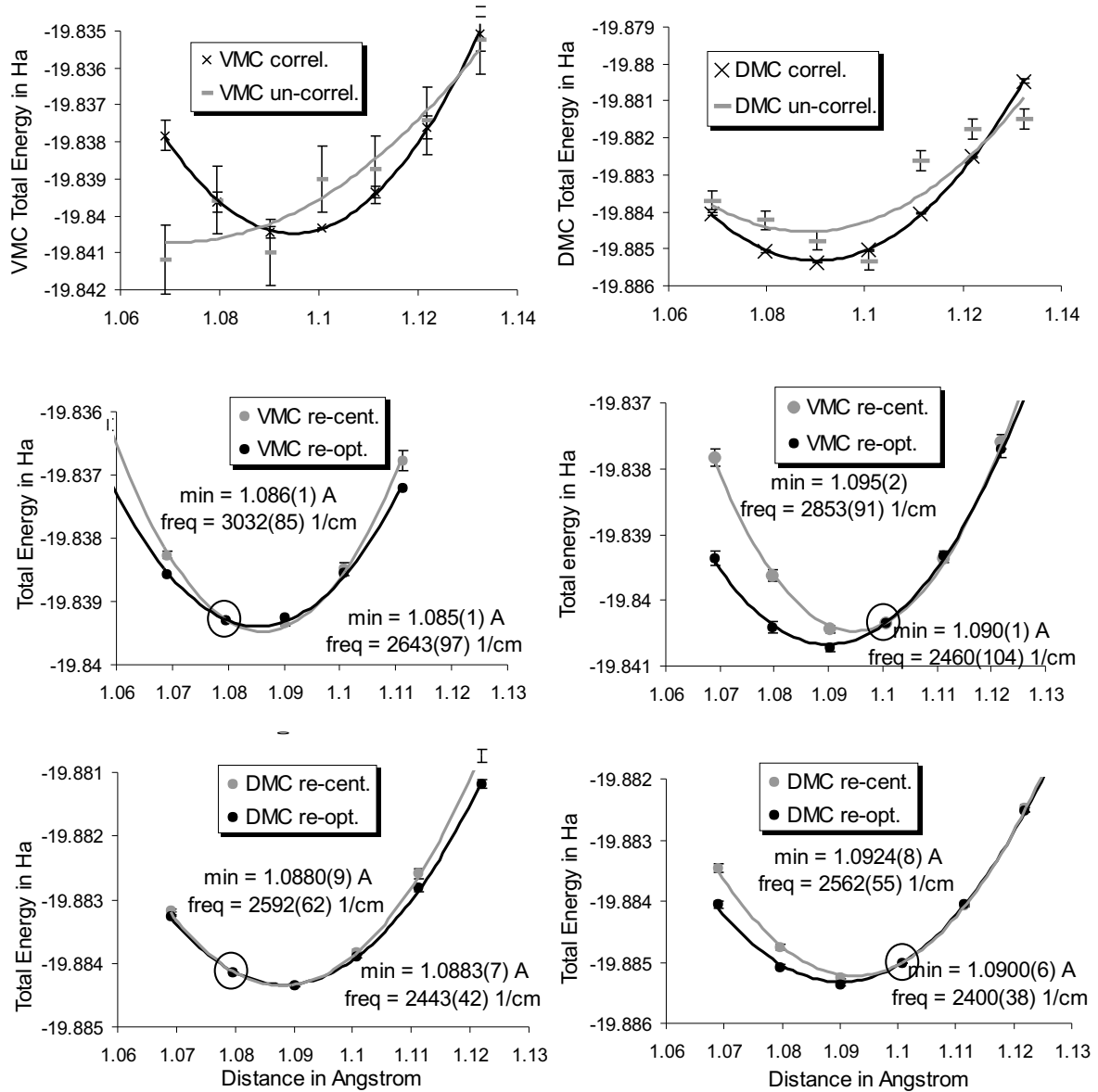


Figure 5.9: All diagrams show the potential energy curve for  $N_2$ . The two upper diagrams compare both correlated and uncorrelated sampling calculations for VMC (on the left hand side) and for DMC (on the right hand side). The two diagrams in the second row compare VMC re-centered and orbital re-optimized correlated sampling calculations for two different reference geometries, for 1.080 Å (on the left hand side) and for 1.101 Å (on the right hand side). The two lower diagrams show the same comparison for DMC calculations. The respective reference points are encircled in all diagrams. For all calculations, we use the CF pseudopotential and basis. For the DMC calculation, we used  $\delta\tau=0.1$  Ha $^{-1}$ ,  $\mathcal{J}(553)$ , 4000 blocks, a population size of 40 walker and a block size of 50 walkers. For the VMC calculation, we used a 30,000 blocks and a block size of 20.

insignificant change in the frequencies and a similar slight changes in the bond length (i.e. 0.005(2) Å (VMC) and by 0.002(1) Å (DMC)).

When summarizing the influence of the reference points on the physical properties from our previous comparison, we find no significant influence on vibrational frequencies. Not so for bond lengths, there we find a slight dependence on the choice of the reference point for both CS method likewise. In particular, we find an influence that can exceed the statistical error bar of currently 0.002 Å by about 2-3 times.

To conclude this section, our investigations suggest that the used orbital re-optimized CS method yields more reliable results when determining the vibrational frequencies than compared to the re-centered method. However, a similar improvement is not indicated by our results when calculating bond lengths. Also, we found that the choice of the reference points has an influence on the bond length which may exceed several times the statistical error bar. This influence need to be incorporated when calculating bond length with the CS technique investigated in this thesis.



# Chapter 6

## Summary and Outlook

In this thesis, we investigated the capability of the Variational Monte Carlo (VMC) and the Diffusion Monte Carlo (DMC) method when performing electronic structure calculations. We examined selected physical properties of nine first and second row molecules. We furthermore showed that DMC, as a correlated total energy method, is very appropriate when describing hydrogen-bonding energetics and proton transfer energy barriers for two selected H-bonding systems. Thereby, DMC allowed us to check for deficiencies in other reference methods (like DFT).

For our investigated molecules, we obtained dissociation energies, equilibrium geometries and fundamental vibrational frequencies with similar accuracy as found by quantum chemical methods (like MP2, CISD(T), CCSD(T)), or Density Functional Theory (DFT) methods (like BLYP or B3LYP). We used the specific CHAMP implementation of the VMC and fixed-node DMC method with a single Slater determinant trial wavefunction. Our best estimates for all binding energies showed an average absolute deviation from the (negative) experimental value by +0.22(1) eV. For the equilibrium geometries and vibrational frequencies, we used a recently developed correlated sampling method. This method allowed us to significantly reduce the statistical fluctuations - a necessity when adequately calculating small energy differences (interatomic forces). Our best DMC results for these molecules showed bond lengths that differed between 0.000(1) Å and 0.014(1) Å from the experimental value. For the vibrational frequencies, the deviations from the experimental value is rather systematic with an average deviation of +46(42) cm<sup>-1</sup>. Although our binding energies still showed slight deviations from the experimental value, our results confirmed the soundness of the applied DMC method when comparing with alternative quantum chemical or DFT methods.

In addition to these nine covalently bonded molecules, two model systems (di-ammonia and malonaldehyde) for weak and strong H-bonding were investigated. In particular, we examined the H-bonding energetics and the proton transfer energy barrier. These two quantities play a key role for the understanding of biomolecules. Our results

agreed fairly well with elaborate reference CCSD(T) values where available. For the di-ammonia proton barrier, our QMC calculation were the first benchmark calculation beyond two DFT calculations. Since DMC gives in principle an accurate treatment of the exchange-correlation energy, it is a useful tool for benchmarking and to check for deficiencies of other methods (like DFT upon its GGA approximation). In our investigations, we clearly confirmed a severe underestimation by the DFT-PBE and DFT-PBE-LDA methods when describing energy barriers. For malonaldehyde, an underestimation is found by 0.08 eV or 82% (PBE) and by 0.03 eV or 33% (PBE-LDA). A similar result is found for di-ammonia with an underestimation by 0.61 eV or 23% (PBE) and by 0.2 eV or 8% (PBE-LDA). At the same time, we found that the PBE optimized equilibrium structure is improved over the PBE-LDA optimized one. More investigations of this kind on a much wider set of H-bonded systems with QMC would help to further generalize statements such as found for our H-bonded model types.

The third major investigation of this thesis was an in-depth study of the  $N_2$  molecule. We identified relevant aspects in our VMC and DMC methods giving rise to systematic errors in the total and binding energy. Four major findings were made in this context:

(1) We found that an improved basis set in our HF calculations did not necessarily lead to an improved representation of the correlated trial wavefunction and thus to an improved DMC result. This showed the requirement of a careful optimization of the initial trial wavefunction used in DMC.

(2) From our test of different pseudopotentials, we identified their influence on the binding energy as large as 0.2 eV which is in agreement with values found in the literature [MITAS 1994]. The best binding energies were found for the Stevens-Basch-Kraus (SBK) pseudopotential. However, we could not clarify the slight difference in the binding energy between our SBK pseudopotential calculations and those by two SBK reference DMC studies. This difference of 0.14(3) eV or 5(1) mHa could be a result of the different basis sets chosen. But since we found no evidence for such an influence in our SBK calculations for different basis sets, this slight deviation could also be a result of the different DMC implementations. Only a more elaborate QMC calculation with more determinants can further clarify that.

(3) We found a significant improvements in the DMC binding energy when using a multi-determinant ansatz in the trial wavefunction. For the  $N_2$  total and binding energy, we found a decrease by -0.27(3) eV or -10(1) mHa compared to results for a single Slater determinant (and the CF pseudopotential). This improvement led to our best estimate of the  $N_2$  binding energy with a deviation of 0.19(3) eV from the experimental value (which is 1.9% of the binding energy). Hence, this significant change in the binding energy is most likely be the result of a reduced fixed-node or pseudopotential localization error. This clearly shows that later QMC calculation should rely on these improved trial wavefunctions.

(4) Also, we identified that the chosen time step in our DMC calculations can have an

influence as large as 0.07(3) eV. Hence, later studies in DMC should also pay attention to the influence of the chosen time step on the DMC results.

To conclude, this thesis has demonstrated that DMC results already compare well with quantum chemical and DFT reference methods. Also, systematic errors in our QMC calculations could largely be controlled and substantially reduced, although with an increase in computational effort. More systematic QMC studies for different basis sets, pseudopotentials and many-determinant trial wavefunction will be important to further improve the understanding of the influence of specific approximations made within QMC. Their understanding is crucial for the DMC method to become an important tool in electronic structure calculations since it provides in principle a highly accurate and systematically controlled treatment of many-electron correlation.





# Appendix A

## A.1 Harmonic Approximation of the BOS

The BOS,  $E_0^{\text{BOS}}$ , given in eq.(2.9), describes the effective potential of the motion of  $M$  nuclei with coordinates  $\mathbf{R}$ , where the **equilibrium geometry**  $\mathbf{R}_0 = (\mathbf{R}_{01}, \dots, \mathbf{R}_{0M})$  of the  $M$  nuclei is defined at the minimum of the BOS,

$$\left( \frac{\partial E_0^{\text{BOS}}(\mathbf{R})}{\partial \mathbf{R}} \right)_{\mathbf{R}=\mathbf{R}_0} = 0, . \quad (\text{A.1})$$

When expanding  $E_0^{\text{BOS}}$  around the equilibrium geometry  $\mathbf{R}_0$  for small displacements of the  $M$  nuclei,  $E_0^{\text{BOS}}$  can be harmonically approximated<sup>1</sup>,

$$E_0^{\text{BOS}}(\mathbf{R}) \approx E_0^{\text{BOS}}(\mathbf{R}_0) + \frac{1}{2} \sum_{I,J}^M (\mathbf{R}_{0I} - \mathbf{R}_{0I}) \mathbf{H}_{I,J} (\mathbf{R}_{0J} - \mathbf{R}_{0J}) \quad (\text{A.2})$$

$$\text{with} \quad \mathbf{H}_{I,J} = \left( \frac{\partial^2 E_0^{\text{BOS}}(\mathbf{R})}{\partial \mathbf{R}_I \partial \mathbf{R}_J} \right)_{\mathbf{R}=\mathbf{R}_0}, \quad (\text{A.3})$$

The linear term in the expansion vanishes as a result of eq.(A.1).  $\mathbf{H}$  is the  $(3M \times 3M)$ -dimensional Hessian or **force constant matrix**. Its secular equation,

$$|\mathbf{H} - \lambda_i^2 \hat{1}| = 0, \quad (\text{A.4})$$

yields eigen-values,  $\lambda_i$  with  $i = 1, \dots, 3M$ , and -vectors which are forces and corresponding normal coordinates, respectively.  $\hat{1}$  is the unity matrix.

---

<sup>1</sup>The further splitting of  $\mathbf{R}_J$  into the x,y and z components has been omitted for simplicity. Consequently, the expression (A.5) itself is a  $(3 \times 3)$ -matrix.

## A.2. INTERNAL AND MASS-WEIGHTED COORDINATES FOR H<sub>2</sub>O

When introducing three-dimensional mass-weighted coordinates,  $\eta_J = \sqrt{m_J}(\mathbf{R}_J - \mathbf{R}_{0J})$  for  $M$  nuclei with  $J = 1, \dots, M$  and nuclear masses  $m_J$ , the force matrix  $\mathbf{H}$  can be transformed into the  $(3M \times 3M)$ -dimensional **dynamical matrix**  $\mathbf{D}$ , with

$$\mathbf{D}_{I,J} := \frac{\mathbf{H}_{I,J}}{\sqrt{m_I m_J}} = \frac{1}{\sqrt{m_I m_J}} \left( \frac{\partial^2 E_0^{\text{BOS}}}{\partial \mathbf{R}_I \partial \mathbf{R}_J} \right)_{\mathbf{R}_0} = \left( \frac{\partial^2 E_0^{\text{BOS}}}{\partial \eta_I \partial \eta_J} \right)_0. \quad (\text{A.5})$$

The eigenvalues of the dynamical matrix, obtained by its secular equation,

$$|\mathbf{D} - \omega_i^2 \hat{1}| = 0, \quad (\text{A.6})$$

are the  $3M$  harmonic vibrational frequencies  $\omega_i$  for  $3M$  independent harmonic oscillators. The  $3M$  eigenvectors correspond to the mass weighted normal coordinates.

## A.2 Internal and Mass-weighted Coordinates for H<sub>2</sub>O

The normal coordinates  $S_1, S_2$  and  $S_3$  for H<sub>2</sub>O of the force matrix in Section 4.2 can geometrically be constructed from Figure 4.3a,

$$\begin{aligned} S_1 &= -(\xi_1 \sin \Theta + \xi_2 \cos \Theta) + \xi_5 \sin \Theta + \xi \cos \Theta \\ S_2 &= \xi_3 \sin \Theta - \xi_4 \cos \Theta - \xi_5 \sin \Theta + \xi \cos \Theta \\ S_3 &= \frac{1}{r_e}(-\xi_1 \cos \Theta + \xi_2 \sin \Theta + \xi_3 \cos \Theta + \xi_4 \sin \Theta - \xi_6 \sin \Theta). \end{aligned} \quad (\text{A.7})$$

As discussed in Section 4.3, H<sub>2</sub>O has six Cartesian coordinates,  $\zeta_i$  with  $i=1, \dots, 6$ . When transforming these coordinates into six mass-weighted coordinates,  $\boldsymbol{\eta} = (\eta_1, \dots, \eta_6)$ , as defined in the previous section, the matrix  $\mathbf{T}$  is then chosen to transform  $\boldsymbol{\eta}$  into  $\mathbf{S} = (S_1, S_2, S_3)$  with  $\mathbf{S} = \mathbf{T}\boldsymbol{\eta}$ , and

$$\mathbf{T} = \begin{pmatrix} \frac{-\sin \Theta}{\sqrt{m_H}} & \frac{-\cos \Theta}{\sqrt{m_H}} & 0 & 0 & \frac{\sin \Theta}{\sqrt{m_O}} & \frac{\cos \Theta}{\sqrt{m_O}} \\ 0 & 0 & \frac{\sin \Theta}{\sqrt{m_H}} & \frac{-\cos \Theta}{\sqrt{m_H}} & \frac{-\sin \Theta}{\sqrt{m_O}} & \frac{\cos \Theta}{\sqrt{m_O}} \\ \frac{-\cos \Theta}{r_e \sqrt{m_H}} & \frac{\sin \Theta}{r_e \sqrt{m_H}} & \frac{\cos \Theta}{r_e \sqrt{m_H}} & \frac{\sin \Theta}{r_e \sqrt{m_H}} & \frac{\sin \Theta}{r_e \sqrt{m_O}} & \frac{-\sin \Theta}{r_e \sqrt{m_O}} \end{pmatrix}. \quad (\text{A.8})$$

## A.3 Definitions in Statistics

The mean value  $\bar{x}$  of a variable  $x_i$  with  $N$  independent values,  $i = 1, \dots, N$ , (also called best estimate for  $x_i$ ) is defined as

$$\bar{x} = \frac{1}{N} \sum_{i=1}^N x_i.$$

The **variance**  $\sigma^2$  of that variable  $x_i$  with mean  $\bar{x}$  is defined as

$$\sigma_x^2 := \frac{1}{N-1} \sum_i^N (x_i - \bar{x})^2 = \langle (x - \bar{x})^2 \rangle, \quad (\text{A.9})$$

where  $\langle \cdot \rangle$  is the expectation value. The **standard deviation** is defined as

$$\sigma_x = \sqrt{\frac{1}{N-1} \sum_{i=1}^N (x_i - \bar{x})^2}. \quad (\text{A.10})$$

According to the central limit theorem<sup>2</sup> (or theorem for large numbers) the **standard deviation of the mean** is then given by

$$\sigma_{\bar{x}} = \frac{\sigma_x}{\sqrt{N}}. \quad (\text{A.11})$$

It is worth mentioning that the standard deviation of the means goes as  $\frac{1}{\sqrt{N}}$  and is independent of the dimensionality of  $x_i$ . However, the standard deviation of the mean in eq.(A.11) relies on independent variables  $x_i$ .

In statistical mathematics, the **correlation** of two variables  $x$  and  $y$  taken from two sets of random variables  $\{X\}$  and  $\{Y\}$  is defined as,

$$\text{cor}(x, y) := \frac{\text{cov}(x, y)}{\sqrt{\text{cov}(x, \bar{x}) \text{cov}(y, \bar{y})}} \quad \text{with} \quad (\text{A.12})$$

$$\text{cov}(x, y) := \langle (x - y)^2 \rangle = \langle xy \rangle - \langle x \rangle \langle y \rangle \quad (\text{A.13})$$

The correlation vanishes,  $\text{cor}(x, y)=0$ , if  $\langle xy \rangle = \langle x \rangle \langle y \rangle$ .

The **auto-correlation time**,

$$\tau_{\text{corr}} := t_{\text{corr}} \cdot \delta\tau, \quad (\text{A.14})$$

with time step  $\delta\tau$  and  $t_{\text{corr}} \in [1, \dots, N]$ , identifies the number for subsequent variables within one set of  $N$  pseudo-random variables,  $\{X\} = \{x_1, \dots, x_N\}$  that are necessary to

---

<sup>2</sup>The central limit theorem states that the sum of  $N$  independent variables  $x_i$  with mean  $\bar{x}$  and variance  $\sigma^2$ , which are drawn from the same and arbitrary distribution  $\{X\}$ , approaches a normal (Gaussian) distribution with mean  $\mu$  and variance  $\sigma^2_x/N$  as the sample size  $N$  becomes large.

become uncorrelated. When normalizing the correlation function given in eq.(A.12), one obtains the **auto-correlation function**,

$$c(t) := \frac{\text{cor}(x_N, x_{N+t})}{\text{cor}(x_N, x_N)} = \frac{\frac{1}{N-t} \sum_{i=1}^{N-t} x_i x_{i+t} - (\frac{1}{N} \sum_{i=1}^N x_i)^2}{\frac{1}{N} \sum_{i=1}^N (x_i - (\frac{1}{N} \sum_{i=1}^N x_i))^2}, \quad (\text{A.15})$$

for large  $N$  and  $\langle x_N \rangle = \langle x_{N-t} \rangle$ . The auto-correlation function yields  $c(t=0) = 1$  and  $c(t=t_{\text{corr}}) = 0$ .

In order to incorporate the correlation of the  $N$  variables with a correlation time,  $t_{\text{corr}}$ , into the standard deviation of the mean in eq.(A.11),  $N$  must be divided by  $t_{\text{corr}}$  which can be written as,

$$\bar{\sigma}_{\text{corr}} = \frac{\sigma}{\sqrt{N}} \sqrt{t_{\text{corr}}}. \quad (\text{A.16})$$

## A.4 Construction of our HF Basis sets

The HF basis sets used in this work are radial, contracted **Gaussian type orbitals** (GTO) centered on the nuclei. Generally, a primitive GTO is given by,

$$\chi_{\zeta nlm}(r, \theta, \varphi) = N Y_{lm}(\theta, \varphi) r^{-l} e^{-\zeta_l r^2}, \quad (\text{A.17})$$

where  $r$ ,  $\theta$  and  $\varphi$  are polar coordinates,  $Y_{lm}$  the spherical harmonics and  $n$  the main,  $l$  the angular momentum and  $m$  the magnetic quantum number.  $\zeta_l$  gives the width of the radial part of the GTO and  $N$  is a normalization factor. The contraction of  $n$  primitive GTOs with the same angular momentum into a single contracted GTO,

$$\chi_{\zeta nlm}^{\text{C}} = \sum_{i=1}^n C_{li} \chi_{\zeta lmn}, \quad (\text{A.18})$$

gives a compact representation of the radial part of the HF orbitals, where the weights  $C_{li}$  are called contraction coefficients. For C, N, O and Si, we use the contraction noted as (10s10p1d)→[3s3p1d].<sup>3</sup> To be more specific, the first eight s- and p-primitive GTOs are contracted and describe the atomic orbital. The others are called polarization functions and are added to have more flexibility when describing molecular orbitals. For the H-atom, the basis contraction is noted as (9s1p)→[2s1p]. The coefficients  $\zeta_{li}$  and  $C_{li}$  for the CF basis and the N-atom are listed in Appendix B. These coefficients were previously obtained by fitting expression (A.18) to a numerical solution of the radial HF eq.(3.62) and was done by Claudia Filippi [private communication].

---

<sup>3</sup>Such notation means that 10 s and p primitive GTOs are contracted into 3 s and p GTOs.

## A.5 Technical Instructions for a MCSCF Calculation with QMC

To give an overview, we will list the subsequent steps which are required to perform a QMC calculation for multiple determinants. Thereby, we use the GAMESS package [SCHMIDT 1993].

1. The first step is to perform a HF calculation. The calculated coefficients of the MOs are written into an \*.dat file which is then copied into the MCSCF file called \*.mcscf.inp.
2. Using this input, a subsequent MCSCF calculation is performed by correctly assigning the active space with the highest occupied and lowest unoccupied MOs. Let us call the output \*.mcscf.log.
3. Based on this MCSCF output, the subsequent gamess2efp script (with “gamess2efp -E \*.mcscf.log > \*.mcscf.csf”) converts the ground state MCSCF wavefunction in \*.mcscf.log into so called Configuration State Functions<sup>4</sup> (CSF) and their constituting determinants. In particular, the coefficients for all CSF are given, where each of these CSFs is further broken down into its constituting determinants which have again a coefficient within the CSF. All results are written in the file \*.mcscf.csf.
4. Edit the script “twf.inp” with “load \*.mcscf.csf”.
5. The script “efpci\_csf.x” (with “efpci\_csf.x < twf.inp” > \*.twf.log) finally decomposes all CSF into single determinants (where the script considers that one determinant may belongs to several CSF simultaneously). Thereby, the determinants are ordered according to decreasing importance as listed e.g. in Figure(5.8). That script also writes out the file qmcwf.inp (which can be used as input file only for the new version<sup>5</sup> of the VMC and DMC programs).
6. With the last script “gamess2qmc” (with “gamess2qmc -n x -t initial \*.mcscf.log”), the required numerical orbital are generated for x orbitals (\*.mcscf.lcao) which need to be renamed to orbitals.1.
7. Having done steps 1 to 6, a subsequent VMC / QMC calculation can be performed as described in Section 3.2 and 3.3. One important aspect need to be mentioned for the optimization procedure of  $\Psi_T$ . We ensure the spatial symmetry of  $\Psi_T$  by equating the determinantal coefficients that belong to the same configuration state function, see also Ref. [ROOS 1992].

---

<sup>4</sup>CSF are linear combinations of certain determinants which allows to create functions that are eigenvectors of the spin. Detailed discussions about CSF can be found in Ref.[JENSEN 2002] or [ROOS 1992].

<sup>5</sup>The version after January 2003.

## A.6 Unit Conversion

Quantity			SI
Hartree	1Ha	= 27.21140	eV
Elementary Charge	1e	= $1.602189 \cdot 10^{-19}$	C
Bohr Radius	$a_0$	= $0.529177 \cdot 10^{-10}$	m
Planck constant	$\hbar$	= $6.582122 \cdot 10^{-16}$	eV s
atomic mass	1u	= $1.66057 \cdot 10^{-27}$	kg
Boltzmann			
Other Conversion Factors			
	1kcal/mol	= 1/627.5	Ha
	1kcal/mol	= 1/23.060	eV
	1kJ/mol	= 1/96.548	eV
	1cal	= 4.18680	J

# Appendix B

## Tables

Basis	$E_{\text{molecule}}^{\text{psp}}$ [in Ha]	$E_{\text{atom}}^{\text{psp}}$ [in Ha]	$E_{\text{B}}^{\text{psp}}$ [in eV]	$r$ [in Å]	$E_{\text{molecule}}^{\text{full}}$ [in Ha]	$E_{\text{atom}}^{\text{full}}$ [in Ha]	$E_{\text{B}}^{\text{full}}$ [in eV]	$r$ [in Å]
CF	-19.8013	-9.7404	8.723	1.100				
aug-cc-pVDZ	-19.7115	-9.6945	8.778	1.100	-109.2942	-54.4870	8.713	1.100
aug-cc-pVTZ	-19.8124	-9.7310	9.533	1.100	-109.3808	-54.5169	9.441	1.100
aug-cc-pVQZ	-19.8363	-9.7366	9.880	1.100	-109.4072	-54.5255	9.693	1.100
aug-cc-pV5Z	-19.8759	-9.7569	9.852	1.100	-109.4155	-54.5282	9.770	1.100
CF	-19.8019	-9.7404	8.741	1.116				
aug-cc-pVDZ	-19.7133	-9.6945	8.825	1.125	-109.2953	-54.4870	8.744	1.121
aug-cc-pVTZ	-19.8124	-9.7310	9.534	1.104	-109.3808	-54.5169	9.442	1.104
aug-cc-pVQZ	-19.8363	-9.7366	9.880	1.099	-109.4072	-54.5255	9.693	1.101
aug-cc-pV5Z					-109.4155	-54.5282	9.770	1.099

Table B.1: This table presents the  $\text{N}_2$  total and binding energies calculated with CCSD(T) for the CF pseudopotential and for all electrons. In the upper half of the table all energies are calculated at a fixed equilibrium distance. In the lower part of this table, all energies are calculated at the optimized geometry for that basis set. All calculations were done by Thorsten Klüner at the FHI, Berlin (2003).

Basis	GTOs	$E_{\text{tot}}(\text{N}_2)$	$E_{\text{tot}}(\text{N})$
		[in Ha]	[in Ha]
6-31++G	4s3p	-19.2995	-9.5960
6-311++G(3df,3pd)	5s3p1d	-19.4136	-9.6145
cc-pCVDZ	4s3p1d	-19.4195	-9.6198
6-31G (3df,3pd)	3s2p3d1f	-19.4226	-9.6135
aug-cc-pVTZ	5s4p3d2f	-19.4483	-9.6256
cc-pV5Z (without f,g)	6s5p4d	-19.4528	-9.6319
d-aug-cc-pV6Z	9s8p7d	-19.4589	-9.6355
aug-ccpVQZ	6s5p4d3f	-19.4638	-9.6361
aug-pV7Z (without f,g)	9s8p7d	-19.4650	-9.6387
CF+ (Claudia Filippi)	5s5p1d	-19.4771	-9.6487
aug-ccpV5Z	7s6p5d4f	-19.4787	-9.6435
cc-pwCVTZ	6s5p3d1f	-19.4812	-9.6472
cc-pCVTZ	6s5p4d1f	-19.4819	-9.6455
cc-pCVQZ (without f)	8s7p5d	-19.4846	-9.6482
cc-pwCV5Z (without f,g)	10s9p7d	-19.4857	-9.6486
cc-pCV5Z (without f,g)	10s9p7d	-19.4858	-9.6488
cc-pCVQZ	8s7p5d3f	-19.4881	-9.6483
cc-pCV5Z	10s9p7d5f	-19.4892	-9.6488

Table B.2: This table present HF total energies for a selection of different basis sets for N and  $\text{N}_2$ . All basis sets are taken from Ref. [NIST 2003]. For all calculations, the CF pseudopotential is used. All basis set abbreviations can be found in Ref.[JENSEN 2002].



Basis set				Pseudopotential				
$l$	PGTO	$\zeta$	Coef.	$l'$	$k$	$A_{l'k}$	$n_{l'k}$	$B_{l'k}$
s	1	21.233646	-0.000673	0	1	5.00000	1	24.28433
	2	0.049437	0.004632	0	2	121.42166	3	11.78922
	3	0.117541	0.103962	0	3	-1.00044	2	124.58565
	4	0.279466	0.472762	0	4	-143.94439	2	13.30095
	5	0.664458	0.461672	0	5	213.14309	2	19.31139
	6	1.579818	0.130162	0	6	-146.66953	2	28.03784
	7	3.756178	-0.194645	0	7	72.02484	2	40.70759
	8	8.930698	0.017413	0	8	-27.13661	2	59.10255
s	1	0.3	1	0	9	6.92602	2	85.80985
s	1	0.1	1	1	1	-5.29300	2	50.00000
p	1	21.233646	-0.000308	1	2	9.76307	2	4.00000
	2	0.049437	0.063051	1	3	-143.68226	2	5.29589
	3	0.117541	0.212836	1	4	615.65354	2	7.01161
	4	0.279466	0.334176	1	5	-1213.22120	2	9.28318
	5	0.664458	0.322225	1	6	1573.26177	2	12.29067
	6	1.579818	0.217975	1	7	-1344.36312	2	16.27251
	7	3.756178	0.092588	1	8	746.97583	2	21.54435
	8	8.930698	0.039922	1	9	-264.70274	2	28.52412
p	1	0.3	1	1	10	55.38172	2	37.76514
p	1	0.1	1					
d	1	0.8	1					

Table B.3: This table present the used CF basis and CF pseudopotential for the N-atom. For the basis, all parameters are defined in Appendix A.4. For the Pseudopotential, all parameters are defined in Section 3.4.1.



# Bibliography

- [Anderson 1975] J. Anderson, *A random-walk simulation of the S-eq. for  $\text{H}_3^+$*  J. Chem. Phys. **63**, No. 4 (1975)
- [BACHELET 1989] G. Bachelet, D. Ceperley, K. Runge *Novel Pseudo-Hamiltonian for QMC Simulations* Phys. Rev. Lett. **62** 2088 (1989)
- [BANEWELL 1994] C. Banwell *Fundamentals of Molecular Spectroscopy* McGraw-Hill (1994)
- [BARONE 1996] V. Barone, C. Adamo *Proton transfer in the ground and lowest excited states of malonaldehyde* J. Chem. Phys, **105** 24 (1996)
- [CEPERLEY 1980] D. Ceperley, B. Alder *Ground State of the Electron Gas by a Stochastic Method* Phys. Rev. Lett., **45** No. 7 566 (1980)
- [CEPERLEY 1996] D. Ceperley *Lecture notes on QMC* 1996 ([www.physics.uiuc.edu/research/ElectronicStructure/498-s97/lnotes/lect22.html](http://www.physics.uiuc.edu/research/ElectronicStructure/498-s97/lnotes/lect22.html))
- [CRC] *CRC Handbook of Chemistry and Physics* 67th ed. CRC Press (1986)
- [DUBI 1999] A. Dubi, *Monte Carlo Applications in Systems Engineering* Wiley & Sons (1999)
- [ENGELKE 1984] F. Engelke *Aufbau der Moleküle* Teubner Studienbücher (1984)
- [ERNZERHOF 1999] M. Ernzerhof, G. Scuseria *Assessment of the PBE exchange-correlation functional* J. Chem. Phys. **110** No.11 (1999)
- [FELLER 1998] D. Feller, K. Peterson, J. Chem. Phys. **108** No.1 154 (1998)
- [FAHY 1990] S. Fahy *VMC nonlocal pseudopotential approach to solids* Phys. Ref. B **42** No. 6 3503 (1990)

- [FILIPPI 1996] C. Filippi, C. Umrigar, J. Chem. Phys. **105** 213 (1996)
- [FILIPPI 2002 ] C. Filippi, S. Healy, P. Kratzer, E. Pehlke, M. Scheffler *QMC Calculations of  $H_2$  Dissociation on Si(001)* Phys. Rev. Lett. **89** No. 16, 166102-2 (2002)
- [FILIPPI 2000] C. Filippi, C. J. Umrigar *Correlated sampling in QMC* Phys. Rev. B **61** No. 24 16291 (2000)
- [FOULKES 2001] W. Foulkes, L. Mitas, R. Needs, G. Rajagopal *QMC simulations of solids* Rev. of Mod. Phys. **73** No.1 33 (2001)
- [GAUSSIAN 2003] Env. Mol. Science Laboratory *Gaussian Basis Set* Washington, USA ([www.emsl.pnl.gov/forms/basisform.html](http://www.emsl.pnl.gov/forms/basisform.html))
- [GRABO 1999] T. Grabo, T. Kreibich, S. Kurth, E. Gross *Orbital functionals in DFT: the optimized effective potential method*, from the following book: Strong Coulomg Correlations in Electronic Structure: Beyond the LDA, edited by V. Ansimov, p203-311 Gordon & Breach (1999)
- [GREEFF 1998] C. Greeff, W. Lester *A soft HF pseudopotential for carbon with applications to QMC* J. Chem. Phys. **109** No.5 1697 (1998)
- [GROSSMAN 2002] J. Grossman *Benchmark QMC calculations* J. Chem. Phys. **117** No. 4 1434 (2002)
- [HADZI 1997] D. Hadzi (editor) *Theoretical Treatments of H-Bonding* J. Wiley & Sons Ltd., 1997
- [HAKEN 2000] H. Haken, H. Wolf *Atom und Quantenphysik* Springer (2000)
- [HOLLEMANN 1995] A. F. Holleman, E. Wiberg *Lehrbuch der Anorganischen Chemie* Walter de Gruyter (1995)
- [LESTER 1994] B. Hammond, J. Lester, P. Reynolds *Monte Carlo Methods in Ab Initio Quantum Chemistry* World Scientific, Singapore (1994)
- [HERZBERG 1979] G. Herzberg *Spectra of Diatomic Molecules* Vol. I -IV (1979)
- [ISMER 2002] L. Ismer *Diplomarbeit* TU Berlin (2002)
- [JEFFREY 1994] G. Jeffrey, W. Saenger *Hydrogen Bonding in Biological Structures* Springer Verlag Berlin (1994)

- [JENSEN 2002] F. Jensen *Introduction to Computational Chemistry* WILEY (2002)
- [POPLE 1992] B. Johnson, P. Gill, J. Pople, J. Chem. Phys. **98** 5612 (1992)
- [KALOS 1974] M. Kalos, D. Levesque and L. Verlet *H at  $0^\circ$  with hard-sphere and other forces* Phys. Rev. A **9** 2178 (1974)
- [KOCH 2001] W. Koch, M. Holthausen *A Chemist's Guide to DFT* Wiley-Vch (2001)
- [KUTZELNIGG 1992] W. Kutzelnigg *Einführung in die Theoretische Chemie* Bd. I/II, Weinheim Verlag (1992)
- [LANDAU 1963] L. Landau, E. Lifschitz *Lehrbuch der Theoretischen Physik - Mechanik* Akademie-Verlag Berlin (1963)
- [LEE 1988] C. Lee, W. Yang, R. Parr *Dev. of the Colle-Salvetti correlation-energy formula into a functional of electron density* Phys. Rev. B **37** 785 (1988)
- [LESTER 2001] W. Lester et al. *Soft PsP's for efficient QMC calculations from Be to Ne and Al to Ar* J. Chem. Phys. **114** 7790 (2001)
- [MANTE 2001] S. Mante, A. Lüchow *On the accuracy of the fixed-node DMC method* J. Chem. Phys. **115** No.12 5362 (2001)
- [MANTEN 2001] S. Mante, A. Lüchow *On the accuracy of the FN DMC* J. Chem Phys. **115** 5362 (2001)
- [METROPOLIS 1953] N. Metropolis, A. and M. Rosenbluth, A. and E. Teller *Equations of state calculations by fast computing machines* J. Chem. Phys. **21** 1087 (1953)
- [MITAS 1991] L. Mitas, E. Shirley and D. Ceperley *Nonlocal Pseudopotentials and DMC* J. Chem. Phys. **95** 3467 (1991)
- [MITAS 1997] L. Mitas, J. Grossman *QMC studies of Si and C Molecular Systems* in Recent Advances in QMC World Scientific (1997)
- [MITAS 1994] L. Mitas, R. Martin *QMC of Nitrogen* Phys. Rev. Lett. **72** 2438 (1994)
- [Moller 1934 ] C. Møller and M. Plesset, Phys. Rev. **46** 618 (1934)

- [NIST 2003] National Institute of Standards and Technology, USA, (<http://www.nist.gov/>)
- [NEWMAN 1999] M. E. J. Newman and G. T. Barkema. *Monte Carlo Methods in Statistical Physics* Oxford University Press (1999)
- [NOLTING 1996] W. Nolting *Elektrodynamik* Bd.3, Vieweg (1996)
- [NOVOA 1995] J. Novoa, C. Sosa *Evaluation of the DFT Approximation on the Computation of Hydrogen Bond Interactions* J. Phys. Chem. **99** 15837 (1995)
- [PERDEW 1981] J. Perdew, A. Zunger *Self-interaction correction to DF approximations for many-electron systems* Phys. Rev. B **23** No. 10 5048 (1981)
- [POPLE 1988] J. Pople, M. Head-Gordon, M. Frisch *MP2 evaluation by direct methods* Chem. Phys. Lett. **153** 503 (1988)
- [POPLE 1987] J. Pople, M. Head-Gordon, K. Raghavachari *Quadratic Configuration Interaction-A General Technique for determining the electron correlation energies* J. Chem. Phys. **87** 5968 (1987)
- [PRESS 2002] W. Press, S. Teukolsky *Numerical Recipes* Cambridge University Press (2002)
- [REIF 1975] F. Reif *Physikalische Statistik* de Gruyter (1975)
- [ROOS 1992] B. Roos *Lecture Notes in Quantum Chemistry* Springer-Verlag Berlin (1992)
- [SCHAUTZ 1998] F. Schautz, H. Flad, M. Dolg *QMC study of BE<sub>2</sub> and group 12 dimers* Theoret. Chem. Acc. **99** 231 (1998)
- [SCHEFFLER 2001] M. Scheffler *Vorlesungsskript Festkörperphysik* Kapitel 1 (2001)
- [SCHEINER 1997] S. Scheiner *Hydrogen Bonding, a Theoretical Perspective* Oxford University Press (1997)
- [SCHERZ 1999] U.Scherz *Quantenmechanik* Teubner Studienbücher (1999)
- [LU 2003] Shih-I Lu, *A DMC Monte Carlo study of geometries and harmonic frequencies* J. Chem. Phys. **120** 14 (2003)
- [SCHMIDT 1993] M.W.Schmidt et all., J. Comp. Chem. **14**, 1347 (1993)

- [SUBRAMANIAM 1992] R. Subramaniam, M. Lee, K. Schmidt, J. Moskowitz *Quantum simulation of the electronic structure of diatomic molecules* J. Chem. Phys. **97** 2600 (1992)
- [PERDEW 2003] V. Staroverov, G. Scuseria, J. Tao, J. Perdew, Comparative assessment of a new nonempirical density functional: molecules and H-bonded complexes, J. Chem. Phys. **119** 12129 (2003)
- [STEVENS 1984] W. Stevens, H. Basch, M. Krauss *SBK PsP for first- and second row atoms* J. Chem. Phys. **81** 6026 (1984)
- [STRUVE 1989] W. Struve *Fundamentals of Molecular Spectroscopy* Wiley-International Publication (1989)
- [TSUZUKI 2001] S. Tsuzuki, H. Lüthi *Interaction energies of van der Waals and H-bonded systems calculated with DFT* J. Chem. Phys. **114** No. 9 3949 (2001)
- [TUMA et al. 1999] C. Tuma, D. Boses, N. Handy *Predicting the Binding Energy of H-Bonded Complexes: A comparative DFT study* Phys. Chem. Chem. Phys. **1** 3939 (1999)
- [UMRIGAR et al. 1988] C. Umrigar, K. Wilson and J. Wilkins *Optimized Wave Function for QMC* Phys. Rev. Lett. **60** No. 17 (1720)
- [UMRIGAR et al. 1993] C. Umrigar, M. Nightingale, K. Runge *A DMC algorithm with very small time-step errors* J. Chem. Phys. **99** 1865 (1993)
- [UMRIGAR et al. 1993] C. J. Umrigar, M. P. Nightingale and K. J. Runge, J. Chem Phys. **99** 2865 (1993)
- [WAHN 2002] M. Wahn *Diplomarbeit* TU Berlin (2002)